

NASA CR-

FINAL TECHNICAL REPORT

INVESTIGATION OF THE FRACTURE MECHANICS  
OF BORIDE COMPOSITES

by

Edward V. Clougherty, Richard L. Pober and Larry Kaufman

MANLABS, INC

21 Erie Street

Cambridge, Massachusetts 02139

prepared for

NATIONAL AERONAUTICS AND SPACE ADMINISTRATION

September 1972

Contract NASW-2088

NASA Headquarters  
Washington, D. C. 20546  
James Gangler, Project Manager

## ABSTRACT

New and significant results were obtained in fabrication studies of the role of metallic additives of Zr, Ti, Ni, Fe and Cr on the densification of  $\text{ZrB}_2$ . All elemental additions lower the processing temperatures required to effect full densification of  $\text{ZrB}_2$ . Each addition effects enhanced densification by a clearly distinguishable and different mechanism and the resulting fabricated materials are different. A significant improvement in strength and fracture toughness was obtained for the  $\text{ZrB}_2/\text{Ti}$  composition. Mechanical characterization studies for the  $\text{ZrB}_2/\text{SiC}/\text{C}$  composites and the new  $\text{ZrB}_2/\text{Metal}$  materials produced data relevant to the effect of impacting load on measured impact energies, a specimen configuration for which controlled fracture could occur in a suitably hard testing apparatus, and fracture strength data. Controlled fracture--indicative of measurable fracture toughness--was obtained for the  $\text{ZrB}_2\text{-SiC-C}$  composite designated VIII(14,30)M2 and a  $\text{ZrB}_2/\text{Ti}$  composite fabricated from  $\text{ZrB}_2$  with an addition of 30 weight per cent Ti. The work of controlled fracture, W/2A, for VIII(14,30)M2 is  $88 \text{ J/M}^2$  ( $0.50 \text{ in-lbs/in}^2$ ); for the  $\text{ZrB}_2$  with 30 per cent Ti,  $138 \text{ J/M}^2$  ( $0.79 \text{ in-lbs/in}^2$ ). The fracture strength of the  $\text{ZrB}_2/\text{Ti}$  composite at room temperature is  $10.2 \times 10^8 \text{ N/M}^2$  (150,000 psi). The increased strength and toughness of the  $\text{ZrB}_2/\text{Ti}$  composite is consistent with the presence of a significantly large amount of a fine grained acicular phase formed by reaction of Ti with  $\text{ZrB}_2$  during processing.

## FOREWORD

The research described in this report was conducted by ManLabs, Inc. under NASA Contract NASW-2088. The work was done under the cognizance of the NASA Project Manager, Mr. James Gangler, NASA Headquarters, Washington, D. C. 20546, with Drs. Larry Kaufman and Edward V. Clougherty of ManLabs, Inc. serving as Principal Investigators. ManLabs personnel who participated in this study included Dr. R. L. Pober, H. Nesor, L. Gordon, K. Meaney, J. Davis and H. Tushman.

## TABLE OF CONTENTS

I.	INTRODUCTION AND BACKGROUND . . . . .	1
A.	Background . . . . .	1
B.	Introduction . . . . .	1
II.	FABRICATION AND CHARACTERIZATION . . . . .	6
A.	Introduction . . . . .	6
B.	Processing Procedures . . . . .	6
C.	Material Identification . . . . .	7
D.	Processing Experiments . . . . .	8
1.	ZrB <sub>2</sub> /Ti System . . . . .	8
2.	ZrB <sub>2</sub> /Zr System . . . . .	11
3.	ZrB <sub>2</sub> /Ni System . . . . .	11
4.	ZrB <sub>2</sub> /Ni: Reinforcement Systems . . . . .	12
5.	ZrB <sub>2</sub> /Fe System . . . . .	13
6.	ZrB <sub>2</sub> /Cr System . . . . .	14
7.	Diboride Materials V, VIII(14,30)M2 and VIII(18,10) . . . . .	14
8.	WC6Co . . . . .	14
III.	MECHANICAL CHARACTERIZATION: STRENGTH AND WORK OF FRACTURE . . . . .	15
A.	Introduction . . . . .	15
B.	Experimental Test Procedures . . . . .	16
1.	Impact Apparatus . . . . .	16
2.	Slow Bend Apparatus for Work of Fracture . . . . .	16
3.	Fracture Strength Apparatus . . . . .	17
C.	Test Results . . . . .	18
1.	Impact Test Results . . . . .	18
2.	Slow Bend Test Results . . . . .	21
3.	Fracture Strength Test Results . . . . .	24
IV.	DISCUSSION OF RESULTS . . . . .	26
	REFERENCES . . . . .	31
	TABLES . . . . .	33
	FIGURES . . . . .	61



## LIST OF TABLES

1.	Processing Conditions for $\text{ZrB}_2/\text{Ti}$ Compositions . . . . .	33
2.	Processing Conditions for $\text{ZrB}_2/\text{Zr}$ Compositions . . . . .	34
3.	Processing Conditions for $\text{ZrB}_2/\text{Ni}$ Compositions . . . . .	34
4.	Processing Conditions for $\text{ZrB}_2/\text{Metal Matrix-Wire}$ Mesh Composites . . . . .	35
5.	Processing Conditions for $\text{ZrB}_2/\text{Fe}$ Compositions . . . . .	36
6.	Impact Test Data for Undersized Specimens . . . . .	37
7.	Impact Test Data for $\text{ZrB}_2\text{-Metal}$ Composites . . . . .	39
8.	Impact Test Data for $\text{ZrB}_2\text{-Metal}$ Composites . . . . .	41
9.	Impact Test Data for $\text{ZrB}_2$ Composition: VIII(18,10) . . . . .	43
10.	Impact Test Data for $\text{ZrB}_2$ Metal Composites . . . . .	44
11.	Impact Test Results for Variation of Incident Impacting Energy . . . . .	46
12.	"Soft" Slow Bend Test Data for $\text{ZrB}_2/\text{Fe}$ and $\text{ZrB}_2/\text{Cr}$ Composites . . . . .	48
13.	"Soft" Slow Bend Test Data for Diboride VIII(18,10) and $\text{ZrB}_2$ Metal Composites . . . . .	50
14.	"Hard" Slow Bend Test Data for V-Notch Specimens . . . . .	52
15.	Comparison of Results for "Soft" and "Hard" Slow Bend Tests . . . . .	54
16.	"Hard" Slow Bend Test Data and Results for Chevron Notched Specimens . . . . .	56
17.	Fracture Strength Levels for $\text{ZrB}_2$ Metal Composites . . . . .	58
18.	Work of Controlled Fracture, W/2A, for Ceramic Materials . . . . .	60

## LIST OF FIGURES

1.	Microstructural Features and Characterization Data for Hot Pressed Material, $\text{ZrB}_2\text{12.5Ti}$ , HP 118 . . . . .	61
2.	Microstructural Features and Characterization Data for Hot Pressed Material, $\text{ZrB}_2\text{20Ti}$ , HP 124 . . . . .	62
3.	Microstructural Features and Characterization Data for Hot Pressed Material, $\text{ZrB}_2\text{20Ti}$ , HP 141 . . . . .	63
4.	Microstructural Features and Characterization Data for Hot Pressed Material, $\text{ZrB}_2\text{25Ti}$ , HP 127 A . . . . .	64
5.	Microstructural Features and Characterization Data for Hot Pressed Material, $\text{ZrB}_2\text{30Ti}$ , HP 172 B . . . . .	65
6.	Isothermal Section of the Ti-Zr-B System Slightly Above $2640^\circ\text{F}$ . . . . .	66
7.	Isothermal Section of the Ti-Zr-B System at $2875^\circ\text{F}$ . . . . .	67
8.	Area of Billet HP 124 Studied by Electron Microprobe Scanning Display . . . . .	68
9.	Billet HP 124, Sample Current (-) Display with Titanium-rich Areas Appearing Light . . . . .	68
10.	Billet HP 124, Zr- $\text{L}\beta$ (1) X-ray Display . . . . .	69
11.	Billet HP 124, Ti- $\text{K}\alpha$ (1) X-ray Display . . . . .	69
12.	Area of Billet HP 141 Studied by Electron Microprobe Scanning Display . . . . .	70
13.	Magnified Area of Billet HP 141 Studied by Electron Microprobe Scanning Display . . . . .	70
14.	Billet HP 141, Sample Current (-) Display, Ti-rich Areas Light . . . . .	71
15.	Billet HP 141, Zr- $\text{L}\beta$ (1) X-ray Display . . . . .	71
16.	Billet HP 141, Ti- $\text{K}\alpha$ (1) X-ray Display . . . . .	71
17.	Area of Billet HP 150 B Studied by Electron Microprobe Scanning Display . . . . .	72
18.	Billet HP 150 B, Sample Current (-) Display with Titanium-rich Areas Appearing Light . . . . .	72
19.	Billet HP 150 B, Zr- $\text{L}\beta$ (1) X-ray Display . . . . .	73
20.	Billet HP 150 B, Ti- $\text{K}\alpha$ (1) X-ray Display . . . . .	73
21.	Microstructural Features and Characterization Data for Hot Pressed Material, $\text{ZrB}_2\text{20Zr}$ , HP 126 . . . . .	74

# LIST OF FIGURES (Continued)

22.	Microstructural Features and Characterization Data for Hot Pressed Material, $\text{ZrB}_2\text{20Zr}$ , HP 144 . . . . .	75
23.	Microstructural Features and Characterization Data for Hot Pressed Material, $\text{ZrB}_2\text{20Zr}$ , HP 174 A . . . . .	76
24.	Microstructural Features and Characterization Data for Hot Pressed Material, $\text{ZrB}_2\text{50Zr}$ , HP 152 A . . . . .	77
25.	Microstructural Features and Characterization Data for Hot Pressed Material, $\text{ZrB}_2\text{20Ni}$ , HP 153 . . . . .	78
26.	Microstructural Features and Characterization Data for Hot Pressed Material, $\text{ZrB}_2\text{20Ni}$ , HP 173 A . . . . .	79
27.	Microstructural Features and Characterization Data for Hot Pressed Material, $\text{ZrB}_2\text{20Ni}$ : Nichrome Wire, HP 127 . . . . .	80
28.	Microstructural Features and Characterization Data for Hot Pressed Material, $\text{ZrB}_2\text{20Ni}$ : Nichrome Wire, HP 131 . . . . .	81
29.	Microstructural Features and Characterization Data for Hot Pressed Material, $\text{ZrB}_2\text{20Ni}$ : Nichrome Wire, HP 134 . . . . .	82
30.	Microstructural Features and Characterization Data for Hot Pressed Material, $\text{ZrB}_2\text{20Ni}$ : Stainless Steel Wire, HP 138 . . . . .	83
31.	Microstructural Features and Characterization Data for Hot Pressed Material, $\text{ZrB}_2\text{10Fe}$ , HP 98 . . . . .	84
32.	Microstructural Features and Characterization Data for Hot Pressed Material, $\text{ZrB}_2\text{10Fe}$ , HP 101 . . . . .	85
33.	Microstructural Features and Characterization Data for Hot Pressed Material, $\text{ZrB}_2\text{20Fe}$ , HP 106 . . . . .	86
34.	Microstructural Features and Characterization Data for Hot Pressed Material, $\text{ZrB}_2\text{30Fe}$ , HP 107 . . . . .	87
35.	Composition, Fabrication Conditions and Microstructural Features of Diboride Material VIII(18,10) . . . . .	88
36.	Composition, Modulus Data, and Microstructural Features of VIII(14,30)M2, HP6M2 . . . . .	89
37.	Microstructural Characteristics of Boride V (80V/o $\text{ZrB}_2$ -20V/oSiC) . . . . .	90
38.	Microstructural Features of Tungsten Carbide Cermet, WC6Co . . . . .	91
39.	Notch and Kerf Configurations for Impact and Slow Bend Test Specimens . . . . .	92

## LIST OF FIGURES (Continued)

- 40. Typical Slow Bend Load vs. Deflection Data for Catastrophic Failure of V-Notch Specimens on Hard Test Machine . . . . . 93
- 41. Chevron Configurations for Slow Bend Test Specimen . . . 94
- 42. Typical Slow Bend Load vs. Deflection Data for Controlled, Semi-Controlled and Catastrophic Failure of Deep Chevron Specimens . . . . . 95

## I. INTRODUCTION AND BACKGROUND

### A. Background

The study of the fracture characteristics of diboride compositions was primarily initiated on the basis of significant progress in the development of oxidation resistant materials (1) and the results of simulated tests for reentry applications (2). The material development program identified several compositions containing  $ZrB_2$  or  $HfB_2$  as the principal phase with added SiC and/or C which could be hot pressed to dense, fine grained polycrystalline materials. Results of physical, mechanical, thermal, and oxidation tests showed combinations of properties which strongly suggested that superior material performance could be realized in several application areas for components such as rocket nozzles, air augmented engine inlet components, and leading edges and other thermal protection hardware for lifting reentry and space shuttle applications. Superior performance was achieved in a series of simulated tests in which subscale components were exposed to hot oxidizing and/or corrosive gases and severe thermal stresses were developed (3); the reentry application was studied in considerable detail (2). The results of the latter program demonstrated unique advantages of boride compositions for long exposure, multi-mission capabilities under lifting reentry conditions (4). Follow on programs have demonstrated the successfulness of the material development study (1) and simulated testing program (2).

The following studies have been initiated to further advance diboride technology.

(1) Fabrication Process for Oxidation Resistant Diboride Materials, AF 33(615)-70-C-1250, a manufacturing technology program;

(2) Research Program on Transition Metal Diboride Matrix Composites, F 33615-69-C-1645, an attempted material improvement program;

(3) Test and Evaluation of Refractory Throat Chamber Materials with  $N_2O_4$ /Amine Propellants, F04611-71-C-0007; a material and design test program using diboride compositions as nozzle throat materials;

(4) Ceramic Nose Cap and Leading Edges for High Performance Weapon Systems, F 33615-70-C-1179, a design, analysis subscale and full scale test program using a diboride composition as the ceramic material.

### B. Introduction

Although considerable data and results have been accumulated to reinforce the earlier projected utility of diboride materials (1, 2, 4), the inherent brittleness of such materials re-

tards acceptance by the design engineer. The study of the fracture characteristics of boride compositions was initiated to attempt to alleviate this problem and to further advance the diboride technology. The program has from the outset been divided into two parts: studies of fracture energies based upon results of impact and slow bend tests of notched specimens and studies of material development designed to produce diboride composites with improved fracture characteristics relative to the diboride materials earlier developed by the Air Force (1, 2).

An inherent difficulty in the program arose from the strength characteristics of boride materials containing SiC and/or C, hereafter referred to as "boride composites" although not containing fiber, whisker, nor filament reinforcement agents. Fracture studies of brittle ceramics and glasses generally are concerned with attempts to measure fracture surface energies by devising a specimen configuration which will permit a fracture to initiate and then proceed in a controlled manner (5). For the most part, these studies are carried out with brittle materials of lower strength levels than have been measured for the boride composites (1); impact data for ceramics and glasses are not generally measured, or, at least, are not reported. Accordingly, measurement of mechanical properties of significance in the solution of the fracture problem of boride composites presented a difficult task. Furthermore, improvement of mechanical performance of the boride composites developed under this study is itself a challenge as fracture resistant and/or improved impact resistant ceramics have long been sought to realize the potential of many high temperature refractory compounds such as borides and carbides. Implicit in the development of such materials for boride compositions is the availability of a suitable test method to distinguish one material from another.

In the first year of the program (6), effort was expended in both the fabrication and mechanical test areas. Impact tests and slow bend tests were conducted for nine (9) diboride composite materials and for high strength WC6Co which was employed as a control material. The immediate object of the material development program was to produce a diboride composite with impact and slow bend fracture energies comparable to the levels displayed by WC6Co. Impact tests performed with a subsized Charpy configuration 1 cm. square by 5 cm. long (0.394 in. square by 2.165 in. long), with a 45° V-notch 0.20 cm. (0.080 in.) deep, showed a value of 1.03 Joules (0.76 ft.-lbs.) for WC6Co and a value close to 0.27 J (0.20 ft-lbs) for several boride composites. Reproducibility of the impact energies was quite acceptable although the measured energies are a small part of the total impact energy, 32.4 J (24 ft-lbs). The impact energy is primarily an engineering property; it is, however, related to the fracture surface energy.

The quantity work of fracture,  $W/A$ , is obtained from slow bend tests of specimens of various geometries (5). In metallic materials, pre-cracked, notched specimens of the subsized Charpy dimensions cited above are tested in impact and in slow bending and the work of fracture is of the same magnitude as the impact energy, normalized for the surface area under the pre-crack (7a, 7b). For metallic materials it is the practice to calculate the area as that of one of the surfaces produced in the fracture. In the first year of this study, slow bend tests were also conducted with the same specimen configuration used for the Charpy impact tests. Controlled fractures were not obtained for WC6Co, nor for the majority of the boride composites. Stored elastic energy in strong, brittle materials is generally more than sufficient to cause catastrophic propagation of the crack after initiation. Values of  $W/A$  were  $455 \text{ J/M}^2$  ( $2.6 \text{ inch lbs./inch}^2$ ) for WC6Co and 70 to  $277 \text{ J/M}^2$  ( $0.40 \text{ to } 1.30 \text{ in.lbs./in}^2$ ) for the boride composites with the larger values greater than  $175 \text{ J/M}^2$  ( $1.0 \text{ in.lbs./in}^2$ ) measured for composites containing the highest amounts of graphite, that is, the boride designated VIII (14, 30) and VIII (14, 30) M2. There was some experimental evidence to suggest that the latter two materials did show a controlled fracture. In earlier mechanical tests of bending strength (1), evidence for crack arrestment by graphite was found. Subsequently, crack arrestment was observed in subscale components tested under mechanical loadings anticipated for lifting reentry conditions (8).

In the earlier development of polycrystalline diboride materials (1), the ceramic additives SiC and/or C were successfully employed to enhance the fabricability of dense, fine grained, crack-free materials. The role of these additives, singularly and combined, is quite complex and appears to be mutually beneficial. Among other effects, the SiC improves oxidation resistance and the C lowers the elastic modulus and thereby improves thermal shock resistance. The formed materials have less thermal stability in controlled atmospheres than the diborides without intentional additives, but the maximum use temperature in oxidizing and/or corrosive environments is higher for the boride composites (9). These boride composites being polycrystalline ceramic materials do not contain except for the graphite phase reinforcing agents nor intergranular strengthening agents designed to improve fracture characteristics. A recent program studied several approaches to this problem (10). Physical deterioration of fibers and other reinforcements constituted of SiC, C and  $\text{ZrO}_2$  caused by high processing temperatures precluded the attainment of improved fracture characteristics. Mechanical property data generated did not include impact energies nor work of fracture,  $W/A$ , from slow bend tests; transverse bend strength, elastic modulus, and shear modulus tests were performed. The strongest material produced was a  $\text{ZrO}_2$  (Zircar)/ $\text{ZrB}_2$ +SiC

composite with a transverse bend strength of  $5.5 \times 10^8$  N/M<sup>2</sup> (81,000 psi). In the earlier boride development program (1), a ZrB<sub>2</sub> composite with 18 volume per cent SiC and 10 volume per cent graphite, VIII(18,10), was prepared with a bend strength of  $6.4 \times 10^8$  N/M<sup>2</sup> (94,000 psi).

In the present program, the processing studies have centered on the use of metal additives to lower fabrication temperatures with a twofold objective: one, to directly produce a strengthened material with improved fracture characteristics, and two, to identify a ceramic system which would densify at a reasonably low temperature and to which a suitable reinforcement could be added such that the composite thereby produced would be characterized by improved fracture energies.

An experimental processing program was carried out with ZrB<sub>2</sub> as the diboride phase and the metals Fe, Ni, Cr, Ti, and Zr singularly employed as the additive; several experiments were also performed with a metal additive and ZrB<sub>2</sub> + SiC and a metal additive + ZrB<sub>2</sub> with nichrome and stainless steel reinforcement. The principal effect of the metal additions on the processing of zirconium diboride is the lowering of the fabrication temperature needed to effect full densification from the 3800° to 4000°F range required for ZrB<sub>2</sub> with no additives to 2200°F to 3000°F. Unlike the ceramic additives, SiC and C, which effect processing and property improvements for zirconium diboride while maintaining their own identities and not reacting with part of the ZrB<sub>2</sub>, the metal additives with the exception of Zr do react. The materials so processed do not contain the elemental metal additives but rather a compound and/or phase produced by reaction of the additive metal and zirconium diboride. For example, elemental Ni forms a Ni<sub>3</sub>B<sub>4</sub> type phase. A liquid phase is produced during processing and the resulting material is characterized by a dense microstructure of ZrB<sub>2</sub> grains with a distinct grain boundary phase which does not appear to be ductile. Addition of Zr to ZrB<sub>2</sub> does not produce an intermediate phase in agreement with the binary phase diagram (11). In the Zr/ZrB<sub>2</sub> system, enhanced densification and the resulting microstructures for ZrB<sub>2</sub>20Zr and ZrB<sub>2</sub>50Zr, are consistent with the formation of a liquid phase during processing from a metal-rich composition at or above the eutectic temperature. The addition of Ti produced an acicular type phase of extremely fine grain size; the relative amount of the acicular type phase increased with increasing Ti content. Additions of Fe and Cr were the least effective in lowering the processing temperature and were not fully delineated since the resulting materials did not show any substantial improvement in mechanical properties. Attempts to use the ZrB<sub>2</sub>/Ni system as a matrix phase with nichrome or stainless steel wire as a reinforcement were not successful due to alloying of the reinforcement with the intergranular phase at the processing temperatures which were below 2500°F.



The significantly larger W/A values obtained from the impact tests relative to the values from the slow bend tests was investigated by examining the effect of lowering the impacting energy from 32.4 J (24 ft-lbs) to 1.35 J (1 ft-lb). A dramatic decrease in measured impact energy was found with decreased impacting energy to 1.35 J (1 ft-lb) for a given material and a discernable differentiation among the ZrB<sub>2</sub> composites which was absent in the test results obtained using the 32.4 J (24 ft-lbs) impacting energy was observed. Two boride/metal composites were produced with impact properties comparable to those measured for WC6Co. The increased impact resistance was achieved by introducing excess metal in a ZrB<sub>2</sub>/Zr composite and by the production of a fine grained acicular phase in ZrB<sub>2</sub>/Ti composites.

The method for measuring the work of fracture for brittle materials proposed by Tattersall and Tappin (5) was successfully applied to several of the boride composites. Specimen configurations were found which permitted fracture to be initiated at very low loads, and a suitably "hard" testing machine was employed. Conditions for controlled fracture were not achieved for all materials tested. Catastrophic fracture resulted for all conditions used to test WC6Co, diboride VIII(18,10), and the weaker ZrB<sub>2</sub>/Metal composites. Controlled fracture was obtained for diboride VIII(14,30)M2, ZrB<sub>2</sub>30Ti and ZrB<sub>2</sub>50Zr. Semi-controlled fracture was obtained for ZrB<sub>2</sub>20Zr and ZrB<sub>2</sub>20Ni.

Fracture strength data was also obtained for the ZrB<sub>2</sub>/Metal composites. The highest strengths were measured for the ZrB<sub>2</sub>/Ti composites; the strength increased with increases in Ti content in the starting powders which effected an increase in the fine grain acicular phase in the fabricated material. The ZrB<sub>2</sub>30Ti material is characterized by a high fracture strength, 10.2 N/M<sup>2</sup> (150,000 psi), and a measurable degree of toughness demonstrated by controlled fracture with W/2A = 138 J/M<sup>2</sup> (0.79 in-lbs/in<sup>2</sup>). The highest strength diboride developed in the earlier study designed primarily to improve oxidation resistance and thermal stress resistance was  $6.4 \times 10^8$  N/M<sup>2</sup> (94,000 psi) for VIII(18,10) (1). The diboride material VIII(14,30)M2 which was found to provide a measure of resistance to catastrophic crack propagation (8) was characterized in this study by a work of controlled fracture, W/2A, of 88 J/M<sup>2</sup> (0.50 in-lbs/in<sup>2</sup>).

## II. FABRICATION AND CHARACTERIZATION

### A. Introduction

The processing studies are designed to produce boride composites with improved fracture characteristics. Specimen material for the characterization studies is also obtained from commercial suppliers and from billets of boride compositions developed in the earlier boride program (1). The objective of the processing studies is to identify compositions containing  $ZrB_2$  as the principal phase and additives which alone or in a particular combination effect (1) lowering of the processing temperature to the vicinity of  $2500^\circ F$  and (2) strengthening or reinforcement such that impact strength and fracture energies are increased relative to the levels of the diboride materials developed earlier.

During the first year study (6), specimens were obtained from WC6Co, a commercially available, high strength material known to have sufficient toughness to be employed for cutting tools. Test specimens were also obtained from ManLabs' billets of polycrystalline diboride composites containing  $ZrB_2$  with SiC and/or C. In addition, processing experiments afforded  $ZrB_2 + SiC$  composites fabricated with layers of carbon cloth parallel to the diametrical plane of the billet. The use of metal additions for  $ZrB_2$  to lower processing temperatures was initiated with Ni, Fe, and Cr. During the current contract year, the processing studies have centered on the use of Fe, Ni, Ti, and Zr as metal additives. All the metals proved to be effective in lowering the processing temperatures.

### B. Processing Procedures

Billets fabricated for this program are processed in ManLabs' hot pressing facility which consists of a 150 ton hydraulic press in which a graphite die and piston assembly is heated by a 50KW, 3kc motor generator induction heating unit (manufactured by Ajax Magnethermic Corporation).

In practice, the powder constituents are mixed in the desired proportions in air with the exception of Ti and Zr containing compositions which are mixed under argon. Ceramic additives are mixed in a Red Devil oscillating dry solids mixer; the metals, in a dry ball mill. The mixed powders are loaded into a graphite die lined with Grafoil, a Union Carbide product with the consistency of thin aluminum foil but composed principally of pyrolytic graphite. For the refractory compositions containing  $ZrB_2$ , SiC and/or C, the die and piston assembly is heated to the desired temperature with a low holding pressure of 100 psi, then the load is

applied at or near the maximum processing temperature. Temperatures are measured with calibrated optical pyrometers and thermocouples. The processing pressure is released at or somewhat lower than the maximum processing temperature and the assembly slowly cools to ambient due to the size of the graphite die and the insulation needed to prevent attack of the graphite by ambient air. For the most part billets were fabricated of dimensions 3 to 3.5 inch diameter by 0.5 to 1.0 inch high. A reducing atmosphere is generated in the die as CO formed by reaction of the graphite and air is more stable than CO<sub>2</sub>. For the more reactive metals, provision was made during the program to introduce an argon atmosphere during processing. Compositions processed in the atmosphere generated in the hot pressing assembly without the introduction of argon and listed and identified as processed in (air) and those processed in argon are designated (argon).

The temperature, pressures, and times reported for processing conditions are the time at maximum temperature and pressure.

### C. Material Identification

In the earlier development of boride composites containing ZrB<sub>2</sub> with SiC and/or C, a Roman numeral system was developed to designate the volume percentage of SiC and C and to identify the base diboride (1). Thus, the designation VIII (18, 10) identified a ZrB<sub>2</sub> composite with 18 volume per cent SiC and 10 volume per cent C. Two ZrB<sub>2</sub> composites containing higher carbon content in two forms of carbon have been employed in this study. The two materials are designated VIII (14, 30) and VIII (14, 30) M2; characterization data were provided in the earlier report (6). One other ZrB<sub>2</sub>-SiC composition has been studied, namely, the material designated V which contains 20 volume per cent SiC.

For the ZrB<sub>2</sub>/Metal composites the composition is expressed as weight per cent of the additive in the initially mixed powders. Thus, ZrB<sub>2</sub>20Ti identifies a billet hot pressed from 80 weight per cent ZrB<sub>2</sub> and 20 weight per cent Ti. In discussing characterization data below, it will be shown that with exception of the Zr addition, all metal additives underwent chemical reaction with the ZrB<sub>2</sub> during processing leading to one or more binary or ternary phases and in some cases unreacted metal or metal alloys. In contrast, the SiC and C additions do not react to any significant extent and the resulting solid composition approximates closely to the initial powder mix.

Other designations for variations of composition and components are explained where they occur in the text.

#### D. Processing Experiments

Processing data for the  $\text{ZrB}_2/\text{SiC}/\text{C}$  composites were provided in the earlier report which also contained some results for  $\text{ZrB}_2$  with metal additions of Fe, Ni, and Co (6).

Processing conditions and characterization data exclusive of mechanical test data follow for the  $\text{ZrB}_2/\text{Metal}$  systems. However, some mechanical test results are cited in the context of material improvement. Some processing data are repeated from the earlier report (6) to provide a more complete analysis of results.

##### 1. $\text{ZrB}_2/\text{Ti}$ System

Processing conditions for hot pressing runs performed with a Ti additive are provided in Table 1. The early hot pressing runs with additions of 12.5 per cent Ti, HP 116 and HP 118, and 20 per cent Ti, HP 113, showed that a reduction in processing temperature could be effected and that the two levels of Ti addition produced different microstructures, Figures 1 and 2. The impact strength level of the  $\text{ZrB}_2\text{20Ti}$  (HP 113) was not significantly different from that reported earlier for the nine diboride compositions (6). However, the work of fracture, W/A, values obtained from the slow bend tests of specimens from the HP 113 billet were, though somewhat scattered, higher than any obtained then for a boride material (6); the averaged result was  $222 \text{ J/M}^2$  ( $1.27 \text{ in.-lbs./in.}^2$ ). Furthermore, the bend strength at room temperature was  $530 \times 10^6 \text{ N/M}^2$  (77,000 psi) for  $\text{ZrB}_2\text{12.5Ti}$  and  $670 \times 10^6 \text{ N/M}^2$  (97,000 psi) for  $\text{ZrB}_2\text{20Ti}$ , HP 118 and HP 124, respectively.

The  $\text{ZrB}_2/\text{Ti}$  composition was modified to attempt to consolidate a  $\text{ZrB}_2/\text{SiC}$  composition in the same temperature range near  $2750^\circ\text{F}$  which is  $900^\circ\text{F}$  lower than that required for the densification of the  $\text{ZrB}_2/\text{SiC}$  composite (1). The resulting low density billet showed that the addition of SiC to the  $\text{ZrB}_2/\text{Ti}$  composition changes the densification characteristics. The SiC is desirable as this compound is known to effect increased oxidation resistance for  $\text{ZrB}_2$  compositions (1). No further work was done on the effect of metal additions on the densification of  $\text{ZrB}_2/\text{SiC}$  compositions.

Processing data and results are also provided in Table 1 for HP 141, HP 150 A and B, HP 172 A, and HP 172 B. The designations A and B refer to separate billets fabricated in the same processing run; the thickness of these billets is  $1/2$  inch as compared to the 1 inch thick billets generally processed in the program. The results after HP 141 were obtained in the revised processing system with a flowing argon atmosphere to reduce the contamination of Ti. Billets fabricated in the argon atmosphere are noticeably

cleaner on the outside edges. The reductions in CO and O<sub>2</sub> concentrations brought about by the introduction of the argon effectively reduced the amount of contamination of the metal additives during processing. Characterization data relative to phase constitution presented below do not show any significant difference between billets processed in air or in argon.

Additional compositional variations within the ZrB<sub>2</sub>/Ti system were investigated. Billets HP 172 A and HP 172 B were processed with 25 and 30 weight per cent addition of Ti in the starting mixture, respectively. There is an apparent difference in the microstructures for the four ZrB<sub>2</sub>/Ti compositions examined thus far; Figures 1 through 5 provide a direct comparison. Atomic fractions of Ti, Zr, and B are provided for comparison of the observed microstructures which are consistent with the ternary equilibrium phase stability data compiled by Rudy (11). Selected isothermal ternary sections are provided in Figures 6 and 7 to illustrate the possible effect of temperature on processing. The compositions studied from 20 to 30 weight per cent Ti added to ZrB<sub>2</sub> produced three solid phases at equilibrium: ternary diboride (Ti, Zr)B<sub>2</sub>, ternary monoboride (Ti, Zr)B, and Ti(Zr) binary metal alloy while the 12.5 weight per cent composition produced a two phase solid mixture without the ternary monoboride. Examination of the microstructures provided in Figures 1 through 5 shows a consistent increase in the monoboride (presumably a ternary monoboride), the acicular structure, with increase in Ti composition. These microstructures are also discussed in the following description of the detailed characterization data obtained for ZrB<sub>2</sub>20Ti.

X-ray diffraction phase analysis was carried out on samples from billets HP 124, HP 141, HP 150 A, and HP 150 B, all having 20 weight per cent Ti. The results showed ZrB<sub>2</sub> and TiB (orthorhombic) type phases to be the major constituents in all billets. The diffraction data were not analyzed to the detail required to distinguish the binary monoboride (TiB) and diboride (ZrB<sub>2</sub>) from the equilibrium ternary phases discussed above. There was some indication of an fcc phase consistent with the pattern for ZrC. A number of unidentified lines were also found in all the diffraction patterns. One or two of these are consistent with a pattern for a TiB fcc or  $\alpha$ -Zr type phase, but sufficient data are not available for firm identification. The rest of the lines are most probably caused by the presence of oxides. Only HP 124 showed a questionable but possible trace of Ti. In general, no significant differences were found to exist in the phases detected.

Several different techniques of electron microprobe analysis were employed for detailed characterization. Spectral scans were run to determine the elements present over a multi-phase area.

Scanning display photographs were obtained to correlate the distribution of Zr and Ti with the observed microstructures. Finally, distribution scans were carried out to monitor variations of the two elements within each phase field. Samples from HP 124, HP 141, and HP 150 B were analyzed. The spectral scans showed similar amounts of Zr and Ti plus a small amount of Hf in all three samples. No other impurity elements were detected, although it should be noted that elements with atomic numbers below Na (11) could not be detected with this type of analysis thus eliminating carbon, oxygen and boron.

Figures 8 through 20 illustrate the results of scanning display studies on selected areas of the three samples. Figures 8 through 11 for HP 124 show a photomicrograph of the area displayed, a sample current display of the area showing pertinent features as distinguished by variations in electrical conductivity, topography and elements present in the different phases, and X-ray display photographs of the same area for the Zr-L $\beta$ (1) and Ti-K $\alpha$ (1) lines respectively. Figures 12 through 16 for HP 141 and Figures 17 through 20 for HP 150 B give similar information. It clearly appears that a distinct separation exists between Ti-rich and Zr-rich areas in all three samples. The Ti-rich TiB-type phase appears as large acicular areas surrounded by the typically blocky ZrB<sub>2</sub> grains as illustrated in Figures 8, 12, 13, and 20 (see also Figures 1 through 5). It also appears that the Ti-rich phase or phases are constituents of the grain boundaries between the ZrB<sub>2</sub> grains. Unfortunately, no distinction between Ti and Zr as elemental or as borides can be made due to the lack of sensitivity of detection.

The distribution scans were made by monitoring the intensities of Ti and Zr as the samples were moved relative to the electron beam. These results generally support the scanning display results and show distinct separations between the Ti-rich and Zr-rich areas, with some Ti at grain boundaries and extremely isolated patches of Zr-rich phase within the acicular Ti-rich areas.

Thus, the Ti addition to ZrB<sub>2</sub> produces the monoboride (Ti, Zr)B at the expense of the B in ZrB<sub>2</sub>. Since there is no monoboride in the Zr-B system, the depletion of B from ZrB<sub>2</sub> produces elemental Zr which alloys with elemental Ti. On the basis of the equilibrium phase diagram, some of the Ti also alloys with ZrB<sub>2</sub> producing the ternary diboride and elemental Zr which as above alloys with Ti. The compositions with 25 and 30 weight per cent Ti, HP 172 A and 172 B, produce a more uniform distribution of the three phases. The overall amount of the ZrB<sub>2</sub>-type phase appears smaller in the ZrB<sub>2</sub>25Ti and the ZrB<sub>2</sub>30Ti than in the ZrB<sub>2</sub>20Ti.

## 2. ZrB<sub>2</sub>/Zr System

Processing conditions and resulting density data obtained for all hot pressings of the ZrB<sub>2</sub>/Zr compositions are provided in Table 2. The composition with 20 weight per cent Zr was the primary material considered. Processings were performed in air and in argon. The large increase in Zr content to 50 weight per cent was designed to attempt to improve the impact strength and the work of fracture by introducing an excess of ductile phase.

The microstructures of billets HP 126, HP 144, and HP 174 A are provided in Figures 21, 22, and 23, respectively. The microstructures of HP 126 and HP 139 are equivalent. Comparison of billets HP 126 and HP 144 shows that a more uniform distribution of metal around metal diboride was obtained in the earlier pressing, HP 126. One reason for reprocessing this composition in HP 144 was to compare material processed in air versus argon; the poor mixing could possibly override the beneficial effect of the argon as explained in the discussion of the fracture strength data. A better distribution of the metal and ceramic phase was obtained in HP 174 A and B. The distribution of the two phases is also less than desirable in ZrB<sub>2</sub>50Zr, HP 152 A and B, Figure 24.

X-ray diffraction phase analysis studies were carried out on samples from billets HP 126 and HP 144 and HP 152 A and B. The results in all cases showed ZrB<sub>2</sub> and Zr metal as the principal phases. A small amount of ZrC was detected in HP 126, which was pressed at a higher temperature than the others and was fabricated before the argon atmosphere was incorporated in the processing cycle. Possible traces of ZrC might exist in the ZrB<sub>2</sub>50Zr, but this could not be definitely concluded. Only three unidentified lines were observed in these diffraction patterns and these generally correspond to some of the lines observed in the Ti series. The probability is thus good that these unexplained lines represent traces of a Zr-rich phase, possibly an oxide.

Electron probe microanalysis of this series was limited to spectral scans to determine elemental impurities. Only a small quantity of Hf was detected in all cases. Scanning display was attempted but no variation in Zr could be detected due to its extremely high concentration in both phases. However, the microstructure shown in Figure 21 clearly illustrates the Zr metal distributed between the typically blocky ZrB<sub>2</sub> grains.

## 3. ZrB<sub>2</sub>/Ni System

Several hot pressing runs were previously performed for the ZrB<sub>2</sub>/Ni system. The significant finding from the processing experiments was the observation that in the hot pressing at-

mosphere elemental Ni reacted with  $\text{ZrB}_2$  at moderately low temperatures,  $2400^\circ\text{F}$ , producing a liquid phase which appeared to wet the remaining  $\text{ZrB}_2$  grain boundaries. Upon cooling, the resulting grain boundary phase was identified by X-ray diffraction as a  $\text{Ni}_3\text{B}_4$  type phase, probably a ternary phase containing Zr also. Processing experiments were carried out in the temperature range from  $2400^\circ\text{F}$  to  $3000^\circ\text{F}$ ; densification was accomplished by weight reduction in the powder charge, and at the higher temperature a nickel-rich material extruded from the billet during processing. The measured mechanical properties of the  $\text{ZrB}_2/\text{Ni}$  composite were consistent with the formation of a brittle intermetallic grain boundary phase (6).

Processing conditions and resulting densities are provided in Table 3 for two new hot pressings of  $\text{ZrB}_2/20\text{Ni}$ . In both cases, there was a weight loss during processing. The initial weight of  $\text{Ni} + \text{ZrB}_2$  for the 1/2 inch high billet is 475 grams; the final weight for HP 153 is 414 grams, for HP 174 448 grams. The processing temperature for HP 174 was lowered to attempt to avoid the weight loss and possibly reduce the apparent reaction of Ni and  $\text{ZrB}_2$  to produce a  $\text{Ni}_3\text{B}_4$  type phase which is probably a ternary compound as no indication of either elemental Ni or Zr has been found in the X-ray work. Electron probe microanalysis has confirmed the presence of Ni in the fabricated billets and the microstructures shown in Figures 25 and 26 clearly show a grain boundary phase. The morphology of the latter appears somewhat different for HP 174 versus HP 153.

#### 4. $\text{ZrB}_2/\text{Ni}$ : Reinforcement Systems

Since the  $\text{ZrB}_2/\text{Ni}$  system permits densification at temperatures of  $2200^\circ\text{F}$  with the formation of an intermetallic grain boundary phase, this system was employed together with nichrome and stainless steel wire mesh to attempt to produce reinforced materials with increased impact strength and fracture energies.

The experimental conditions employed and the characteristics observed for the resulting billets are provided in Table 4. The matrix phase was selected on the basis of the low processing temperatures required to effect densification; the reinforcements, on the basis of anticipated chemical compatibility and retained mechanical integrity. The latter aspect is supported in part in the reported retention of ductility in nichrome wire mesh in hot pressed reinforced alumina (12).

The processing cycles, HP 127, HP 131, and HP 134, were performed at decreasing maximum hot pressing temperatures using nichrome wire mesh (20 mesh, 0.016 inch diameter wire) as the potential reinforcement. The overall result is a chemical degrada-



tion of the reinforcement due to reaction with the matrix system. The same result was obtained for HP 138 in the attempt to use a stainless steel wire mesh (20 mesh, 0.016 inch diameter wire). The nature of the chemical interaction was not studied in detail. The microstructural features of the materials produced in the attempted hot pressing of the wire reinforced  $\text{ZrB}_2\text{20Ni}$  are provided in Figures 27 through 30. The principal feature of the microstructures is the presence of the grain boundary phase which appears to have wetted the  $\text{ZrB}_2$  grains.

A similar type of microstructural feature was observed for hot pressed  $\text{ZrB}_2\text{20Ni}$  with no reinforcement, Figures 25 and 26. However, the relative amounts of the grain boundary phase appear to be larger in the microstructures of the  $\text{ZrB}_2\text{20Ni}$ /Reinforcement billets shown in Figures 27 through 30. This observation is consistent with the apparent reactions of the reinforcements with the  $\text{ZrB}_2\text{20Ni}$  matrix.

#### 5. $\text{ZrB}_2/\text{Fe}$ System

In the earlier studies of the effect of Fe additions on the densification of  $\text{ZrB}_2$ , compositions containing a ten per cent addition were processed. Temperatures near  $3000^\circ\text{F}$  were required to effect significant densification. Characterization data showed that  $\alpha\text{Fe}$  was present and located at the  $\text{ZrB}_2$  grain boundaries in the microstructure (6). Experiments with Fe addition were extended to 20 and 30 weight per cent in the present investigation. The maximum processing conditions for the hot pressing conditions are provided for all the  $\text{ZrB}_2/\text{Fe}$  compositions studied in Table 5; billet absolute densities and the per cent of starting powder density are also tabulated. The microstructural features of the four billets are provided in Figures 31 through 34; additional characterization data are also provided thereon. In examining the results of the processing conditions on the initially mixed powders, the absence of any attempt to provide an inert gas at this time in the processing study during mixing or processing should be considered. This aspect of the hot pressing equipment was subsequently modified and facilities for processing under an inert atmosphere were installed.

Examination of the processing conditions and density and characterization data, Table 5 and Figures 31 through 34, reveals that an iron addition can promote densification at temperatures as low as  $2515^\circ\text{F}$ . This effect was observed for the 30 weight per cent addition. The first assessment of the observed behavior for the Fe addition is that the 30 weight per cent level used to effect the significant reduction in processing temperature would probably seriously degrade the thermochemical stability. The behavior of the Fe is quite different from that observed for nickel which ef-

fecting a reduction of processing temperature to 2420°F by way of liquid phase reaction to form  $\text{Ni}_3\text{B}_4$ . The microstructures provided in Figures 31 through 34 do not show evidence for extensive liquid phase formation. The density and X-ray data are consistent with retention of elemental iron in the hot pressed  $\text{ZrB}_2/\text{Fe}$  composites; all materials appear to be ferromagnetic.

#### 6. $\text{ZrB}_2/\text{Cr}$ System

This system was examined in the earlier study (6) using a 10 weight per cent addition. Temperatures of the order of 3200°F were required to effect high densification. The Cr did not form a liquid phase during processing; a discrete intermetallic B-Zr-Cr ternary phase would be anticipated on the basis of equilibrium considerations. The observed mechanical properties are consistent with the absence of a ductile metallic phase and the presence of a material constituted primarily of brittle components, namely,  $\text{ZrB}_2$  and the Cr intermetallic compound. No further work was performed with this system.

#### 7. Diboride Materials V, VIII(14,30)M2, and VIII(18,10)

New mechanical data are presented for three of the polycrystalline diboride materials developed in an earlier program(1). Characterization data and mechanical test results were presented for two of these materials in the previous report (6). Material VIII(18,10) was included in the program in the second year study. Microstructural data and other information for VIII(18,10) is provided in Figure 35. The VIII(14,30)M2 material was obtained from large NP6M2 and NP7M22 billets, fabricated under the support effort for a diboride test hardware program (8). Microstructural data and other information are provided in Figure 36. There is some anisotropy in this composition. Material V, the  $\text{ZrB}_2$  20 volume per cent SiC composite was described in the earlier report (6); a microstructure is provided for direct comparison in Figure 37.

#### 8. WC6Co

New mechanical data are presented for WC6Co. The material was procured as before as the dense, sintered material supplied to cutting tool manufacturing companies. The material is a dense, fine grained, polycrystalline material with a metallic, skeletal phase which provides strength reinforcement. A representative microstructure is provided in Figure 38.

### III. MECHANICAL CHARACTERIZATION: STRENGTH AND WORK OF FRACTURE

#### A. Introduction

An increasing amount of attention is now being focused by ceramists on the measurement of parameters related to fracture toughness of brittle materials and composites containing brittle reinforcing agents in a metallic or resin matrix. Much of the earlier work in the measurement of surface energy for ceramic materials is reviewed and discussed in a compendium published by the Defense Ceramic Information Center (13). A companion compendium relating to the evaluation and interpretation of mechanical properties of brittle materials was also prepared (14). For ceramics in general, the quantity designated work of fracture is determined from a slow bend test of a notched bar in three-point bending using a geometry such that controlled fracture is obtained. When a suitable geometry is found, the work of fracture normalized for twice the cross sectional area under the crack (or the total area of surface generated) is designated  $W/2A$  and is considered as the surface energy, provided that the elastic energy stored in the specimen and in the test machine are either not significant or calculable. In the latter, the work of fracture can be corrected for these measurement artifacts and the surface energy determined.

In metallurgical data reporting, the work of fracture is designated as  $W/A$  and the specimens are notched and pre-cracked (7a, 7b). Impact tests of subsized Charpy specimens of metals provide  $W/A$  values comparable with  $W/A$  determined from slow bend tests. The magnitude of such values are however considerably higher than those measured for ceramic materials,  $W/A$  for H11(187.4) steel is  $175,000 \text{ J/M}^2$  ( $1000 \text{ in-lbs/in}^2$ ) from impact measurements and  $171,500 \text{ J/M}^2$  ( $980 \text{ in-lbs/in}^2$ ) from slow bend measurements (7b). In general, the  $W/A$  values obtained for other steels, aluminum alloys, and titanium alloys show a similar trend; that is, values obtained from impact tests are higher than values obtained from slow bend tests. The largest difference was approximately a factor of two (7b). For polycrystalline alumina, a typical ceramic material, Davidge and Tappin (15) report a surface energy of  $66 \text{ J/M}^2$  ( $0.38 \text{ in-lbs/in}^2$ ) determined from a slow bend test under conditions of controlled fracture.

During the first year of this study, mechanical characterization data obtained for a tough WC6Co tool material and for boride composites included fracture strength for unnotched specimens and fracture energies or better work of fracture for notched specimens of equal dimensions tested by impact and slow bend methods. For the latter measurements, data was collected using a "soft" hydraulic test machine under conditions such that catastro-

phic failure occurred. The impact measurements were made with a pendulum type instrument which provided an impacting energy of 31.5J (24 ft-lbs). A measurable difference was observed between the WC6Co material and the refractory oxidation resistant boride material (6). For WC6Co the impact fracture energy expressed as  $W/2A$  was  $6475 \text{ J/M}^2$  ( $37 \text{ in-lbs/in}^2$ ) and the slow bend measurements yielded  $W/2A = 228 \text{ J/M}^2$  ( $1.3 \text{ in-lbs/in}^2$ ). For nine diboride composites the impact fracture energies expressed as  $W/2A$  varied from 1490 to  $2450 \text{ J/M}^2$  (8 to 14 in-lbs/in<sup>2</sup>); the slow bend values from 35 to 115  $\text{J/M}^2$  (0.20 to 0.66 in-lbs/in<sup>2</sup>). The large difference between  $W/2A$  obtained from impact and slow bend tests was noted and compared with the smaller difference observed for metals for which the magnitude of  $W/2A$  is considerably larger, e.g. 87,500  $\text{J/M}^2$  (500 in-lbs/in<sup>2</sup>).

## B. Experimental Test Procedures

### 1. Impact Apparatus

Impact tests were conducted with a ManLabs Model CIM-24 Impact Tester. This instrument has a compound pendulum (sector of circle) with a maximum capacity of 31.5 J (24 ft-lbs) and a corresponding impact velocity of 348 cm/sec (11.4 ft/sec). The accuracy and precision of measurement of this instrument are within 0.014 J (0.01 ft-lbs). The specimen size used for these tests is as the ASTM standard charpy, 1.00 cm square by 5.00 cm long (0.394 inch square by 2.165 inch long), some tests being conducted with modified notches (e.g. saw cut to various depths).

Tests were also conducted with a modified CIM-24 Impact Tester, such that the capacity of the instrument could be reduced to one foot-pound while the impact velocity decreased to a corresponding low of 70 cm/sec (2.3 ft/sec).

The parameter actually measured with the impact test instrument is the angular position to which the pendulum rises after impacting the specimen. This value is then translated into the energy transferred to the specimen. This energy is usually considered to be the impact work of fracture for the specimen.

### 2. Slow Bend Apparatus for Work of Fracture

Slow bend tests were conducted with two different instruments: a ManLabs Model SB-750 Slow Bend Machine and a Baldwin Tate-Emery Universal Testing Machine. The ManLabs Slow Bend Machine is designed to accept ASTM standard charpy specimens. The tup is driven toward the anvil at constant speed by an electric motor, gear train, and lead screw. Consequently, the specimen is subjected to three-point bending with a constant rate of deflection. This machine is quite "hard," relative to the loads required

to fracture the ceramic type specimens, and very little energy is stored in the machine relative to the elastic energy stored in the specimen.

During operation of the "hard" slow bend instrument, the parameters measured are two electrical signals (voltage): one from a strain gage circuit, which is proportional to the load on the specimen; the other from an electrical circuit, which is proportional to time. The product of these signals is integrated electrically and displayed as a reading proportional to the work (integral of force times distance) done by the machine in fracturing the specimen. Work of fracture for the specimen is obtained by appropriate conversion factors related to load range and deflection rate for the particular test. A graphical presentation of load versus time (time is proportional to deflection for this constant deflection rate machine) is also obtained so that the fracture work may also be determined by graphical integration (e.g. planimeter). With an accessory kit using a more sensitive load cell, more precise data can be obtained but at a sacrifice in machine hardness.

Slow bend tests conducted in the Baldwin machine were performed with a three-point bend test fixture. The shape and dimensions of the anvil and tup are essentially as for the ASTM charpy specimen. The machine is set up for compression of the fixture between the platen and the fixed crosshead. The Baldwin machine is loaded by hydraulic pressure in a piston-cylinder arrangement. This machine is used as a constant loading rate device, during testing. Because the oil used for pressurizing the cylinder is of relatively low modulus, this machine is "softer" than the ManLabs slow bend machine; that is to say it has more elastic energy stored in the machine relative to that stored in the specimen.

During the test, the parameters measured are the pressure in the loading circuit (pressure is proportional to load) and an electrical signal from a dilatometer (voltage proportional to deflection). These signals are plotted by an X-Y recorder to give a graphical presentation of load versus deflection. The work of fracture is obtained by graphical integration (e.g. planimeter) of the load versus deflection plot.

### 3. Fracture Strength Apparatus

Fracture stress measurements were performed at a constant rate of loading with the Baldwin machine cited above. Specimens of 4.45 cm length by 0.508 cm width by 0.254 cm thickness (1.75 in x 0.200 in x 0.100 in) were prepared with a 0.013 cm (0.005 in) radius along two edges of one side running the length of the specimen. Specimens were loaded to failure in four-point

bending with a support span of 4.12 cm (1.62 in) and a load span of 2.005 cm (0.79 in). Earlier reported fracture strengths were obtained in three-point bending (6).

### C. Test Results

#### 1. Impact Test Results

Impact test data were obtained for the most part with the ASTM subsized Charpy configuration described in the earlier report (6) using the 32.4 J (24 ft-lbs) capacity machine. Some measurements were also made using specimens of the same overall dimensions but with saw cuts employed to replace the V-notch which requires EDM machining procedures or with thickness variations for the same height and depth of notch. In addition, some measurements were performed with ASTM subsized Charpy specimens using 1.35 and 2.70 J (1 and 2 ft-lbs) incident impacting energies. All impact test specimen configurations used are shown in Figure 39.

The measurements at the lower incident impacting energy were introduced late in the program to attempt to obtain data under impact conditions such that the measured work of fracture would be a larger fraction of the impacting energy. Multer (16) reported substantial reduction in measured impact fracture energies for several ceramic materials tested using a variation of ASTM D256 in which the position of the impacting hammer of total weight, 0.37 and 0.74 kilograms (1 and 2 pounds), was varied to reduce the tossing of the ceramic specimen.

Impact testing results obtained using a specimen undersized in width but otherwise conforming to the ASTM notch configuration and the full impacting capacity of 32.4 J (24 ft-lbs) are provided in Tables 6 and 6MKS. The data were collected to check the testing procedure by reducing the area under the notch by a factor of two. Three materials were selected for testing: the WC6Co tool material, the Boride V material ( $\text{ZrB}_2 + \text{SiC}$ ), and Boride VIII M2 ( $\text{ZrB}_2 + \text{SiC} + \text{C}$ ). The data provided in Table 6 are normalized for the unit area, A, under the notch. The normalized impact energy values for the two specimen widths are in satisfactory agreement, although a somewhat lower value was obtained for the smaller specimens of the WC6Co material. Analogous data obtained using the slow bend test procedures which were followed earlier showed a more uniform agreement for the same three materials (6). On the basis of the impact and the then-available slow bend test results for three different materials using specimens differing in area by a factor of two, it was concluded that both methods were reliable

and reproducible. The matter of the large difference in the magnitude of the work of fracture as calculated from the impact results and slow bend test results, however, remained unexplained.

During the second year of the study, the fabrication effort shifted emphasis to the  $\text{ZrB}_2$ /Metal systems. It was anticipated that addition of excess metal would improve impact properties, and compositions were designed to attempt to realize such improvement without considering other properties, particularly thermal properties which would be degraded.

In the results obtained in the fabrication study, it was shown that 30 weight per cent of Fe was required to lower the fabrication temperature from the 3000°F range required for the 10 and 20 per cent Fe additions to 2500°F, Table 5. Impact data obtained earlier (6) for the 10 weight per cent composition and new data for the 20 and 30 weight per cent compositions are provided in Tables 7 and 7MKS. No improvement in measured impact energy was noted for the relatively large amount of Fe, although slow bend test data presented in the following subsection did appear to show some improvement relative to levels measured for the oxidation resistant  $\text{ZrB}_2 + \text{SiC}$  compositions such as Boride V.

Individual additions of Ti and Zr to  $\text{ZrB}_2$  produced favorable fabrication effects as shown in the previous section, II-D. Impact tests were conducted along with slow bend tests to assess the work of fracture, and fracture strength tests were also performed as discussed in the following subsections, III-C-2 and III-C-3, respectively. Fracture strengths approaching  $6.5 \times 10^8 \text{ N/M}^2$  (100,000 psi) were measured for a  $\text{ZrB}_2\text{20Ti}$  composition (20 weight per cent Ti). Somewhat lower values of fracture strength were measured for a  $\text{ZrB}_2\text{20Zr}$  composition,  $5.5 \times 10^8 \text{ N}^2/\text{M}^2$  (80,000 psi); a  $\text{ZrB}_2/\text{Zr}$  composition was fabricated with 50 weight per cent Zr in anticipation of improved impact properties. The results obtained for the  $\text{ZrB}_2\text{20Ti}$  composition using two fabrication procedures as discussed in Section II and for the  $\text{ZrB}_2\text{50 Zr}$  composition are provided in Tables 8 and 8 MKS. The measured impact energy for  $\text{ZrB}_2\text{50Zr}$ , 5250 J/M<sup>2</sup> (30 in-lbs/in<sup>2</sup>) was somewhat higher than any similarly measured in this program except for WC6Co. The previously-highest measured value of 4820 J/M<sup>2</sup> (27.5 in-lbs/in<sup>2</sup>) was obtained for a Boride V composition modified with layers of carbon cloth (6). The low measured impact energies for  $\text{ZrB}_2\text{20Ti}$  compositions were in sharp contrast to their high fracture strengths.

Impact data for the diboride composite, VIII(18,10), was obtained with the full machine capacity of 32.4 J (24 ft-lbs) to complement similar data for other boride composites. The results in Tables 9 and 9 MKS show the same level of impact energy,

0.29 J (0.21 ft-lbs), that was measured for other boride composites. The bend strength values of VIИ(18,10) were among the highest measured in the earlier diboride development program (1), and it was anticipated that somewhat higher work of fracture values, W/A, should result for this material. The W/A obtained from impact tests at 32.4 J (24 ft-lbs) does not appear to show the anticipated increase.

A series of impact test specimens were obtained from billets fabricated in the attempts to reinforce the  $\text{ZrB}_2$ -Ni matrix with nichrome and stainless steel wire. It was anticipated that the excess metal would improve the impact resistance. Measurements performed with the full capacity of 32.4 J (24 ft-lbs) failed to show a measurable increase in impact energy, Tables 10 and 10 MKS.

Although the precision of the impact energies measured using the 32.4 J (24 ft-lbs) impacting energy appear to be satisfactory, the experimental test procedure was modified to reduce the impacting energy to levels of 1.35 and 2.70 J (1 and 2 ft-lbs) so that the measured impact energies, which are of the order of fractions of a Joule, would be a considerably larger part of the total impacting energy. Tests were performed for five materials, WC6Co, two  $\text{ZrB}_2/\text{SiC}/\text{C}$  composites,  $\text{ZrB}_220\text{Zr}$ , and  $\text{ZrB}_250\text{Zr}$ . The results provided in Tables 11 and 11 MKS show a considerable decrease in the magnitude of the measured impact energy for decreased impacting energy. Results of data obtained at 32.4 J (24 ft-lbs) incident energy are also provided in Table 11 for direct comparison. The overall results are consistent with the findings of Multer (16), who reported impact energies of 0.30 J (0.22 ft-lbs) and 0.054 J (0.04 ft-lbs) for 1.27 cm x 1.27 cm (0.50 in x 0.50 in) square unnotched bars for polycrystalline SiC tested at full capacity of 2.70 J (2 ft-lbs) and under conditions such that tossing was eliminated, respectively. Multer followed ASTM-D256 except for the lower incident impacting energy.

The precision of the new impact data reported herein for low incident impacting energy does not have the same relative precision as the data obtained at 32.4 J (24 ft-lbs). Since the new data were obtained near the end of the program, an insufficient number of test specimens were available to establish uncertainty limits. The trend in results for the five different types of materials is however conclusive and part of the previously reported (6) large difference in work of fracture, W/A values, calculated from impact and slow bend tests appears to have been resolved.



## 2. Slow Bend Test Results

Slow bend tests were performed from the outset of the study to attempt to measure the fracture energy as an important material characteristic in general and as an indicator of material improvement effected by the compositional and fabrication variations in the processing study described in Section II of this report.

Two measuring techniques were employed to attempt to obtain accurate data suitable for the various analytical procedures employed to calculate fracture energies of brittle materials (5). Both techniques employed specimens of 1 cm x 1 cm (0.394 in x 0.394 in) cross section by 5 cm (2.165 in) long with one or more notch configurations. The majority of the data collected was obtained with a "soft" testing machine, the Baldwin Tate-Emery Universal Testing Machine, described in Section III-B-2, using specimens with a 45° V-notch of 0.032 cm (0.080 in) depth. In the later stages of the second year of the program, an effort was expended to obtain analogous data using the "hard testing machine," ManLabs Model SB-750 Slow Bend Machine also described in Section III-B-2, using in addition to the same V-notched configuration, saw kerfs of 0.032 to 0.635 cm (0.080 to 0.250 in) depth, and chevron configurations of the type described by Tattersall and Tappin (5) and commonly used for ceramic materials.

The "soft machine" was originally selected on the basis of the measured differences in work of fracture,  $W/A$ , for WC6Co (455 J/M<sup>2</sup>) and several boride composites (70 to 277 J/M<sup>2</sup>), and on the agreement in  $W/A$  values found for WC6Co and diboride composites V and VIII(14,30)M<sub>2</sub> measured with 1/2 the cross sectional areas under identical V-notches (6). The measurement technique was accepted although the test conditions and the specimen configuration did not allow a controlled fracture to occur. The measured quantity was identified as the slow bend fracture energy for a unit surface of a single cross-sectional area,  $W/A$ . It was anticipated that the  $W/A$  quantity was greater than polycrystalline surface energy, but the immediate problem appeared to be the much larger  $W/A$  values obtained from impact tests, which at that time were obtained using the full 32.4 J (24 ft-lbs) machine capacity. Thus for WC6Co,  $W/A$  from impact tests was 12,950 J/M<sup>2</sup> and for the boride composites was of the order of 3,000 J/M<sup>2</sup>. The results of slow bend tests obtained with the "soft machine" are presented in Tables 12 and 12 MKS for ZrB<sub>2</sub>/Fe and ZrB<sub>2</sub>/Cr composites, and in Tables 13 and 13 MKS for ZrB<sub>2</sub>/Ti and ZrB<sub>2</sub>/Zr composites and diboride VIII(18,10). The results from the "soft machine" produced values of  $W/A$  which are now designated as work of fracture and which appear to show some differentiation among the ZrB<sub>2</sub>/Metal composites and the oxidation resistant ZrB<sub>2</sub>/SiC/C composites. In particular, the ZrB<sub>2</sub>10Fe

and  $\text{ZrB}_2\text{10Cr}$  composites afforded W/A values less than the VIII(18,10); the  $\text{ZrB}_2$  composites with 20 and 30 weight per cent Fe, 12.5 and 20 weight per cent Ti and 20 weight per cent Zr showed W/A values greater than those measured for VIII(18,10). A comparison of the somewhat higher W/A values listed for  $\text{ZrB}_2\text{20Ti}$  in Tables 13 and 13MKS with the W/A values calculated from impact tests at low impacting energies indicates a much closer agreement than previously obtained when W/A values were calculated from impact tests using the 32.4 J (24 ft-lbs) capacity of the machine. Since the "soft" slow bend tests were known to produce W/A values which were somewhat uncertain due to the occurrence of catastrophic fracture coupled with energy absorption by the "soft" test apparatus, it was decided to attempt to perform some measurements using a "hard testing Machine" and to explore the feasibility of fabricating a test specimen such that controlled fracture could occur.

The ManLabs Model SB-750 Slow Bend Machine, as described in Section III-B-2, was employed with the same specimen geometry and V-notch configuration used for the earlier reported measurements for the soft testing machine; several variations of notch configuration were explored to obtain experimental conditions such that controlled fracture resulted. The initial tests with the "hard" machine were performed with the same V-notch configuration employed for tests using the "soft" machine. Several materials were tested including WC6Co, VIII(14,30)M2, and several  $\text{ZrB}_2$ /Metal composites. Catastrophic failure was observed for all materials tested with the 0.032 cm (0.080 in) deep V-notch and slight variations thereof. Typical curves for WC6Co, VIII(18,10), VIII(14,30)M2, and  $\text{ZrB}_2\text{20Zr}$  are provided in Figure 40. The data and results are provided in Tables 14 and 14 MKS.

The results show equivalent work of fracture for  $\text{ZrB}_2\text{20Ti}$  and WC6Co. This boride composite is somewhat higher in fracture strength,  $6.8 \times 10^8 \text{NN/M}^2$  (100,000 psi), than the other  $\text{ZrB}_2$ /Metal composites, as discussed in the following subsection. The pronounced increase in work of fracture measured for  $\text{ZrB}_2\text{50Zr}$ , albeit the slight variation in the angle of the notch, is consistent with the high amount of elemental zirconium in the processed material.

A comparison of the results of slow bend tests of V-notched specimens conducted with a "hard" and a "soft" apparatus is provided in Tables 15 and 15 MKS. The resulting W/A values from the two test procedures are of the same magnitude. The values obtained from the "hard" test apparatus are consistently higher for all the materials tested by both methods. If the difference between the two test procedures was entirely due to the "soft" nature of the hydraulic testing machine, then the values obtained from the "soft" machine would be larger than those obtained from the "hard" machine. The difference in such circumstances is due to an energy loss due

to energy stored in the soft machine. In the description of the test apparatus in Section III-B-2, a second difference between the "hard" and "soft" machines was noted; namely, the loading mechanisms differ. The "soft" machine uses a constant rate of loading; the "hard" machine, a constant rate of deflection. The overall results in Tables 14 and 14 MKS, and in Tables 11 and 11 MKS show a somewhat better agreement in the magnitude of the W/A values obtained from "hard" slow bend tests and impact tests conducted with impacting energies of 1.35 to 2.70 J (1 to 2 ft-lbs).

Further experimentation was conducted with the "hard" testing apparatus to attempt to obtain conditions such that controlled fracture would occur. The specimen configurations shown in Figure 41 were employed to minimize the load required to initiate crack growth. The specimen design was taken from that employed by Tattersall and Tappin (5) who were successful in producing controlled fracture in polycrystalline aluminas. The initial experiments were conducted with the VIII(14,30)M2 ZrB<sub>2</sub>/SiC/C composite which was developed earlier and found in practice to exhibit crack arresting properties. A subscale component developed a stable crack in a series of thermal cycling tests (8). The VIII(14,30)M2 material is a low modulus,  $2.0 \times 10^{11}$  NN/M<sup>2</sup> ( $30 \times 10^6$  psi), and moderately low strength,  $2.0 \times 10^8$  NN/M<sup>2</sup> (30,000 psi), boride composite with a graphite morphology which could effect crack arrestment. Properties are provided in Section II-C-7 and Figure 136. The first experiments were conducted with the triangulated chevron configuration "A" shown in Figure 41 which effectively provides a stress concentration at the apex with approximately three-fourths of the cross sectional area available for fracture surfaces. The stress concentration was effective in lowering the load required to initiate fracture; however, sufficient elastic energy was stored in the specimen so that a catastrophic fracture occurred. The measured W/A value was 306 J/M<sup>2</sup> (1.74 in-lbs/in<sup>2</sup>) compared to 420 J/M<sup>2</sup> (2.4 in-lbs/in<sup>2</sup>) obtained from the catastrophic failure of the V-notched specimen tested in the same "hard" apparatus. The reduction in W/A for the specimen with the shallow triangulated notch configuration A is consistent with a decrease in stored elastic energy in the specimen. The decrease, however, appears to be insufficient to prevent catastrophic failure once the fracture is initiated. Utilization of the deeper notched chevron configuration "B", in which one-fourth of the cross sectional area is available as fracture surface, produced a controlled fracture for VIII(14,30)M2; duplicate tests were in close agreement with an average W/A = 173 J/M<sup>2</sup> (0.99 in-lbs/in<sup>2</sup>). The "hard" test apparatus was modified to allow the use of a more sensitive load cell while maintaining the constant rate of deflection. This modification permits a more sensitive measurement of the integrated area of the load deflection data, and consequently a more precisely measured energy term. The increase in sensitivity however is accompanied by a reduction in the "hardness" of the test

machine. Specimens tested with configuration B underwent a semi-controlled fracture with somewhat higher W/A values. Duplicate measurements afforded  $W/A = 249 \text{ J/M}^2$  (1.42 in-lbs/in<sup>2</sup>). The increase in measured energy is consistent with the decrease in hardness of the test apparatus. The three curves in Figure 42 provide a graphical description of the three fracture conditions: catastrophic, semi-controlled and controlled. Similar curves were shown by Nakayama (17) for brittle material failure. The variation of fracture made from controlled to semi-controlled with decrease in test machine "hardness" was also observed by Tattersall and Tappin(5) for alumina.

Several ZrB<sub>2</sub>/Metal composites were tested with the configuration B. Controlled fracture was observed for a ZrB<sub>2</sub>30Ti composite and semi-controlled fracture was observed, or at least indicated, for ZrB<sub>2</sub>20Zr and ZrB<sub>2</sub>20Ni. The results of all tests performed with the notch configurations A and B are provided in Tables 16 and 16 MKS. The highest controlled work of fracture values were obtained for ZrB<sub>2</sub>30Ti,  $W/A = 278 \text{ J/M}^2$  (1.59 in-lbs/in<sup>2</sup>). Data presented in the following subsection show that this material is characterized by a transverse bend strength of the order of  $10.2 \times 10^8 \text{ N/M}^2$  (150,000 psi). This is the highest strength measured in the program; of all the materials evaluated, only WC6Co has a higher strength. Where comparable data are available, the W/A values calculated from experiments in which controlled fracture occurred are less than those calculated from experiments in which catastrophic failure occurred. This behavior is consistent with the presence of excess stored elastic energy in the specimens which undergo catastrophic fracture. From these considerations, W/A values calculated from impact tests should always be larger than those calculated from slow bend tests under controlled fracture conditions. In addition to excess stored elastic energy, impact test specimens will lose energy from vibration and kinetic energy considerations.

### 3. Fracture Strength Test Results

Fracture strength measurements using four point bending were introduced in the course of the program when the apparent insensitivity of the full capacity, 32.4 J (24 ft-lbs), impact test method for the ZrB<sub>2</sub> composites was found. Earlier data using three point bending was previously reported for the ZrB<sub>2</sub>/SiC/C composites (6).

The measurements were conducted using the apparatus and specimen configuration described in Section III-B-3. The results are tabulated in Tables 17 and 17 MKS.

The available fracture strengths appear to provide a differentiation among the ZrB<sub>2</sub>/Metal compositions. The highest

strength material produced thus far is the  $\text{ZrB}_2\text{30Ti}$  composition. The average strength for this composition is  $10.2 \times 10^8 \text{ N/M}^2$  (150,000 psi). A comparison of the microstructures in Figures 3 through 5 for HP 141 ( $\text{ZrB}_2\text{20Ti}$ ), HP 172 A ( $\text{ZrB}_2\text{25Ti}$ ), and HP 172 B ( $\text{ZrB}_2\text{30Ti}$ ) shows the latter two to be more uniform in the distribution of the  $\text{ZrB}_2$ -type and the  $\text{TiB}$ -type phases and presumably the metal phase. The role of the acicular  $\text{TiB}$  phase with regard to strengthening is not known at this time. However, the acicular phase is definitely smaller than the  $\text{ZrB}_2$ -type phase.

The fracture strength for the  $\text{ZrB}_2\text{20Zr}$  compositions is somewhat less than the  $\text{ZrB}_2\text{20Ti}$  material. A comparison of the grain boundary phase for HP 126 versus HP 144 in Figures 21 and 22 shows a particularly uniform grain boundary phase distribution for HP 126 and poor mixing for HP 144. The mechanical test data obtained from HP 174 A is representative of a more uniformly mixed composition (Figure 23) of  $\text{ZrB}_2\text{20Zr}$  fabricated in the gas system. The observed strength is consistent with the microstructure. The fracture strength measured for the  $\text{ZrB}_2\text{50Zr}$  composition is in the range obtained for the  $\text{ZrB}_2\text{20Zr}$ . Again, the phase distribution is not particularly good for this composition and it is anticipated that a more uniform material would prove to have higher fracture strength. The 50 per cent Zr addition does not change the phases in equilibrium relative to  $\text{ZrB}_2\text{20Zr}$ ; the relative amounts of the phases do, of course, change.

The level of fracture strength obtained thus far for  $\text{ZrB}_2/\text{Ni}$  compositions is about that anticipated for polycrystalline ceramics of this grain size with no strengthening agent. The formed intermetallic grain boundary phase would not be considered as a strengthening agent. The ability of the Ni additive phase to wet the  $\text{ZrB}_2$  phase is particularly interesting and if the "in situ" reaction could be controlled to produce a  $\text{Ni}_3\text{B}_4$ -type bonding phase surrounded by unreacted Ni, then metallic strengthening would indeed be achieved. This was not, however, achieved.

#### IV. DISCUSSION OF RESULTS

The fabrication studies generated new and significant data on the role of metallic additives on the densification of  $\text{ZrB}_2$ . Experiments conducted with Ti, Zr, Fe, Ni and Cr as singular additives to  $\text{ZrB}_2$  revealed clearly distinguishable and different effects for each element. All elemental additions lower processing temperatures required to effect full densification. The Ni addition was the most efficient as evidenced by the 2200°F temperature required to densify  $\text{ZrB}_2\text{20Ni}$ ; however, the resulting product displayed poor mechanical properties.

Additions of Ti, Ni, Fe and Cr effect densification enhancement by reacting with the  $\text{ZrB}_2$  to form compounds for which exact identification presents considerable difficulty. The identification problems are lessened when the phase diagrams are known for the respective ternary systems. Addition of Zr to  $\text{ZrB}_2$  does not produce an intermediate phase in agreement with the binary phase diagram (11). In the Zr/ $\text{ZrB}_2$  system, enhanced densification and the resulting microstructures for  $\text{ZrB}_2\text{20Zr}$  and  $\text{ZrB}_2\text{50Zr}$ , are consistent with the formation of a liquid phase during processing from a metal-rich composition at or above the eutectic temperature. The addition of Ti produced an acicular type phase of extremely fine grain size; the relative amount of the acicular type phase increased with increasing Ti content. The addition of Ni produced a liquid phase at or near 2200°F with the formation of an inter-metallic phase of the  $\text{Ni}_3\text{B}_4$  type, but presumably a ternary phase. The formed phase wets the  $\text{ZrB}_2$  grain boundaries, producing a skeletal phase surrounding the  $\text{ZrB}_2$  matrix. Additions of Fe and Cr were the least effective in lowering the processing temperature. The reactions with  $\text{ZrB}_2$  were not fully delineated since the resulting materials did not show any substantial improvement in mechanical properties.

Based on the experience gained in previous attempts (1, 10) to fabricate reinforced diboride composites, the  $\text{ZrB}_2\text{20Ni}$  system was selected as a potential matrix phase of a modified diboride composition suitable for reinforcement studies. The low processing temperature found for the  $\text{ZrB}_2\text{20Ni}$  system was considered of particular importance since minimization of reinforcement-matrix chemical reaction and prevention of physical deterioration of the reinforcement were considered prerequisites for successful fabrication of truly reinforced diboride composites. The excessive chemical reactivity of the  $\text{ZrB}_2\text{20Ni}$  system, albeit the low processing temperature, produced undesirable reactions with nichrome and stainless steel wire reinforcements. This work was discontinued in favor of the polycrystalline  $\text{ZrB}_2/\text{Ti}$  system which appeared to offer some advantage in that rather high fracture strengths and improved

slow bend work of fracture values were obtained in early characterization tests.

Mechanical characterization tests were initially limited to impact tests using a 32.4 J (24 ft-lb) impacting energy and slow bend tests under conditions that produced catastrophic failure after fracture initiation. Both tests were conducted with V-notched specimens of the same dimensions and the work of fracture, W/A, calculated for the two tests differed considerably. For a series of ZrB<sub>2</sub>/Metal composites, W/A from these impact tests was of the order of 3500 J/M<sup>2</sup> (20 in-lbs/in<sup>2</sup>); W/A from the slow bend tests, 175 J/M<sup>2</sup> (1 in-lbs/in<sup>2</sup>). The variety of products produced from the ZrB<sub>2</sub>/Metal compositions and the ZrB<sub>2</sub>/SiC/C composites developed in earlier studies (1) were not distinguishable from the results of the impact tests; the results of the slow bend tests, however, did provide a material separation consistent with separately measured fracture strengths.

The significantly larger W/A values obtained from the impact tests relative to the values from the slow bend tests were investigated by examining the effect of lowering the impacting energy from 32.4 J (24 ft-lbs) to 1.35 J (1 ft-lb). The results provided in Tables 11 and 11 MKS show a dramatic decrease in measured impact energy with decreased impacting energy to 1.35 J (1 ft-lb) for a given material and a discernable differentiation among the ZrB<sub>2</sub> composites which was absent in the test results obtained using the 32.4 J (24 ft-lbs) impacting energy. The ZrB<sub>2</sub>50Zr composite was fabricated with a large excess of Zr metal in anticipation of producing a material of improved toughness although decreased thermal stability would be expected. The impact data obtained with the low impacting energy for this composite are thus consistent with the composition and the microstructure. The general lowering of the W/A values obtained at the lower impacting energies is consistent with the results cited earlier which were obtained by Multer (16), who showed a significant drop in measured impact energy for several ceramics including SiC when the tests were conducted to adjust the 2.70 J (2 ft-lbs) impacting energy used in ASTM-D256 such that "no tossing" of broken pieces resulted from the lower energy impact. For SiC Multer reported a drop from 0.30 J (0.22 ft-lb) to 0.054 J (0.04 ft-lb). An examination of the data in Tables 11 and 11 MKS shows that the program goal of producing a boride material of impact energy comparable to that displayed by WC6Co was indeed achieved with ZrB<sub>2</sub>50Zr. Insufficient specimen material of ZrB<sub>2</sub>30Ti was available for complete testing, however very limited data obtained with notched specimens in which the V-notch was replaced by saw kerfs of equal depth indicated that this material also has an impact energy comparable to that obtained for WC6Co. It is significant to note that this level of impact resistance was achieved for a polycrystalline boride material without introducing excess free metal in the final product and hence without a drastic reduction in thermal stability. The occurrence of a variation in mea-

sured impact energy (or work of fracture by impact) for different incident impacting energies bears further investigation, as ceramic materials are increasingly being considered for structural applications with a corresponding increase in necessity for design allowable data.

The method for measuring the work of fracture for brittle materials proposed by Tattersall and Tappin (5) was successfully applied to several of the boride composites examined in this program. Specimen configurations were found which permitted fracture to be initiated at very low loads and thus minimize the elastic energy stored in the specimen, and a suitably "hard" testing machine was employed to reduce the elastic energy stored in the test machine. Conditions for controlled fracture were not achieved for all materials tested. The very high strength of the WC6Co which results in excess elastic energy stored in the specimen was not offset by the known toughness of this material (which is a consequence of intergranular strengthening and fine grain size) and consequently fracture was catastrophic under all conditions of the tests employed. Catastrophic fracture also resulted for all conditions of tests for the weaker ZrB<sub>2</sub>/Metal composites. Controlled fracture was observed for diboride VIII(14,30)M<sub>2</sub>, which does not contain an intergranular strengthening agent, but which has a graphite phase with a morphology such that crack arrestment could be anticipated, Figure 36. Hardware components manufactured from VIII(14,30)M<sub>2</sub> in engineering development studies (8) for lifting reentry application showed crack arresting properties in agreement with the observations of controlled fracture in this program. Controlled fracture was observed for ZrB<sub>2</sub>30Ti which has somewhat different microstructural features than any of the other diboride/metal composites, Figure 5. The ZrB<sub>2</sub>20Ti and ZrB<sub>2</sub>25Ti composites have less of the acicular type phase which is believed to contribute to the improved toughness of this material. The increased Ti content in the powder mixture for ZrB<sub>2</sub>30Ti relative to composites with 25 and 20 weight per cent Ti could also result in more elemental Ti in the processed material tested. An increase in free titanium, or Ti/Zr alloy, could effect increased strength and toughness through intergranular bonding of the very fine Ti(Zr)B phase which, as indicated above, has the acicular morphology. The occurrence of controlled fracture for the ZrB<sub>2</sub>50Zr material is believed to be a consequence of the excess Zr metal in the fabricated material. The highest measured value of W/A was obtained for ZrB<sub>2</sub>30Ti, 278 J/M<sup>2</sup> (1.59 in-lbs/in<sup>2</sup>).

Fracture strength data was also obtained for the ZrB<sub>2</sub>/Metal composites. The results in Tables 17 and 17 MKS show that the highest strengths were obtained for the ZrB<sub>2</sub>/Ti composites; the strength increased with increases in Ti content in the starting powders which effected an increase in the fine grain acicular phase in the fabricated material. The highest strength, 10.2 N/M<sup>2</sup> (150,000 psi), was



obtained for  $\text{ZrB}_2\text{30Ti}$  which also was found to have significant toughness as shown by the occurrence of controlled fracture under suitable test conditions. Available impact data also indicate a measurably higher impact energy (work of fracture by impact) for  $\text{ZrB}_2\text{30Ti}$  relative to the other  $\text{ZrB}_2/\text{Metal}$  composites except  $\text{ZrB}_2\text{50Zr}$  which contains excess Zr metal. Fracture strengths for the  $\text{ZrB}_2/\text{Zr}$  and  $\text{ZrB}_2/\text{Ni}$  composites were consistent with microstructural characteristics. The addition and retention of elemental Zr provides a grain boundary strengthening. The reaction of Ni with  $\text{ZrB}_2$  produces an intermetallic grain boundary phase which does not provide any strengthening probably due to the brittleness of the formed phase.

The earlier reported (6) discrepancy in the  $W/A$  values obtained from impact tests conducted at high incident impacting energy and slow bend tests appears to be resolved by considering the results of the impact tests conducted at lower incident impacting energy. For the brittle ceramic materials an impacting energy of 1.35 J (1.00 ft-lbs) appears to be appropriate. The question of variation of impacting velocity was not considered in the tests conducted. Tattersall and Tappin (5) discuss variations of work of fracture measured in impact and by slow bend tests and report significantly larger values calculated from impact data for several metallic materials. Energy losses due to vibration and kinetic factors in the impact tests are cited. The question of variation of impacting energies was not discussed although other factors leading to energy absorption in impact tests were cited.

In order to compare the work of fracture measured for the boride composites with available data in the literature, it is convenient to designate the quantity, " $W/2A$ ," in agreement with the ceramic literature. For controlled fracture, the values of  $W/2A$  measured for  $\text{ZrB}_2\text{30Ti}$  and  $\text{ZrB}_2\text{50Zr}$  are of the same magnitude as reported for several ceramic materials. Tattersall and Tappin (5) report a work of controlled fracture for recrystallized alumina as 55 J/M<sup>2</sup> (0.31 in-lbs/in<sup>2</sup>);  $W/2A$  for  $\text{ZrB}_2\text{30Ti}$  is 138 J/M<sup>2</sup> (0.79 in-lbs/in<sup>2</sup>). A compilation of  $W/2A$  values obtained by several investigators and the results generated in this program are provided in Table 18. A comparison of the available characterization data for  $\text{ZrB}_2\text{30Ti}$  with the detailed information available for  $\text{Si}_3\text{N}_4$  reveals several common failures. In their discussion of the relationship between fracture energy and microstructure, Lange and Terwilliger (19) point out that the  $\text{Si}_3\text{N}_4$  material with the highest fracture energy was observed to have an elongated grain structure and rough surface features. The room temperature bend strength and the work of controlled fracture measured for  $\text{ZrB}_2\text{30Ti}$  are in excess of the corresponding values reported for  $\text{Si}_3\text{N}_4$ . Considerably

more data are of course available for  $\text{Si}_3\text{N}_4$ . The presence of the acicular phase in the  $\text{ZrB}_2\text{30Ti}$  is analogous to the elongated grain structure in  $\text{Si}_3\text{N}_4$ . The relative amount of the acicular phase increased with increasing Ti content from 20 to 30 weight per cent. Lange and Terwilliger (19) show that a change in grain morphology of  $\text{Si}_3\text{N}_4$  from an equi-axed structure to an elongated structure increased the fracture energy by a factor of four and the strength increased twofold, and they suggest that other ceramics may be similarly strengthened.

A consideration of the data and results obtained in the processing study coupled with the mechanical characterization information reveals that a new type of boride material is produced when  $\text{ZrB}_2/\text{Ti}$  compositions in the range 20 to 30 weight per cent Ti are hot pressed to full density. The materials fabricated from a 30 per cent Ti - 70 per cent  $\text{ZrB}_2$  starting powder mixture, which is designated  $\text{ZrB}_2\text{30Ti}$ , is characterized by a high fracture strength,  $10.2 \text{ N/M}^2$  (150,000 psi), and a degree of toughness demonstrated by controlled fracture with  $W/2A = 138 \text{ J/M}^2$  (0.79 in-lbs/in<sup>2</sup>). The highest strength diboride developed in the earlier study designed primarily to improve oxidation resistance and thermal stress resistance was  $6.4 \times 10^8 \text{ N/M}^2$  (94,000 psi) for VIII(18,10) (1). The diboride material VIII(14,30)M2 which was found to provide a measure of resistance to catastrophic crack propagation (8) was characterized in this study by a work of controlled fracture,  $W/2A$ , of  $88 \text{ J/M}^2$  (0.50 in-lbs/in<sup>2</sup>). The fine grained acicular structure in the  $\text{ZrB}_2/\text{Ti}$  composites, which increases with increasing Ti added to the  $\text{ZrB}_2$  starting material coupled with the retention of an alloyed metallic phase, is considered as a contributing factor in the observed behavior of the new type of boride material. This interpretation is consistent with the rationale developed by Lange and Terwilliger (19) in discussing the relationship of the elongated grain structure of hot pressed  $\text{Si}_3\text{N}_4$  of fracture strength,  $\sigma = 6.45 \times 10^8 \text{ N/M}^2$  (94,000 psi) and controlled fracture energy,  $W/2A = 70 \text{ J/M}^2$  (0.40 in-lbs/in<sup>2</sup>).

## REFERENCES

1. Clougherty, E. V., "Research and Development of Refractory Oxidation Resistant Diborides, Part II, Volume I: Summary," AFML-TR-68-190, Part II, Volume I, July 1970.
2. Kaufman, L. and Nesor, H., "Stability Characterization of Refractory Materials under High Velocity Atmospheric Flight Conditions, Part I; Volume I: Summary," AFML-TR-69-84, Part I, Volume I, March 1970.
3. Clougherty, E. V., "Research and Development of Refractory Oxidation Resistant Diborides, Part II, Volume VII: Application Evaluations and Design Considerations," AFML-TR-68-190, Part II, Volume VII, July 1970.
4. Kaufman, L., "Boride Composites--A New Generation of Nose Cap and Leading Edge Materials for Reusable Lifting Re-entry Systems," AIAA Paper No. 70-278, AIAA Advanced Space Transportation Meeting, Cocoa Beach, Florida, February 1970 (published in SAMPE Quarterly)(1970) 2 46.
5. Tattersall, H. G. and Tappin, G., "The Work of Fracture and Its Measurement in Metals, Ceramics and Other Materials," J. Materials Sci. 1 296-301 (1966).
6. Kaufman, L., Clougherty, E. V., and Nesor, H., "Investigation of Fracture Mechanics of Boride Composites," NASA Technical Report - Contract NASW 2088, July 1971.
- 7a. Kalish, D. and Kulin, S. A., "Thermomechanical Treatments Applied to Ultrahigh Strength Steels," Final Report - Contract No. 66-0142-C, Naval Air Systems Command, November 1966.
- 7b. Orner, G. M. and Hartbower, C. E., "Sheet Fracture Toughness Evaluated by Charpy Impact and Slow Bend," Welding Journal Research Supplement, September 1961.
8. Strauss, E. L., "Ceramic Nose Cap and Leading Edges for High Performance Weapon Systems," AFFDL-TR-72-19, April 1972.
9. Clougherty, E. V. and Peters, E. T., "Research and Development of Refractory Oxidation Resistant Diborides, Part II, Volume III: Thermochemical Stability Characteristics," AFML-TR-68-190, Part II, Volume III, January 1970.
10. Schulz, D. A. and Volk, H. F., "Transition Metal Diboride Matrix Composites," AFML-TR-71-41, April 1971.

11. E. Rudy, "Compendium of Phase Diagram Data," AFML-TR-65-2, Part V (1969).
12. Johnson, D. R. and Morgan, P. E. D., "Ceramic Matrix Composites as Armor Materials," AFML-TR-70-54, Part II, June 1971.
13. Duga, J. J., "Surface Energies of Ceramic Materials," DCIC Report 69-2, June 1969.
14. Rudnick, A., et. al., "The Evaluation and Interpretation of Mechanical Properties of Brittle Materials," DCIC Report 68-3, April 1968.
15. Davidge, R. W. and Tappin, G., "The Effective Surface Energy of Brittle Materials," J. Mat. Sci. 3 165-173 (1968).
16. Multer, R. K., "Impact Testing of Ceramics," Materials Research and Standards, 193-194 (1966).
17. Nakayama, J., "Direct Measurement of Fracture Energies of Brittle Homogeneous Materials," J. Am. Cer. Soc. 48 583-587 (1965).
18. Simpson, L. A., "The Effect of Microstructure on Fracture Energy Measurements in Alumina," Abstract, Fall Meeting American Ceramic Society (Pacific Coast), 1971.
19. Lange, F. F. and Terwilliger, G. R., "Fabrication and Properties of Silicon Compounds," Final Report, Naval Air Systems Command, Contract N00019-17-C-0107.

TABLE 1  
Processing Conditions for ZrB<sub>2</sub>/Ti Compositions

Composition*	Billet No.	Processing Conditions**				Density	
		Pressure (psi)	Temp. (°F)	Time (min)	Atmosphere	Billet (g/cc)	Powder (%)
12.5 Ti	HP 116	3000	2650	195	Air	5.05g/cc	88.6%
	HP 118	3000	2800	235	Air	5.61	98.4
20 Ti	HP 113	3000	2780	130	Air	5.73	100
	HP 124	3000	2780	135	Air	5.6	99
	HP 141	3000	2650	65	Air		
	HP 150 A, B	3000	2520	75	A	5.66 (A)	99+
25 Ti	HP 172 A	3000	2500 2500 2570 2570	40	A	5.57	
	HP 172 B	3000		40	A	5.50	

\*The composition designated is the weight percent of Ti powder mixed with ZrB<sub>2</sub> powder as the starting materials; the tabulated powder densities are calculated on the basis of the starting powder mixture.

\*\* Conditions tabulated are the time at the maximum temperature and pressure and the atmosphere used, A, or generated in the hot pressing apparatus, Air.

TABLE 2

Processing Conditions for ZrB<sub>2</sub>/Zr Compositions

Composition*	Billet No.	Processing Conditions**			Density	
		Pressure (psi)	Temp. (°F)	Time (min)	Atmosphere	Billet (g/cc) Powder (%)
20 Zr	HP 126	3000	3035°F	87 min	Air	99%
	HP 139	3000	2970	145	Air	99
	HP 144	3000	2670	40	A	6.19 100
	HP 174A, B	3000	2730 to 2812	17	A	6.13 A 6.07 B
50 Zr	HP 152 A, B	3000	2200-	120	A	6.24A 100
			2260	85	A	6.24B 100

TABLE 3

Processing Conditions for ZrB<sub>2</sub>/Ni Compositions

25 Ni	HP 153 A, B	3000	2350	160	A	
20 Ni	HP 173 A, B	3000	2200		A	6.28 A 6.21 B

\*The composition designated is the weight percent of additive mixed with ZrB<sub>2</sub> powder as the starting materials; the tabulated powder densities are calculated on the basis of the starting powder mixture.

\*\*Conditions tabulated are the time at the maximum temperature and pressure and the atmosphere used, A, or generated in the hot pressing apparatus, Air.

TABLE 4

Processing Conditions for  $\text{ZrB}_2$ /Metal Matrix-Wire Mesh Composites

(3 in. Diameter by 0.5 in Height)

Compositions*	Billet No.	Processing Conditions**			Remarks
<u>Matrix</u>		<u>Press</u>	<u>Temp.</u>	<u>Time</u>	
Reinforcement		psi	°F	min	
$\text{ZrB}_2$ 20Ni	HP 127	3000	2420	100	Microstructure dense except for holes
Nichrome	HP 131	3000	2200	215	ditto
	HP 134	3000	1950	115**	Tooling Failed in Heating cycle
$\text{ZrB}_2$ 20Ni	HP 138	3000	1600-2190	165	Same as 127, 134
Stainless					

\*The additive phase is given in weight percent in the starting powder material; the powder lot for the additive phase is identified by the parentheses.

\*\*Conditions cited are the time at the maximum temperature and pressure except HP 134 which is total time of run curtailed due mechanical failure of punch during heating cycle.

TABLE 5

Processing Conditions for  $\text{ZrB}_2/\text{Fe}$  Compositions

Composition*	Billet No.	Processing Conditions**			Density	Pwd. Density
		<u>Press</u>	<u>Temp.</u>	<u>Time</u>		
		psi	$^{\circ}\text{F}$	min	g/cc	(%)
$\text{ZrB}_2$ 10Fe (01)	HP98	3000	2800	115	5.84	(97)
		3000	2900	120		
$\text{ZrB}_2$ 10Fe (01)	HP101	3000	2900	240	6.03	(100*)
$\text{ZrB}_2$ 20Fe (01)	HP106	3000	2820	150	6.31	(99+)
$\text{ZrB}_2$ 30Fe (01)	HP107	3000	2515	165	6.34	(98)

\*The additive phase is given in weight percent in the starting powder material;  
the powder lot for the additive phase is identified by the parentheses.

\*\* Conditions cited are the time at the maximum temperature and pressure



TABLE 6  
IMPACT TEST DATA FOR UNDERSIZED SPECIMENS  
(24 ft-lb Incident Impact Energy)

<u>Composition</u>	<u>h</u>	<u>t</u>	<u>Impact Energy, W/A</u>	
Billet	inch.	inch	ft-lbs	in-lbs/in <sup>2</sup>
<u>WC6Co</u>				
15C	0.317	0.200	0.310	58.8
16C	0.316	0.199	0.306	58.4
17C	0.316	0.200	0.262	49.8
18C	0.314	0.199	0.282	54.1
19C	0.316	0.200	0.343	65.2
20C	0.317	0.200	0.310	58.8
			Average	57.5
Ave. Ref. (6)	0.315	0.395		73.9
<u>Boride V</u>				
31L-11C	0.316	0.200	0.116	22.0
31L-12C	0.316	0.200	0.132	25.0
31L-13C	0.315	0.200	0.148	28.2
31L-14C	0.316	0.200	0.128	24.3
31L-15C	0.316	0.200	0.106	20.1
31L-16C	0.314	0.200	0.101	19.3
			Average	23.2
Ave. Ref. (6)	0.315	0.394		22.3
<u>Boride VIII-M2</u>				
NP2-17C	0.317	0.200	0.089	16.9
NP2-18C	0.316	0.200	0.088	16.8
NP2-19C	0.314	0.199	0.096	18.5
NP2-20C	0.316	0.199	0.095	18.2
NP2-21C	0.316	0.199	0.096	18.3
NP2-22C	0.319	0.199	0.096	18.1
			Average	17.8
Ave. Ref. (6)	0.315	0.394		17.3

TABLE 6MKS  
IMPACT TEST DATA FOR UNDERSIZED SPECIMENS  
(32.4 J Incident Impact Energy)

<u>Composition</u> Billet	<u>h</u>	<u>t</u>	<u>Impact Energy, W/A</u>	
	$10^{-3}\text{M}$	$10^{-3}\text{M}$	J	J/M <sup>2</sup>
<u>WC6Co</u>				
15C	8.05	5.08	0.420	10,290
16C	8.03	5.05	0.415	10,220
17C	8.03	5.08	0.355	8,715
18C	7.98	5.05	0.382	9,468
19C	8.03	5.08	0.465	11,410
20C	8.05	5.08	0.420	10,240
			Average	10,600
Ave. Ref. (6)	8.00	10.03		12,920
<u>Boride V</u>				
31L-11C	8.03	5.08	0.157	3,850
31L-12C	8.03	5.08	0.179	4,375
31L-13C	8.00	5.08	0.200	4,935
31L-14C	8.03	5.08	0.174	4,255
31L-15C	8.03	5.08	0.144	3,520
31L-16C	7.98	5.08	0.137	3,378
			Average	4,060
Ave. Ref. (6)	8.00	10.00		4,252
<u>Boride VIII-M2</u>				
NP2-17C	8.05	5.08	0.121	2,960
NP2-18C	8.03	5.08	0.119	2,940
HP2-19C	7.98	5.05	0.130	3,240
NP2-20C	8.03	5.05	0.129	3,190
NP2-21C	8.03	5.05	0.130	3,200
NP2-22C	8.10	5.05	0.130	3,170
			Average	3,120
Ave. Ref. (6)	8.00	10.00		3,030

TABLE 7  
IMPACT TEST DATA FOR  $\text{ZrB}_2$  - METAL COMPOSITES  
(24 ft-lb Incident Impact Energy)

<u>Composition</u> Billet	<u>h</u>	<u>t</u>	<u>Impact Energy, W/A</u>	
	inch	inch	ft-lbs	in-lbs/in <sup>2</sup>
<u><math>\text{ZrB}_2</math>20Fe</u>				
HP106-1C	0.311	0.395	0.232	22.7
HP106-2C	0.308	0.395	0.241	23.8
HP106-3C	0.311	0.395	0.364*	35.6
HP106-4C	0.310	0.395	0.278	27.3
<u><math>\text{ZrB}_2</math>30Fe</u>				
HP107-1C	0.306	0.390	0.238	23.9
HP107-2C	0.306	0.390	0.210	21.1
HP107-3C	0.306	0.390	0.200	20.2
<u><math>\text{ZrB}_2</math>10Fe (6)</u>				
HP101-1C	0.321	0.391	0.230	22.0
HP101-2C	0.318	0.392	0.232	22.4
HP101-3C	0.319	0.391	0.253	24.3

Note: In the impact testing sequence, the following irregularities were noted for the specimens marked with the asterisks:

\* One-half of fractured specimen traveled forward in direction of pendulum.

TABLE 7MKS  
IMPACT TEST DATA FOR  $\text{ZrB}_2$  - METAL COMPOSITES  
(32.4 J Incident Impact Energy)

<u>Composition</u>	<u>h</u>	<u>t</u>	<u>Impact Energy, W/A</u>	
Billet	$10^{-3}\text{M}$	$10^{-3}\text{M}$	J	$\text{J/M}^2$
<u><math>\text{ZrB}_2\text{20Fe}</math></u>				
HP106-1C	7.90	10.03	0.315	3,972
HP106-2C	7.82	10.03	0.327	4,165
HP106-3C	7.90	10.03	0.494*	6,230
HP106-4C	7.87	10.03	0.377	4,777
<u><math>\text{ZrB}_2\text{30Fe}</math></u>				
HP107-1C	7.77	9.91	0.323	4,183
HP107-2C	7.77	9.91	0.285	3,692
HP107-3C	7.77	9.91	0.271	3,535
<u><math>\text{ZrB}_2\text{10Fe (6)}</math></u>				
HP101-1C	8.15	9.93	0.312	3,850
HP101-2C	8.08	9.96	0.315	3,920
HP101-3C	8.10	9.93	0.314	4,260

Note: In the impact testing sequence, the following irregularities were noted for the specimens marked with the asterisks:

\* One-half of fractured specimen traveled forward in direction of pendulum.

TABLE 8  
IMPACT TEST DATA FOR ZrB<sub>2</sub> METAL COMPOSITES  
(24 ft-lb Incident Impact Energy)

<u>Composition</u> *	<u>Specimen Geometry at Notch</u>		<u>Impact Energy, W/A</u>	
	<u>Height</u>	<u>Thickness</u>	<u>Measured</u>	<u>Normalized</u>
	(inch)	(inch)	(ft.-lbs.)	(in.lbs./in. <sup>2</sup> )
ZrB <sub>2</sub> 50Zr	0.313	0.395	0.265	25.8
HP 152 B(Gas)	0.313	0.395	0.276	26.9
	0.313	0.395	0.383	37.3
Average			0.308	30.0
ZrB <sub>2</sub> 20Ti	0.314	0.395	0.171	16.5
HP 150 B(Gas)	0.314	0.395	0.163	15.8
Average			0.167	16.1
ZrB <sub>2</sub> 20Ti	0.317	0.396	0.175**	16.7
HP 113 (Air)	0.309	0.395	0.202***	19.9
	0.314	0.395	0.204	19.7
	0.312	0.395	0.202	19.7
Average				19.0

Note: In the impact testing sequence, the following irregularities were noted for the specimens marked with the asterisks:

\* Processing atmosphere given in parentheses, see Section II.

\*\*Both halves of fractured specimen traveled in reverse direction to pendulum swing.

\*\*\*A large chip broke off from the face of one of the fractured pieces.

TABLE 8 MKS  
IMPACT TEST DATA FOR ZrB<sub>2</sub> METAL COMPOSITES  
(32.4 J Incident Impact Energy)

<u>Composition*</u>	<u>Specimen Geometry at Notch</u>		<u>Impact Energy, W/A</u>	
	<u>Height</u> (M x 10 <sup>-3</sup> )	<u>Thickness</u> (M x 10 <sup>-3</sup> )	<u>Measured</u> (J)	<u>Normalized</u> (J/M <sup>2</sup> )
ZrB <sub>2</sub> 50Zr	7.95	10.03	0.359	4,510
HP 152 B(Gas)	7.95	10.03	0.375	4,705
	7.95	10.03	0.520	6,525
Average			0.418	5,250
ZrB <sub>2</sub> 20Ti	7.98	10.03	0.232	2,885
HP 150 B(Gas)	7.98	10.03	0.221	2,765
Average			0.227	2,815
ZrB <sub>2</sub> 20Ti	8.05	10.06	0.237**	2,922
HP 113 (Air)	7.84	10.03	0.274***	3,483
	7.98	10.03	0.277	3,448
	7.92	10.03	0.274	3,448
Average				

Note: In the impact testing sequence, the following irregularities were noted for the specimens marked with the asterisks:

\* Processing atmosphere given in parentheses, see Section II.

\*\* Both halves of fractured specimen traveled in reverse direction to pendulum swing.

\*\*\* A large chip broke off from the face of one of the fractured pieces.

TABLE 9

IMPACT TEST DATA FOR  $\text{ZrB}_2$  COMPOSITION: VIII(18,10)  
(24 ft-lb Incident Impact Energy)

$\frac{h}{\text{inch}}$	$\frac{t}{\text{inch}}$	$\frac{\text{Impact Energy, W/A}}{\text{ft-lbs} \quad \text{in-lbs/in}^2}$	
		ft-lbs	in-lbs/in <sup>2</sup>
0.314	0.395	0.210	20.3
0.316	0.395	0.208	20.0
0.314	0.395	0.289	28.0
0.314	0.395	0.206	20.0

TABLE 9 MKS

IMPACT TEST DATA FOR  $\text{ZrB}_2$  COMPOSITION: VIII(18,10)  
(32.4 J Incident Impact Energy)

$\frac{h}{10^{-3}\text{M}}$	$\frac{t}{10^{-3}\text{M}}$	$\frac{\text{Impact Energy, W/A}}{\text{J} \quad \text{J/M}^2}$	
		J	J/M <sup>2</sup>
7.98	10.03	0.285	3,553
8.03	10.03	0.282	3,500
7.98	10.03	0.392	4,900
7.98	10.03	0.279	3,500

TABLE 10  
IMPACT TEST DATA FOR  $\text{ZrB}_2$  METAL COMPOSITES  
(24 ft-lb Incident Impact Energy)

<u>Composition*</u>	<u>Specimen Geometry at Notch</u>		<u>Impact Energy, W/A</u>	
	<u>Height</u> (inch)	<u>Thickness</u> (inch)	<u>Measured</u> (ft-lbs)	<u>Normalized</u> (in-lbs/in <sup>2</sup> )
$\text{ZrB}_2/\text{Ni:Nichrome}$				
HP 127-1	0.314	0.395	0.157	15.1
HP 127-2	0.314	0.394	0.148	14.2
HP 131-1	0.314	0.395	0.167	16.0
$\text{ZrB}_2/\text{Ni:Stainless}$				
HP 138-1	0.314	0.394	0.218	20.9
HP 138-2	0.314	0.395	0.214	20.5
HP 138-3	0.314	0.394	0.189	18.1

\* See Table 4 and Text in Section II for billet processing and composition data.



TABLE 10 MKS  
IMPACT TEST DATA FOR  $\text{ZrB}_2$  METAL COMPOSITES  
(32.4 J Incident Impact Energy)

<u>Composition</u> *	<u>Specimen Geometry at Notch</u>		<u>Impact Energy, W/A</u>	
	<u>Height</u> (M x $10^{-3}$ )	<u>Thickness</u> (M x $10^{-3}$ )	<u>Measured</u> (J)	<u>Normalized</u> (J/M <sup>2</sup> )
$\text{ZrB}_2/\text{Ni:Nichrome}$				
HP 127-1	7.98	10.03	0.212	2,640
HP 127-2	7.98	10.00	0.200	2,480
HP 131-1	7.98	10.03	0.226	2,800
$\text{ZrB}_2/\text{Ni:Stainless}$				
HP 138-1	7.98	10.00	0.295	3,680
HP 138-2	7.98	10.03	0.289	3,590
HP 138-3	7.98	10.00	0.255	3,160

\* See Table 4 and Text in Section II for billet processing and composition data.

TABLE 11

## IMPACT TEST RESULTS FOR VARIATION OF INCIDENT IMPACTING ENERGY

(Specimen: V-Notch, 0.080 in. deep,  
0.394 in. x 0.394 in. cross section)

<u>Material</u>	<u>Incident Energy</u> (ft-lbs)	<u>Impact Energy</u>	
		<u>Measured</u> (ft-lbs)	<u>Normalized, W/A</u> (in-lbs/in <sup>2</sup> )
WC6Co	24.0	0.76	74
	0.98	0.08	7.7
VIII(18,10)	24.0	0.21	20
	2.0	0.10	9.6
	1.1	0.05	4.8
VIII(14,30)M2	24.0	0.18	17
	1.0	0.03	3.0
	1.0	0.01	1.0
ZrB <sub>2</sub> 20Zr	24.0	0.26	27
	0.98	0.02	1.9
ZrB <sub>2</sub> 50Zr	24.0	0.31	30
	0.97	0.10	9.6
	0.97	0.09	8.6

TABLE 11 MKS

## IMPACT TEST RESULTS FOR VARIATIONS OF INCIDENT IMPACTING ENERGY

(Specimens: V-Notch, 0.20 cm deep  
in 1 cm x 1 cm cross section)

<u>Material</u>	<u>Incident Energy</u> (J)	<u>Impact Energy</u>	
		<u>Measured</u> (J)	<u>Normalized, W/A</u> (J/M <sup>2</sup> )
WC6Co	32.4	1.03	12,950
	1.3	0.11	1,348
VIII(18,10)	32.4	0.28	3,500
	2.7	0.14	1,680
	1.5	0.07	840
VIII(14,30)M2	32.4	0.24	2,980
	1.35	0.04	575
	1.35	0.014	175
ZrB <sub>2</sub> 20Zr	32.4	0.35	4,730
	1.3	0.026	323
ZrB <sub>2</sub> 50Zr	32.4	0.42	5,250
	1.3	0.135	1,680
	1.3	0.12	1,500

TABLE 12

"SOFT" SLOW BEND TEST DATA FOR  $\text{ZrB}_2/\text{Fe}$  AND  $\text{ZrB}_2/\text{Cr}$  COMPOSITES  
( $l$ =span length=1.75 in.)

Composition	h	t	$P_{\max}$	W	Work of Fracture, W/A
Specimen No.	inch	inch	lbs.	in-lbs	in-lbs/in <sup>2</sup>
$\text{ZrB}_210\text{Fe}^*$					
HP98-4S	0.313	0.394	126	0.0451	0.368
HP98-5S	0.317	0.395	128	0.0512	0.409
HP101-4S	0.315	0.392	124	0.0645	0.523
HP101-5S	0.314	0.390	133	0.0532	0.434
HP101-6S	0.318	0.391	147	0.0588	0.473
$\text{ZrB}_220\text{Fe}$					
HP106-6S	0.316	0.395	267	0.1121	0.899
HP106-7S	0.318	0.395	232	0.1044	0.848
$\text{ZrB}_230\text{Fe}$					
HP107-4S	0.311	0.391	177	0.1009	0.830
HP107-5S	0.305	0.391	182	0.0892	0.748
HP107-6S	0.305	0.390	166	0.0797	0.670
$\text{ZrB}_210\text{Cr}$					
HP99-1	0.314	0.393	120	0.055	0.44
HP99-2	0.314	0.394	95	0.048	0.39
HP99-3	0.310	0.394	117	0.047	0.39
$\text{ZrB}_210\text{Cr}$					
HP103-1	0.316	0.394	122	0.040	0.32
HP103-2	0.316	0.394	120	0.042	0.34
HP103-3	0.316	0.394	121	0.033	0.27

TABLE 12 MKS

"SOFT" SLOW BEND TEST DATA FOR  $\text{ZrB}_2/\text{Fe}$  AND  $\text{ZrB}_2/\text{Cr}$  COMPOSITES  
( $l=\text{span length}=0.0444\text{M}$ )

Composition	h	t	$P_{\max}$	W	Work of Fracture, W/A
Specimen No.	$10^{-3}\text{M}$	$10^{-3}\text{M}$	N	$10^{-3}\text{J}$	$\text{J}/\text{M}^2$
$\text{ZrB}_2/10\text{Fe}^*$					
HP98-4S	7.95	10.00	560	5.10	64.4
HP98-5S	8.05	10.03	570	5.79	71.6
HP101-4S	8.00	9.96	552	7.29	91.5
HP101-5S	7.98	9.91	592	6.01	76.0
HP101-6S	8.08	9.93	654	6.64	82.8
$\text{ZrB}_2/20\text{Fe}$					
HP106-6S	8.03	10.03	1188	12.67	157
HP106-7S	8.08	10.03	1032	11.80	148
$\text{ZrB}_2/30\text{Fe}$					
HP107-4S	7.90	9.93	788	11.40	145
HP107-5S	7.75	9.93	810	10.08	134
HP107-6S	7.75	9.91	739	9.01	117
$\text{ZrB}_2/10\text{Cr}$					
HP99-1	7.98	9.98	533	6.2	77
HP99-2	7.98	10.00	422	5.4	68
HP99-3	7.87	9.98	519	5.3	68
$\text{ZrB}_2/10\text{Cr}$					
HP103-1	8.03	9.98	542	4.5	56
HP103-2	8.03	9.98	532	4.7	60
HP103-3	8.03	9.98	537	3.7	47

TABLE 13

"SOFT" SLOW BEND TEST DATA FOR DIBORIDE VIII(18,10)  
 AND  $\text{ZrB}_2$  METAL COMPOSITES  
 (l=span length=1.57 in.)

Composition	h	t	P <sub>max</sub>	W	Work of Fracture, W/A
Specimen No.	inch	inch	lbs.	in-lbs	in-lbs/in <sup>2</sup>
VIII(18,10)					
R33L-A	0.310	0.394	233	0.116	0.95
R33L-B	0.310	0.394	211	0.095	0.78
R33L-C	0.315	0.393	226	0.100	0.81
R33L-D	0.305	0.394	225	0.116	0.97
$\text{ZrB}_2\text{20Zr}$					
HP126-4	0.314	0.392	270	0.153	1.24
HP126-3	0.320	0.392	264	0.136	1.08
$\text{ZrB}_2\text{12.5Ti}$					
HP118-1	0.331	0.399	287	0.161	1.22
HP118-4	0.331	0.399	310	0.156	1.18
$\text{ZrB}_2\text{20Ti}$					
HP113-5S	0.305	0.395	184	0.0754	0.627
HP113-7S	0.312	0.395	274	0.1589	1.288
HP113-8S	0.310	0.396	253	0.2328	1.895
$\text{ZrB}_2\text{20Ti}$					
HP124-1	0.318	0.395	376	0.265	2.10
HP124-2	0.318	0.396	349	0.227	1.80
HP124-3	0.316	0.395	277	0.160	1.27

TABLE 13 MKS

"SOFT" SLOW BEND TEST DATA FOR DIBORIDE VIII(18,10)  
 AND  $\text{ZrB}_2$  METAL COMPOSITES  
 (l=span length=0.0398 M)

Composition	h	t	$P_{\max}$	W	Work of Fracture, W/A
Specimen No.	$10^{-3}\text{M}$	$10^{-3}\text{M}$	N	$10^{-3}\text{J}$	$\text{J/M}^2$
VIII(18,10)					
R33L-A	7.87	10.00	990	13.1	166
R33L-B	7.87	10.00	937	10.7	137
R33L-C	8.00	9.98	1003	11.3	142
R33L-D	7.75	10.00	999	13.1	170
$\text{ZrB}_2\text{20Zr}$					
HP126-4	7.98	9.96	1199	17.3	217
HP126-3	8.03	9.96	1172	15.4	189
$\text{ZrB}_2\text{12.5Ti}$					
HP118-1	8.31	10.13	1274	18.2	213
HP118-4	8.31	10.13	1376	17.6	207
$\text{ZrB}_2\text{20Ti}$					
HP113-5S	7.75	10.03	819	9.25	110
HP113-7S	7.92	10.03	1219	13.77	225
HP113-8S	7.87	10.06	1126	12.72	332
$\text{ZrB}_2\text{20Ti}$					
HP124-1	8.08	10.03	1669	29.9	368
HP124-2	8.08	10.06	1550	25.6	315
HP124-3	8.03	10.06	1230	18.0	222

TABLE 14

"HARD" SLOW BEND TEST DATA AND RESULTS FOR V-NOTCH SPECIMENS\*

<u>Material</u>	<u>Work of Catastrophic Fracture</u>	
	Measured in-lbs	Normalized, W/A in-lbs/in <sup>2</sup>
Boride SiC Composites:		
VIII(18,10)R33L	0.168	1.4
VIII(14,30)M2, NP7	0.30	2.4
Tungsten Carbide:		
WC6Co	1.0	4.0
Boride Metal Composites:		
ZrB <sub>2</sub> 20Zr, HP 139	0.34	2.7
ZrB <sub>2</sub> 20Ti, HP 124	0.61	4.9
ZrB <sub>2</sub> 10Cr, HP 103	0.164	1.3
ZrB <sub>2</sub> 30Fe, HP 107	0.31	2.5
ZrB <sub>2</sub> 20Ni:Nichrome, HP 127	0.38	3.0
ZrB <sub>2</sub> 20Ni:Nichrome, HP 131	0.314	2.5
ZrB <sub>2</sub> 50Zr, HP 152	(1.41)	(11.3)

\* Specimens were 0.394 in x 0.394 in x 2.165 in long with V-notch 0.080 in deep and 0.001 in radius specified for notch of 45°. Specimen results tabulated in parentheses were obtained with 90° notch.



TABLE 14 MKS

"HARD" SLOW BEND TEST DATA AND RESULTS FOR V-NOTCH SPECIMENS\*

<u>Material</u>	<u>Work of Catastrophic Fracture</u>	
	Measured (J)	Normalized, W/A (J/M <sup>2</sup> )
Boride SiC Composites:		
VIII(18,10)R33L	0.0189	245
VIII(14,30)M2, NP7	0.033	420
Tungsten Carbide:		
WC6Co	0.112	700
Boride Metal Composites:		
ZrB <sub>2</sub> 20Zr, HP 139	0.038	473
ZrB <sub>2</sub> 20Ti, HP 124	0.069	859
ZrB <sub>2</sub> 10Cr, HP 103	0.0184	228
ZrB <sub>2</sub> 30Fe, HP 107	0.035	438
ZrB <sub>2</sub> 20Ni:Nichrome, HP 127	0.043	525
ZrB <sub>2</sub> 20Ni:Nichrome, HP 131	0.035	438
ZrB <sub>2</sub> 50Zr, HP 152	(0.159)	(1980)

\* Specimens were 0.394 in. x 0.394 in. x 2.165 in. long with V-notch 0.080 in. deep and 0.001 in. radius specified for notch of 45°. Specimen results tabulated in parentheses were obtained with 90° notch.

TABLE 15  
COMPARISON OF RESULTS FOR "SOFT" AND "HARD" SLOW BEND TESTS  
FOR V-NOTCH SPECIMENS\*

<u>Material</u>	<u>Normalized Work of Catastrophic Fracture, W/A</u>	
	"Soft" Test	"Hard" Test
	$\frac{\text{in-lbs}}{\text{in}^2}$	$\frac{\text{in-lbs}}{\text{in}^2}$
WC6Co	2.6	4.0
VIII(18,10)	0.88	1.4
VIII(14,30)M2	1.30	2.4
ZrB <sub>2</sub> 20Zr	1.16	2.7
ZrB <sub>2</sub> 20Ti	1.27 to 2.10	4.9
ZrB <sub>2</sub> 10Cr	0.31	1.3
ZrB <sub>2</sub> 30Fe	0.75	2.5

\* Specimens were 0.394 in. x 0.394 in. x 2.165 in. long with V-notch 0.080 in. deep and 0.001 in. radius specified for notch of 45°.

TABLE 15 MKS  
COMPARISON OF RESULTS FOR "SOFT" AND "HARD" SLOW BEND TESTS  
FOR V-NOTCH SPECIMENS\*

<u>Material</u>	<u>Normalized Work of Catastrophic Fracture, W/A</u>	
	"Soft" Test J/M <sup>2</sup>	"Hard" Test J/M <sup>2</sup>
WC6Co	455	700
VIII(18,10)	154	245
VIII(14,30)M2	228	420
ZrB <sub>2</sub> 20Zr	203	473
ZrB <sub>2</sub> 20Ti	223 to 368	859
ZrB <sub>2</sub> 10Cr	54	228
ZrB <sub>2</sub> 30Fe	131	438

\*Specimens were 0.394 in. x 0.394 in. x 2.165 in. long with V-notch 0.080 in. deep and 0.001 in. radius specified for notch of 45°.

TABLE 16  
"HARD" SLOW BEND TEST DATA AND RESULTS  
FOR CHEVRON NOTCHED\* SPECIMENS

<u>Material</u>	<u>Configuration</u>	<u>Fracture Type**</u>	<u>Work of Fracture</u>	
			Measured (in-lbs)	Normalized, W/A (in-lbs/in <sup>2</sup> )
WC6Co Diboride VIII(14,30)M2:	B	Catastrophic	0.11	2.75
NP7A	A	Catastrophic	0.22	1.74
NP7B	A	Catastrophic	0.22	1.74
NP7-1	B	Controlled	0.0405	1.02
NP7-2	B	Controlled	0.0385	0.96
NP7C	B	Semi-Controlled	(0.059)	(1.46) Note 1
NP7D	B	Semi-Controlled	(0.055)	(1.38) Note 1
ZrB <sub>2</sub> /Metal Composites:				
ZrB <sub>2</sub> 30Ti				
HP 172 B-1	B	Controlled	0.0675	1.68
HP 172 B-2	B	Controlled	0.060	1.50
ZrB <sub>2</sub> 25Ti				
HP 172 A-1	B	Catastrophic	0.066	1.66
HP 172 A-2	B	Catastrophic	0.075	1.88
ZrB <sub>2</sub> 20Ti				
HP 124	B	Catastrophic	0.030	0.75
ZrB <sub>2</sub> 20Zr				
HP 174 A-1	B	Semi-Controlled	0.036	0.90
HP 174 A-2	B	Catastrophic	(0.071)	(1.80) Note 1
ZrB <sub>2</sub> 50Zr				
HP 152 B	B	Controlled	0.237	5.92
ZrB <sub>2</sub> 20Ni				
HP 173 A-1	B	Semi-Controlled	0.0023	0.056
HP 173 A-2	B	Semi-Controlled	0.0015	0.036

\*See Figure 41 for details of chevron notch configurations.

\*\*See Figure 42 for graphical representations of fracture types.

Note 1. Data and results tabulated in parentheses were obtained with constant stress rate apparatus using a more sensitive load cell which reduces the "hardness" of the machine.

TABLE 19

GLASS, SLOW BEND TEST DATA AND RESULTS  
FOR CHELON NOTCHED SPECIMENS

Specimen	Notch	Length of Specimen, in.	Length of Notch, in.	Modulus of Elasticity, $\times 10^6$ psi	Modulus of Elasticity, $\times 10^6$ psi	Modulus of Elasticity, $\times 10^6$ psi	Modulus of Elasticity, $\times 10^6$ psi	Modulus of Elasticity, $\times 10^6$ psi	Modulus of Elasticity, $\times 10^6$ psi
NP7A	A	0.125	0.005	0.125	0.125	0.125	0.125	0.125	0.125
NP7-B	B	0.125	0.005	0.125	0.125	0.125	0.125	0.125	0.125

TABLE 16 MKS  
"HARD" SLOW BEND TEST DATA AND RESULTS  
FOR CHEVRON NOTCHED\* SPECIMENS

<u>Material</u>	<u>Configuration</u>	<u>Fracture Type**</u>	<u>Work of Fracture</u>	
			Measured (J)	Normalized, W/A (J/M <sup>2</sup> )
WC6Co	B	Catastrophic	0.012	480
Diboride VIII(14,30)M2:				
NP7A	A	Catastrophic	0.025	306
NP7B	A	Catastrophic	0.025	306
NP7-1	B	Controlled	0.0045	178
NP7-2	B	Controlled	0.0043	168
NP7C	B	Semi-Controlled	(0.0065)	(255) Note 1
NP7D	B	Semi-Controlled	(0.0062)	(242) Note 1
ZrB <sub>2</sub> /Metal Composites:				
ZrB <sub>2</sub> 30Ti				
HP 172 B-1	B	Controlled	0.0675	294
HP 172 B-2	B	Controlled	0.060	262
ZrB <sub>2</sub> 25Ti				
HP 172 A-1	B	Catastrophic	0.0076	290
HP 172 A-2	B	Catastrophic	0.0084	329
ZrB <sub>2</sub> 20Ti				
HP 124	B	Catastrophic	0.0034	132
ZrB <sub>2</sub> 20Zr				
HP 174 A-1	B	Semi-Controlled	0.00405	158
HP 174 A-2	B	Catastrophic	(0.0080)	(315) Note 1
ZrB <sub>2</sub> 50Zr				
HP 152 B	B	Controlled	0.027	1035
ZrB <sub>2</sub> 20Ni				
HP 173 A-1	B	Semi-Controlled	0.00026	10
HP 173 A-2	B	Semi-Controlled	0.00017	6

\* See Figure 41 for details of chevron notch configurations.

\*\* See Figure 42 for graphical representations of fracture types.

Note 1. Data and results in parentheses were obtained with constant stress rate apparatus using a more sensitive load cell which reduces the "hardness" of the machine.



TABLE 17  
FRACTURE STRENGTH LEVELS FOR  $\text{ZrB}_2$  METAL COMPOSITES  
(Four Point Bending)

<u>Composition</u>			<u>Fracture Strength, <math>10^3</math> psi</u>		
$\text{ZrB}_2$ 12.5Ti	HP 118	(Air)	76.0, 78.0		Av. 77.0
$\text{ZrB}_2$ 20Ti	HP 124	(Air)	88.0, 106		Av. 97.0
$\text{ZrB}_2$ 20Ti	HP 141	(Air)	89.1, 85.4, 86.5		Av. 87.0
$\text{ZrB}_2$ 20Ti	HP 150 A	(Gas)	97.7, 99.5, 96.4		Av. 97.8
$\text{ZrB}_2$ 25Ti	HP 172 A	(Gas)	96.1, 129.0		Av. 112.5
$\text{ZrB}_2$ 30Ti	HP 172 B	(Gas)	146.0, 155.0		Av. 150.5
$\text{ZrB}_2$ 20Zr	HP 126	(Air)	72.2, 82.0		Av. 76.0
$\text{ZrB}_2$ 20Zr	HP 139	(Air)	76.4, 78.6		Av. 77.5
$\text{ZrB}_2$ 20Zr	HP 144*	(Gas)	34.9, 37.1, 36.4		Av. 36.1
$\text{ZrB}_2$ 20Zr	HP 174 A	(Gas)	72.5, 84.1		Av. 78.3
$\text{ZrB}_2$ 50Zr	HP 152	(Gas)	80.0, 81.6, 76.5		Av. 79.3
$\text{ZrB}_2$ 20Ni	HP 153 B	(Gas)	45.9, 47.5, 42.3		Av. 45.2
$\text{ZrB}_2$ 20Ni	HP 173 A	(Gas)	43.9, 50.7		Av. 47.3

\*Metallography revealed poor mixing to be consistent with low strength.



TABLE 17 MKS  
FRACTURE STRENGTH LEVELS FOR  $ZrB_2$  METAL COMPOSITES  
(Four Point Bending)

<u>Composition</u>			<u>Fracture Strength, <math>10^8 \text{ N/M}^2</math></u>		
$ZrB_2$ 12.5Ti	HP 118	(Air)	5.17, 5.30	Av.	5.23
$ZrB_2$ 20Ti	HP 124	(Air)	5.90, 7.20	Av.	6.60
$ZrB_2$ 20Ti	HP 141	(Air)	6.05, 5.80, 5.88	Av.	5.92
$ZrB_2$ 20Ti	HP 150 A	(Gas)	6.64, 6.76, 6.55	Av.	6.65
$ZrB_2$ 25Ti	HP 172 A	(Gas)	6.53, 8.77	Av.	7.64
$ZrB_2$ 30Ti	HP 172 B	(Gas)	9.92, 10.5	Av.	10.2
$ZrB_2$ 20Zr	HP 126	(Air)	4.91, 5.57	Av.	5.17
$ZrB_2$ 20Zr	HP 139	(Air)	5.19, 5.35	Av.	5.27
$ZrB_2$ 20Zr	HP 144*	(Gas)	2.37, 2.66, 2.47	Av.	2.45
$ZrB_2$ 20Zr	HP 174 A	(Gas)	4.93, 5.72,	Av.	5.32
$ZrB_2$ 50Zr	HP 152	(Gas)	5.44, 5.55, 5.20	Av.	5.39
$ZrB_2$ 20Ni	HP 153 B	(Gas)	3.12, 3.23, 2.88	Av.	3.07
$ZrB_2$ 20Ni	HP 173 A	(Gas)	2.99, 3.54	Av.	3.22

\* Metallography revealed poor mixing to be consistent with low strength.

TABLE 18

## WORK OF CONTROLLED FRACTURE, W/2A, FOR CERAMIC MATERIALS

<u>Material</u> <u>Investigators</u>	<u>Material Description</u>	<u>Specimen Configuration</u>	<u>Work of Fracture, W/2A</u> (in-lbs/in <sup>2</sup> )	<u>(J/M<sup>2</sup>)</u>
<u>Alumina:</u>				
Tattersall & Tappin (5)	Thermal Syndicate (505 Recrystallized Rod)	Deep Chevron	0.31	55
Simpson (18)	Sintered $\sigma = 1.97 \times 10^6$ N/M <sup>2</sup> $\sigma = 29,000$ psi	Deep Chevron	0.228	40
<u>Silicon Nitride:</u>				
Lange & Terwilliger (19)	Hot pressed $\sigma = 6.45 \times 10^8$ N/M <sup>2</sup> $\sigma = 94,000$ psi	Double Cantilever	0.40	70
<u>ZrB<sub>2</sub>/Metal Composites:</u>				
ZrB <sub>2</sub> 50Zr	$\sigma = 5.39 \times 10^8$ N/M <sup>2</sup> $\sigma = 79,300$ psi	Deep Chevron	2.96	518
ZrB <sub>2</sub> 30Ti	$\sigma = 10.2 \times 10^8$ N/M <sup>2</sup> $\sigma = 150,000$ psi	Deep Chevron	0.79	138
<u>ZrB<sub>2</sub>/SiC/C Composite:</u>				
VIII(14,30)M2	$\sigma = 2.04 \times 10^8$ N/M <sup>2</sup> $\sigma = 30,000$ psi	Deep Chevron	0.50	88

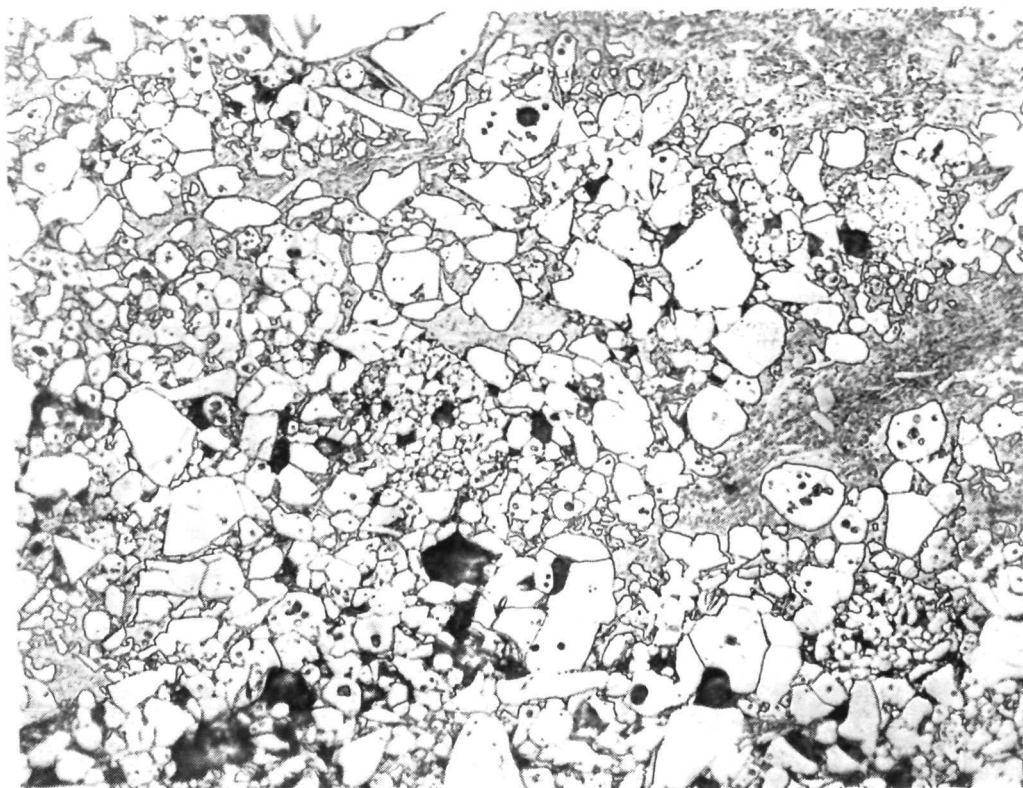


Plate No.

6579 A

Etched

650X

Characterization Data:

Density:	5.6 g/cc
X-Ray Diffraction:	ZrB <sub>2</sub> principal phase
Atom Fraction Ti:	0.10
Atom Fraction Zr:	0.30
Atom Fraction B:	0.60

Figure 1. Microstructural Features and Characterization Data for Hot Pressed Material, ZrB<sub>2</sub>12.5Ti, HP 118.

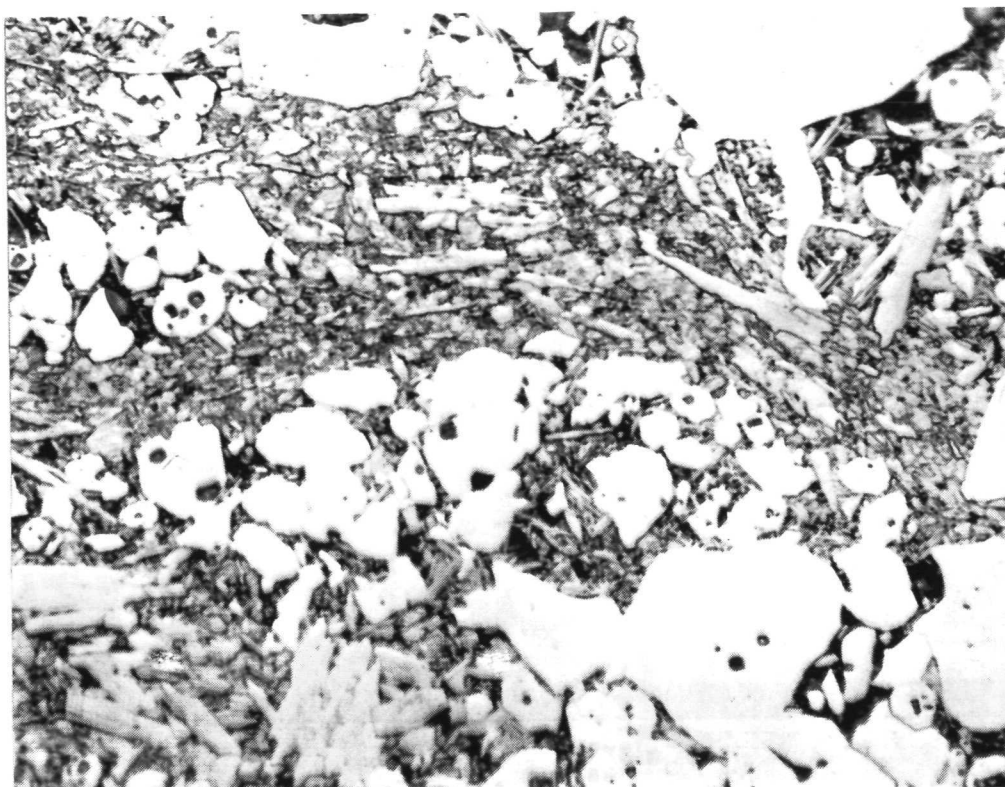


Plate No.  
6419 A

Etched

1500X

Characterization Data:

Density:	5.6 g/cc
X-Ray Diffraction:	ZrB <sub>2</sub> principal phase, TiB identified
Atom Fraction Ti:	0.16
Atom Fraction Zr:	0.28
Atom Fraction B:	0.56

Figure 2. Microstructural Features and Characterization Data for Hot Pressed Material, ZrB<sub>2</sub>20Ti, HP 124.

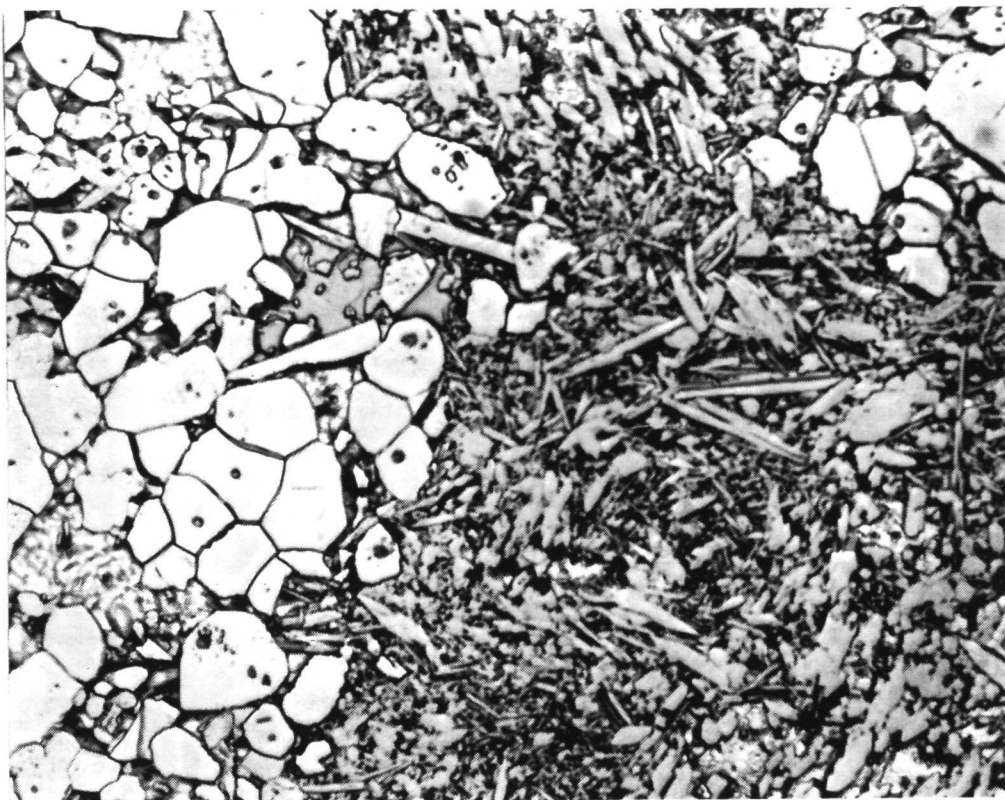


Plate No.  
6497

Etched

1500X

Characterization Data:

Density:	5.6 g/cc
X-Ray Diffraction:	ZrB <sub>2</sub> principal phase, TiB identified
Atom Fraction Ti:	0.16
Atom Fraction Zr:	0.28
Atom Fraction B:	0.56

Figure 3. Microstructural Features and Characterization Data for Hot Pressed Material, ZrB<sub>2</sub>20Ti, HP 141.

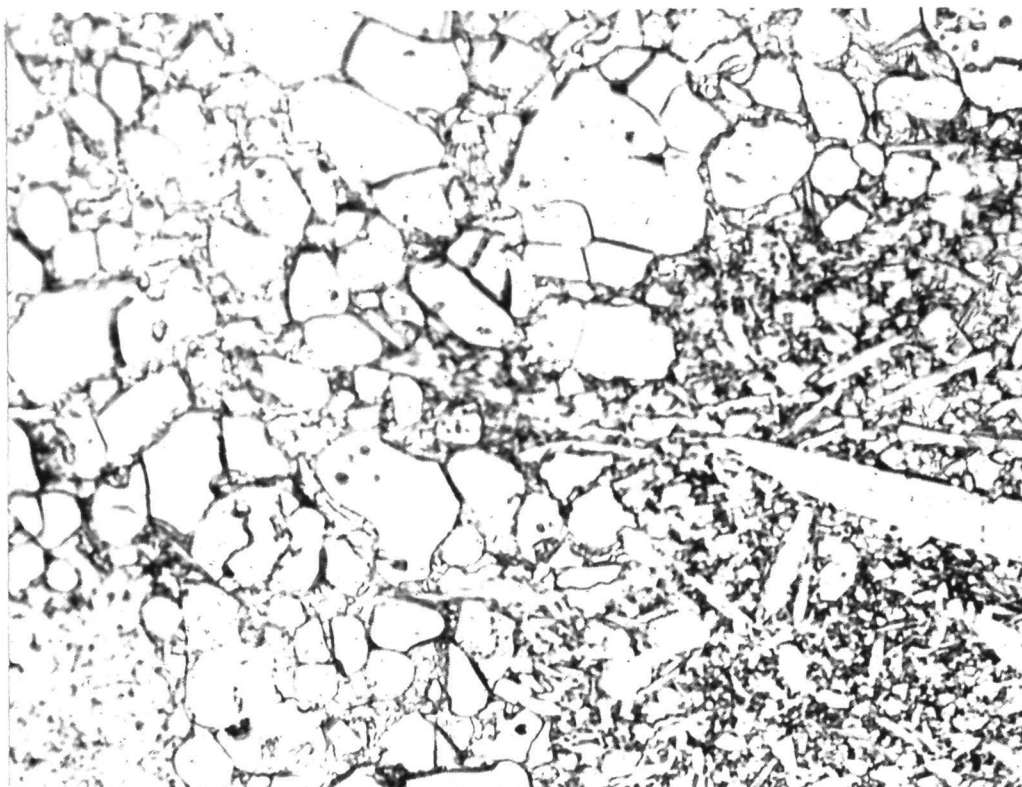


Plate No.  
6581

Etched

1500X

Characterization Data:

Density:	5.57 g/cc
X-Ray Diffraction:	ZrB <sub>2</sub> principal phase, TiB identified
Atom Fraction Ti:	0.21
Atom Fraction Zr:	0.26
Atom Fraction B:	0.53

Figure 4. Microstructural Features and Characterization Data for Hot Pressed Material, ZrB<sub>2</sub>25Ti, HP 172 A.

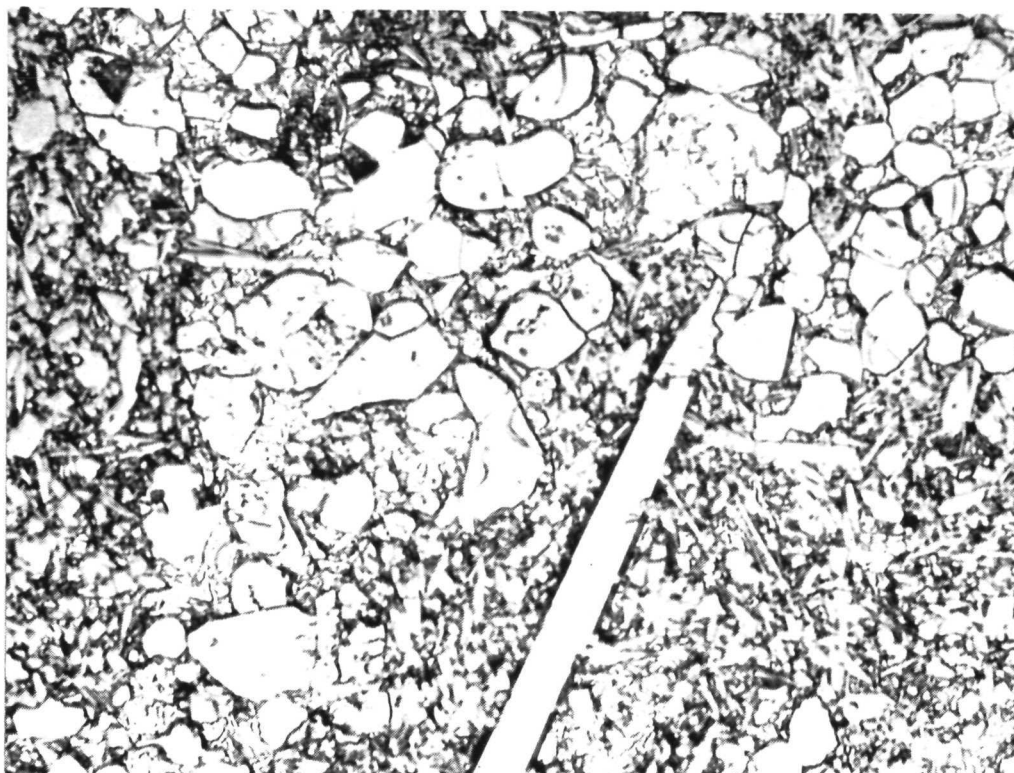


Plate No.

6582

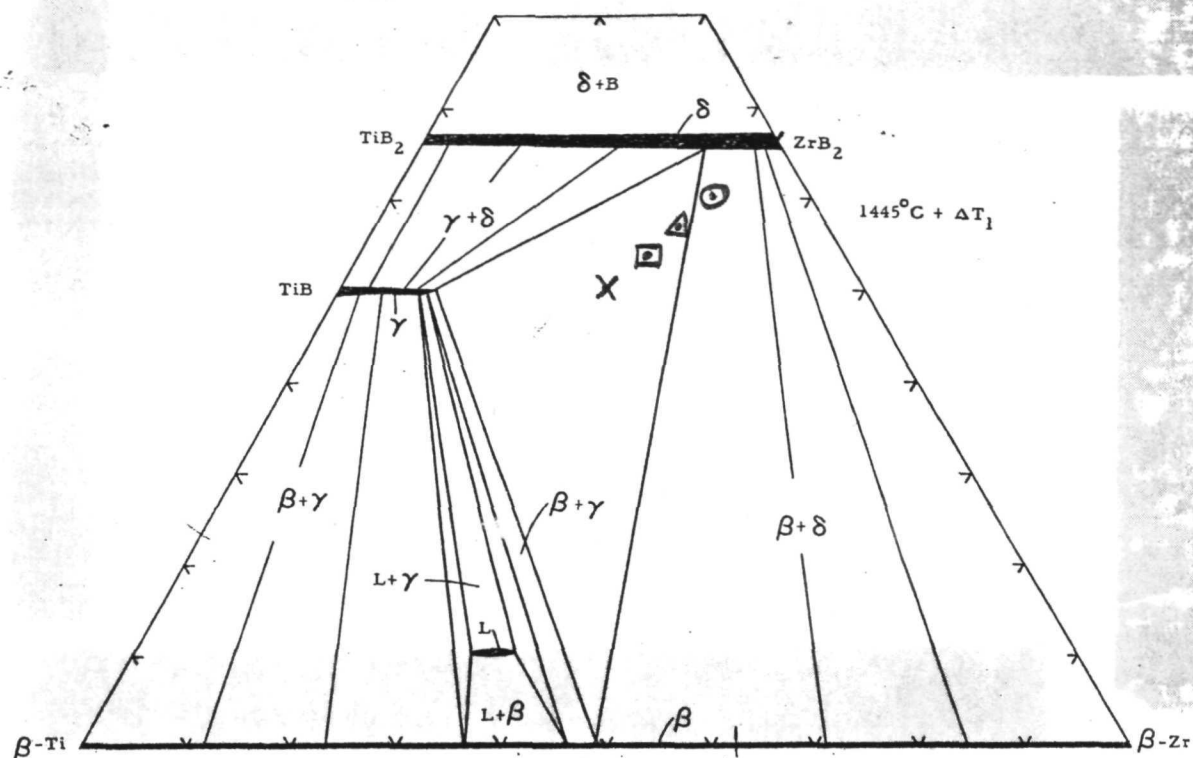
Etched

1500X

Characterization Data:

Density:	5.50 g/cc
X-Ray Diffraction:	ZrB <sub>2</sub> principal phase, TiB identified
Atom Fraction Ti:	0.25
Atom Fraction Zr:	0.25
Atom Fraction B:	0.50

Figure 5. Microstructural Features and Characterization Data for Hot Pressed Material, ZrB<sub>2</sub>30Ti, HP 172 B.

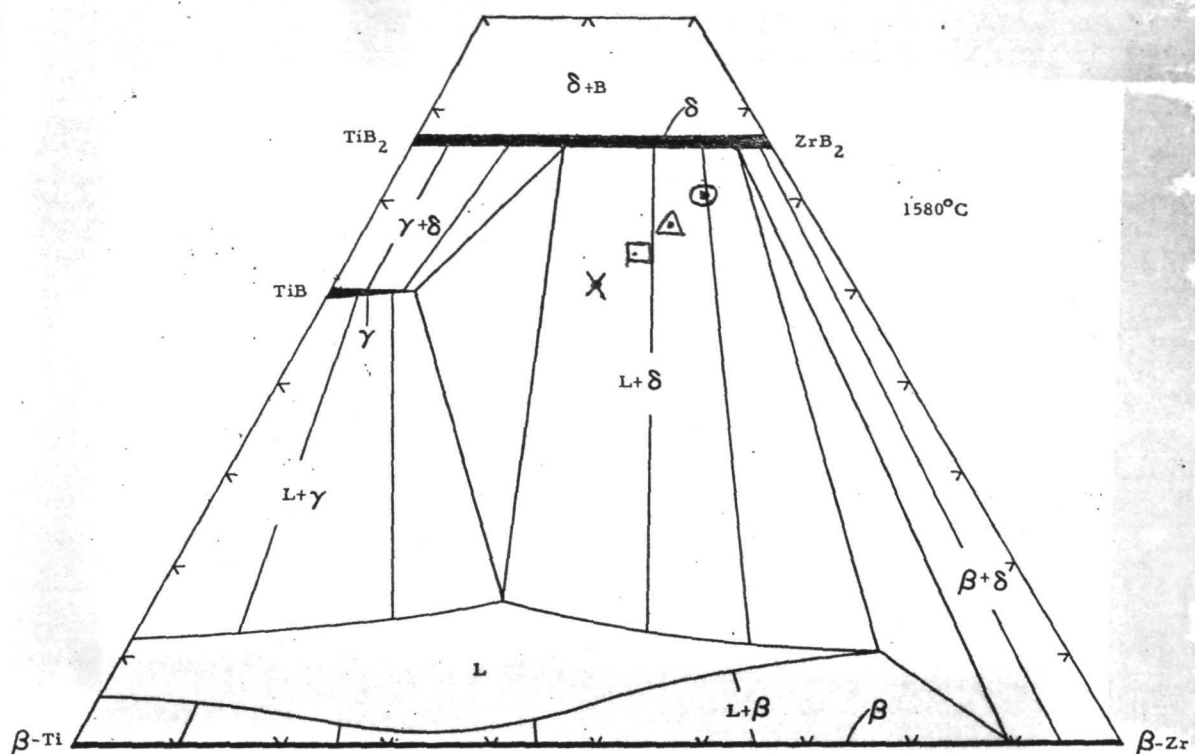


Atomic Fraction

	<u>Ti</u>	<u>Zr</u>	<u>B</u>
⊙	0.10	0.30	0.60
△	0.16	0.28	0.56
□	0.21	0.26	0.53
X	0.25	0.25	0.50

Figure 6. Isothermal Section of the Ti-Zr-B System  
Slightly Above 2640°F.

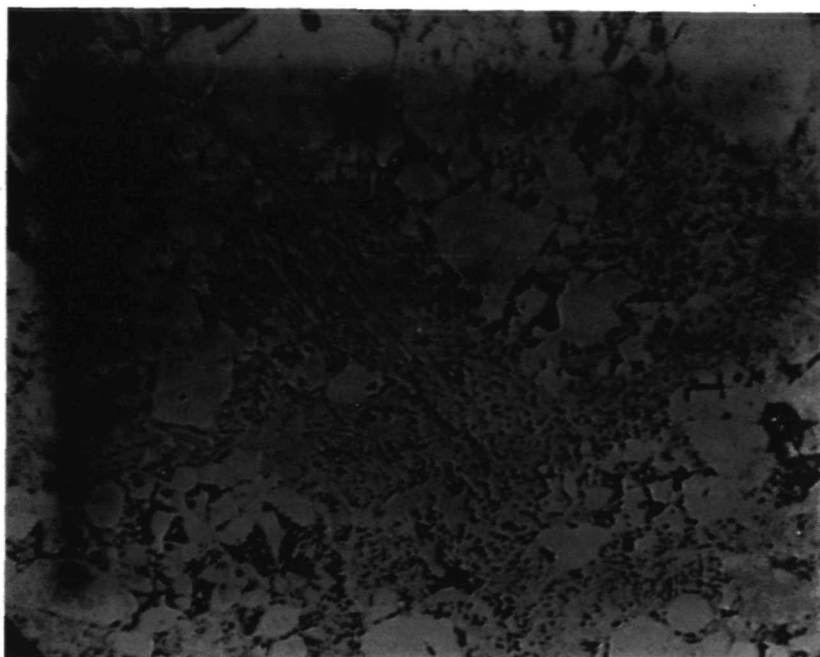




Atomic Fraction

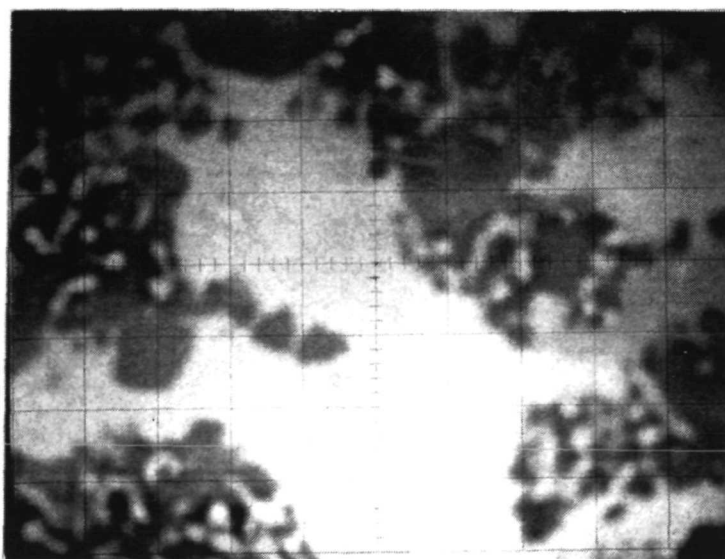
	<u>Ti</u>	<u>Zr</u>	<u>B</u>
⊙	0.10	0.30	0.60
△	0.16	0.28	0.56
□	0.21	0.26	0.53
X	0.25	0.25	0.50

Figure 7. Isothermal Section of the Ti-Zr-B System at 2875°F.



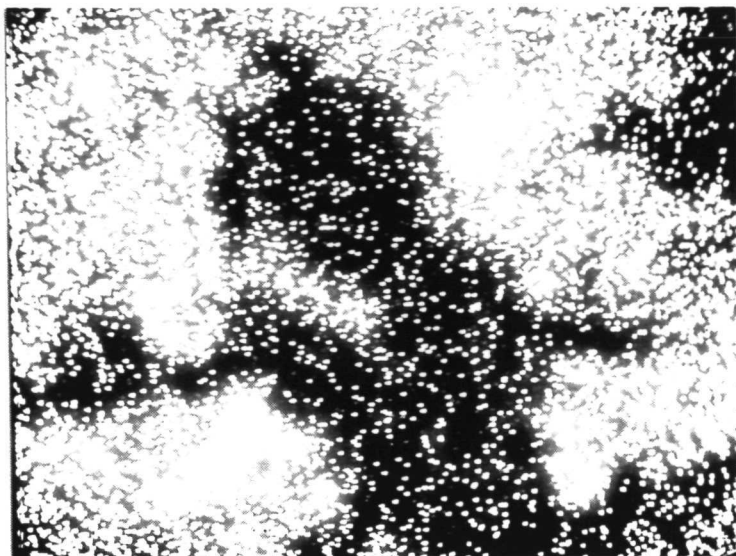
750X

Figure 8. Area of Billet HP 124 Studied by Electron Microprobe Scanning Display



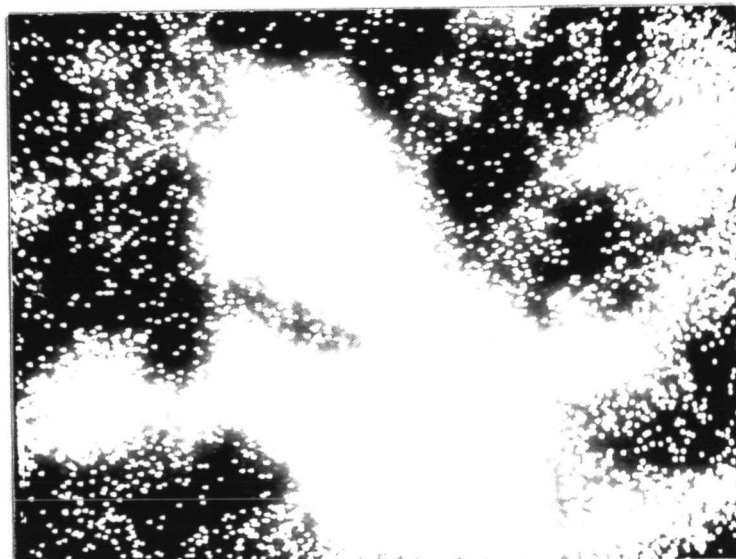
800X

Figure 9. Billet HP 124, Sample Current (-) Display with Titanium-rich Areas Appearing Light



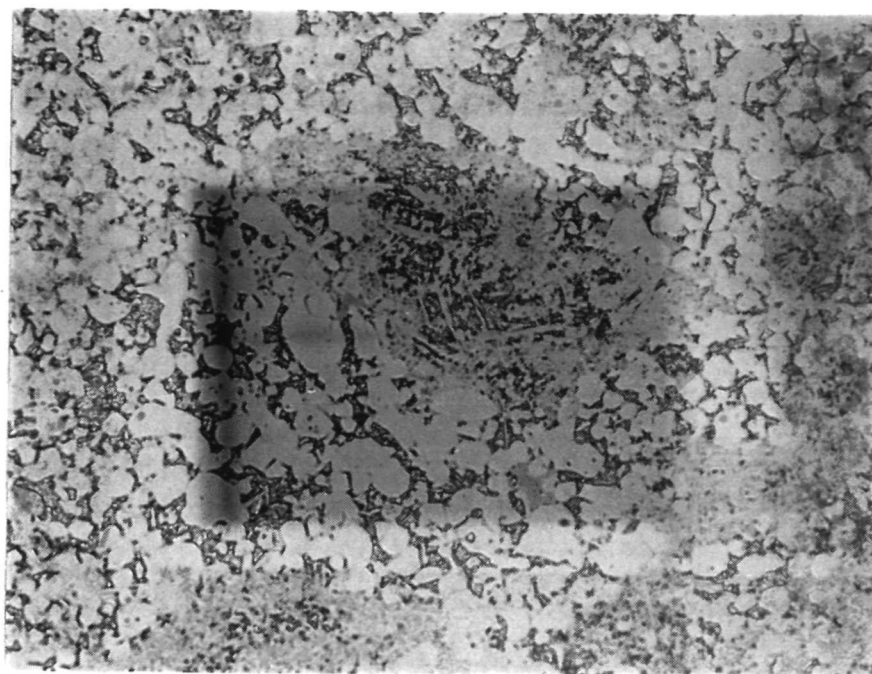
800X

Figure 10. Billet HP 124, Zr-L $\beta$  (1) X-ray Display



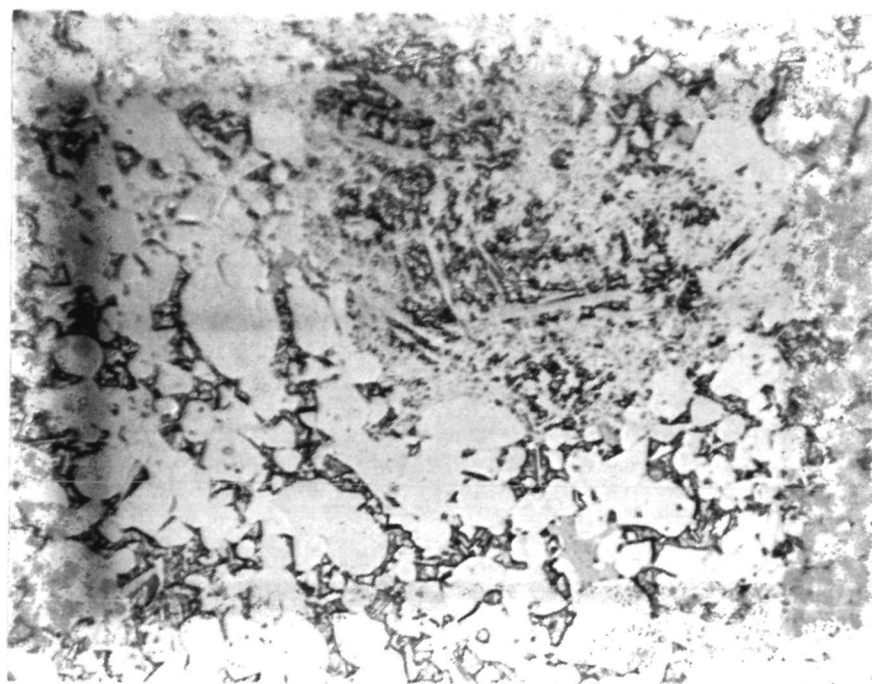
800X

Figure 11. Billet HP 124, Ti-K $\alpha$  (1) X-ray Display



500X

Figure 12. Area of Billet HP 141 Studied by Electron Microprobe Scanning Display



750 X

Figure 13. Magnified Area of Billet HP 141 Studied by Electron Microprobe Scanning Display

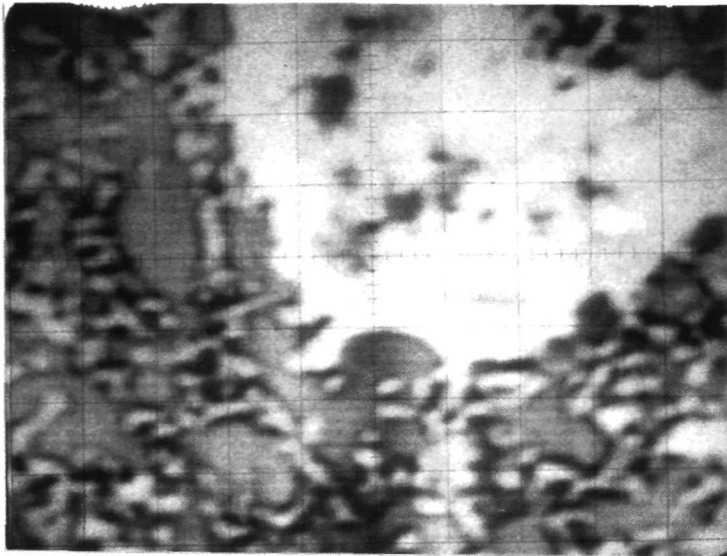


Figure 14. Billet HP 141,  
Sample Current (-) Display,  
Ti-rich Areas Light

800X

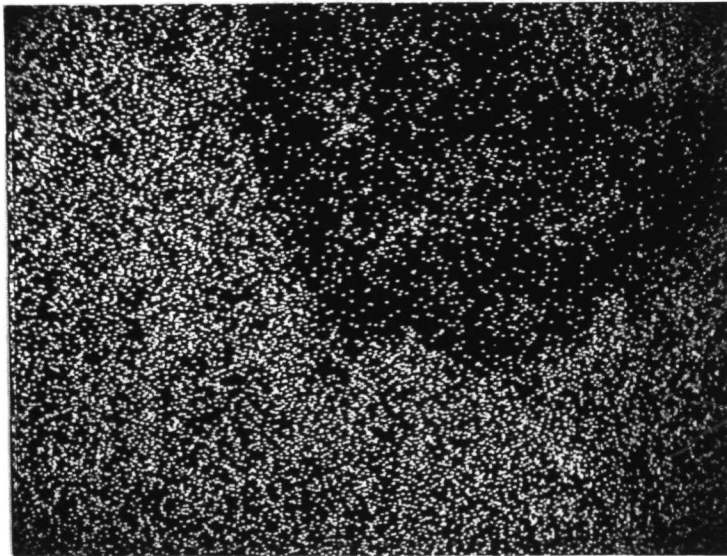


Figure 15. Billet HP 141,  
Zr-L $\beta$  (1) X-ray Display

800X

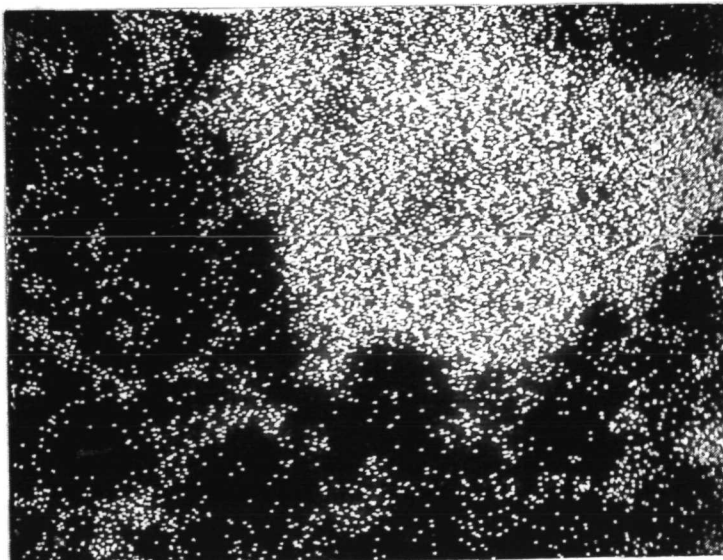
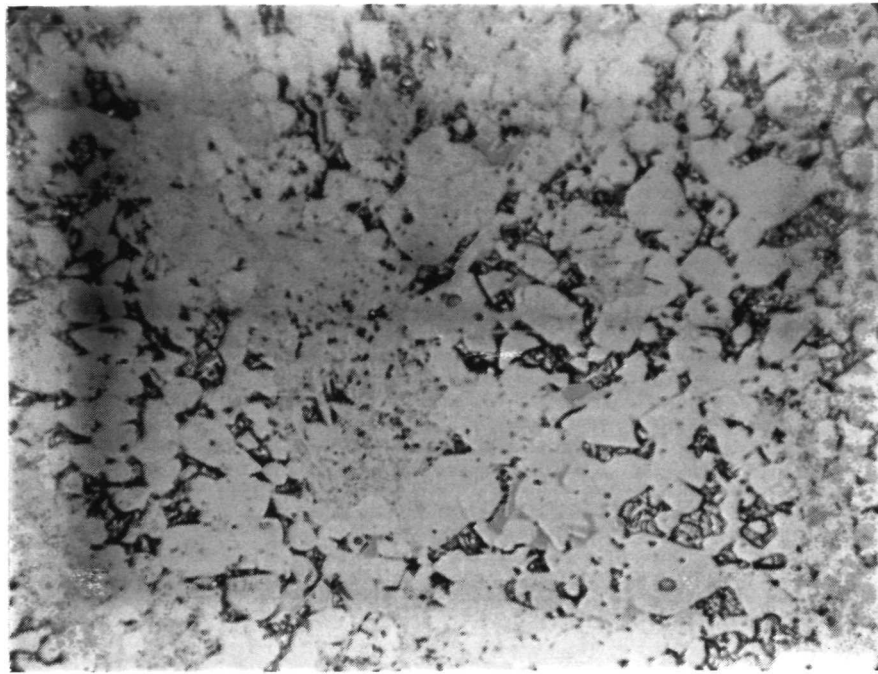


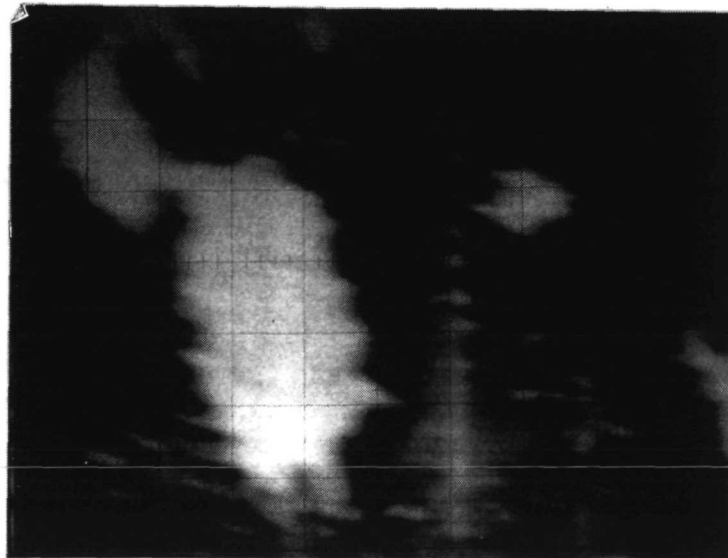
Figure 16. Billet HP 141,  
Ti-K $\alpha$  (1) X-ray Display

800X



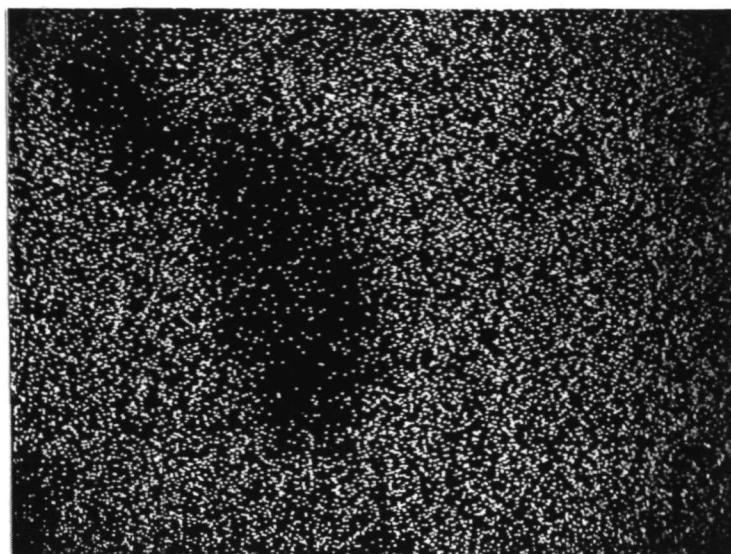
750X

Figure 17. Area of Billet HP 150 B Studied by Electron Microprobe Scanning Display



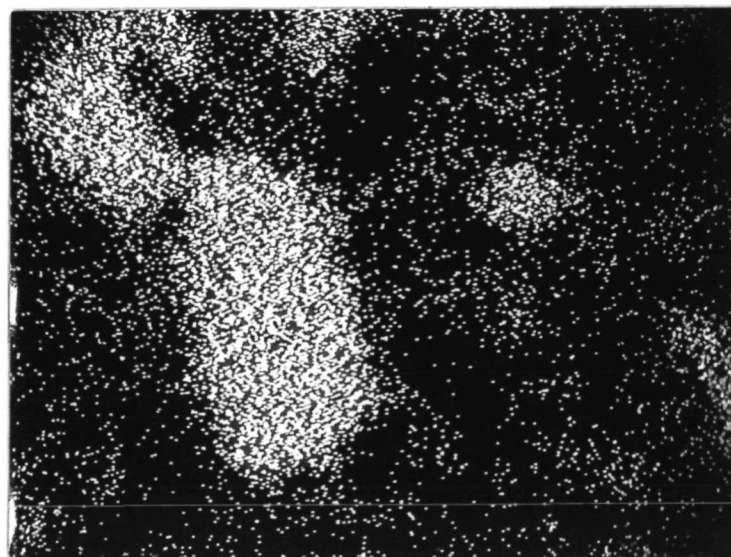
800X

Figure 18. Billet HP 150 B, Sample Current (-) Display with Titanium-rich Areas Appearing Light



800X

Figure 19. Billet HP 150 B, Zr-L $\beta$  (1) X-ray Display



800X

Figure 20. Billet HP 150 B, Ti-K $\alpha$  (1) X-ray Display



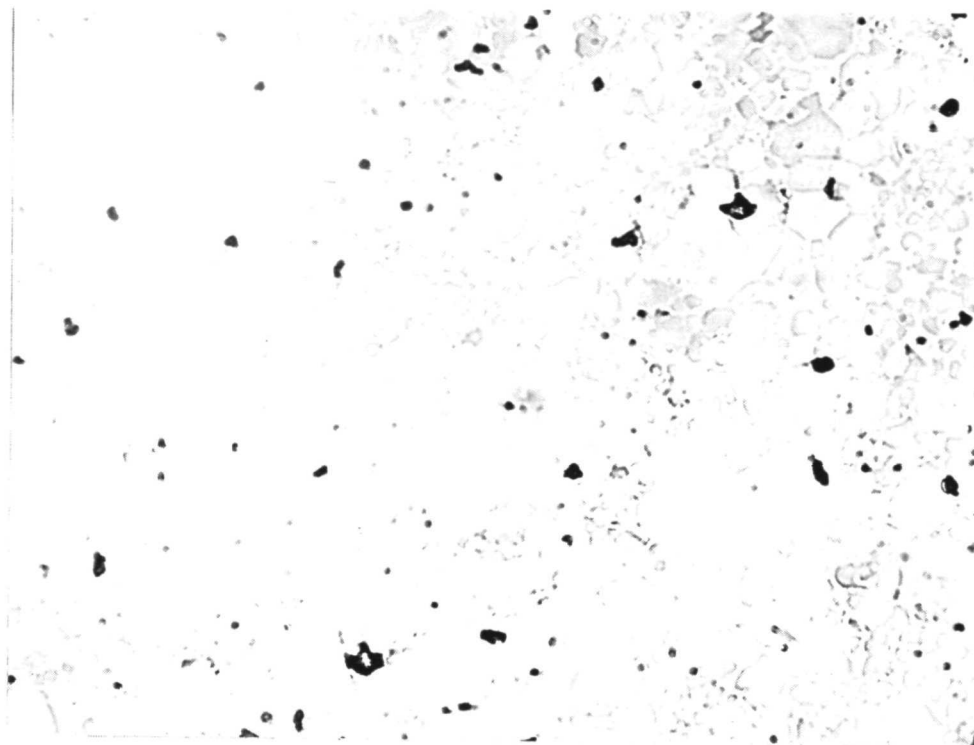


Plate No.  
6414 A

As Polished

500X

Characterization Data:

Density: 6.10 g/cc

X-Ray Diffraction:  $\text{ZrB}_2$  principal phase, Zr secondary phase

Figure 21. Microstructural Features and Characterization Data  
for Hot Pressed Material,  $\text{ZrB}_2\text{-20Zr}$ , HP 126.



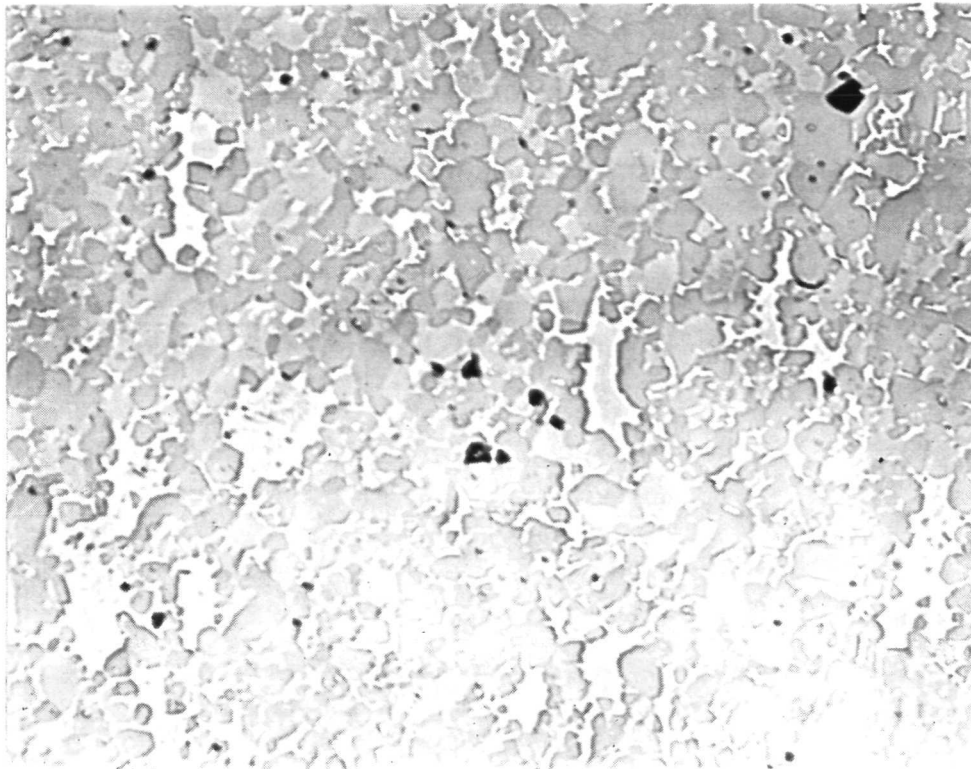


Plate No.  
6587

As Polished

500X

Characterization Data:

Density: 6.19 g/cc

X-Ray Diffraction:  $\text{ZrB}_2$  principal phase, Zr secondary phase

Figure 22. Microstructural Features and Characterization Data for Hot Pressed Material,  $\text{ZrB}_2\text{-20Zr}$ , HP 144.

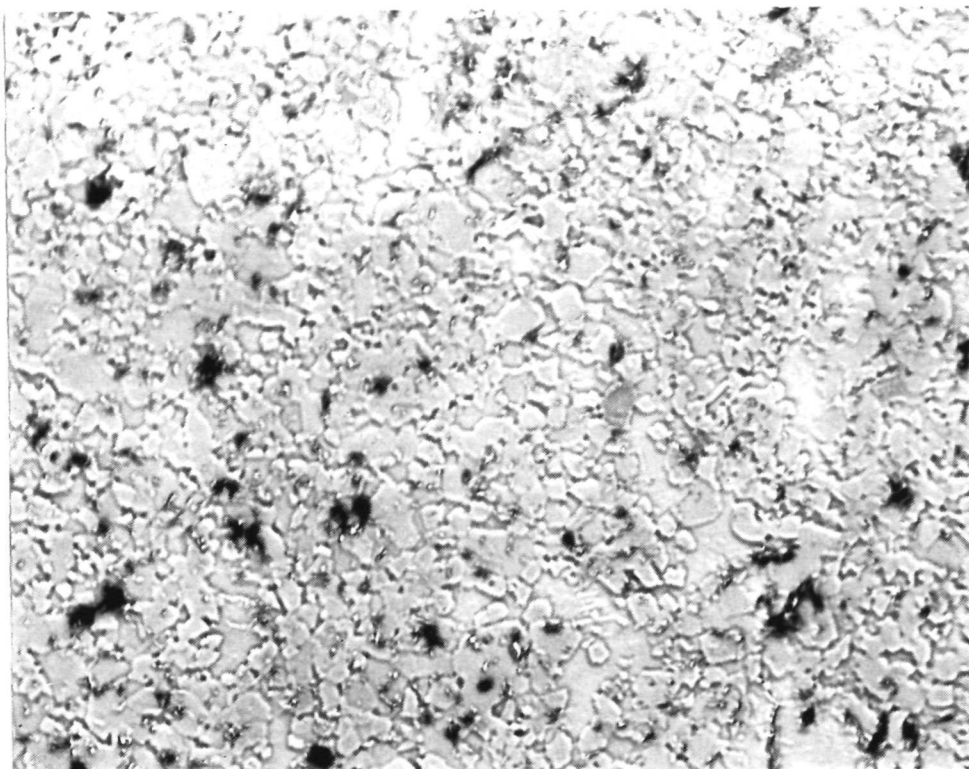


Plate No.  
6591

As Polished

500X

Characterization Data:

Density:

X-Ray Diffraction:  $\text{ZrB}_2$  principal phase, Zr secondary phase

Figure 23. Microstructural Features and Characterization Data for Hot Pressed Material,  $\text{ZrB}_2\text{20Zr}$ , HP 174 A.

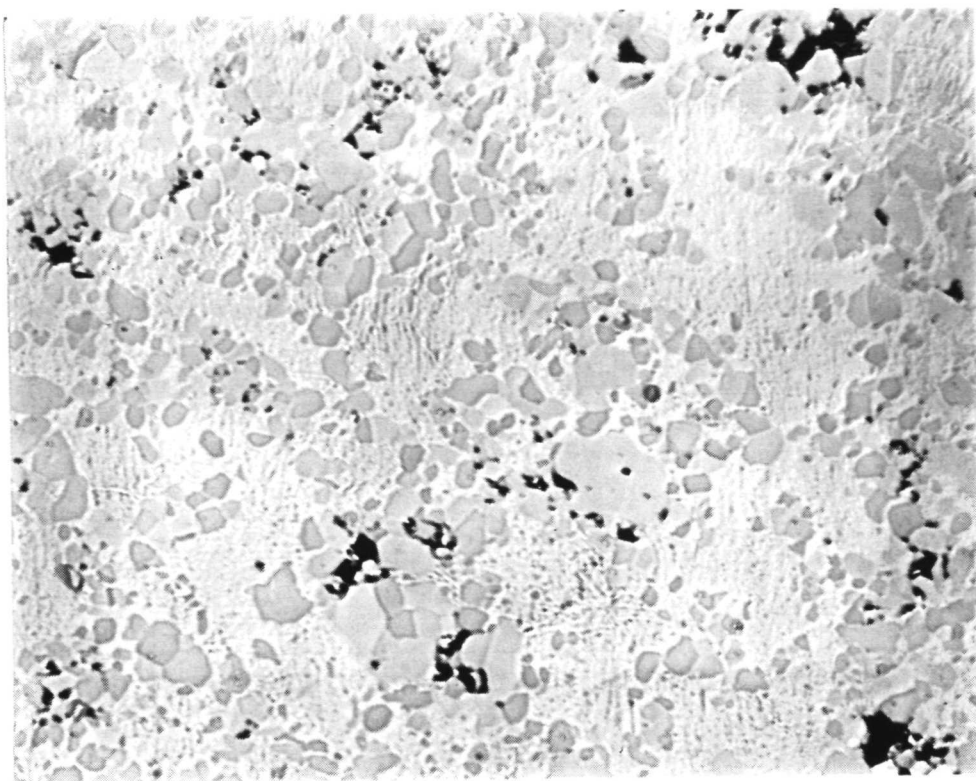


Plate No.  
6593

As Polished

500X

Characterization Data:

Density: 6.24 g/cc

X-Ray Diffraction:  $\text{ZrB}_2$  principal phase, Zr secondary phase

Figure 24. Microstructural Features and Characterization Data for Hot Pressed Material,  $\text{ZrB}_2$ 50Zr, HP 152 A.

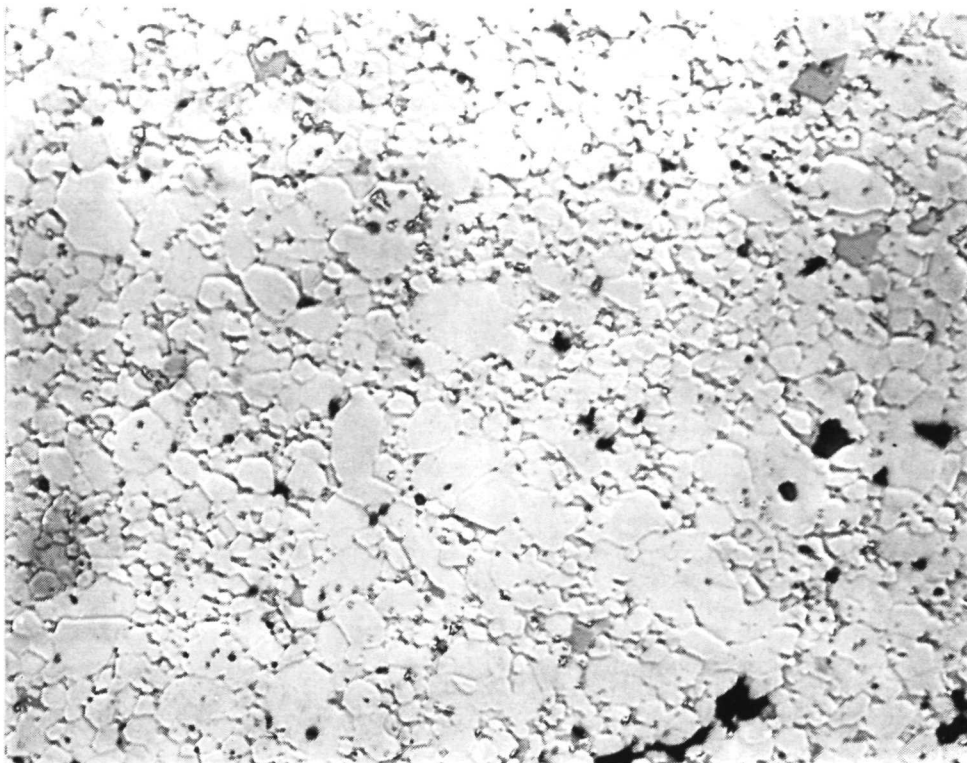


Plate No.

6585

As Polished

500X

Characterization Data:

Density:	6/20 g/cc
X-Ray Diffraction:	ZrB <sub>2</sub> principal phase
Electron Probe Analysis:	Zr and Ni identified

Figure 25. Microstructural Features and Characterization  
Data for Hot Pressed Material, ZrB<sub>2</sub>20Ni, HP 153.

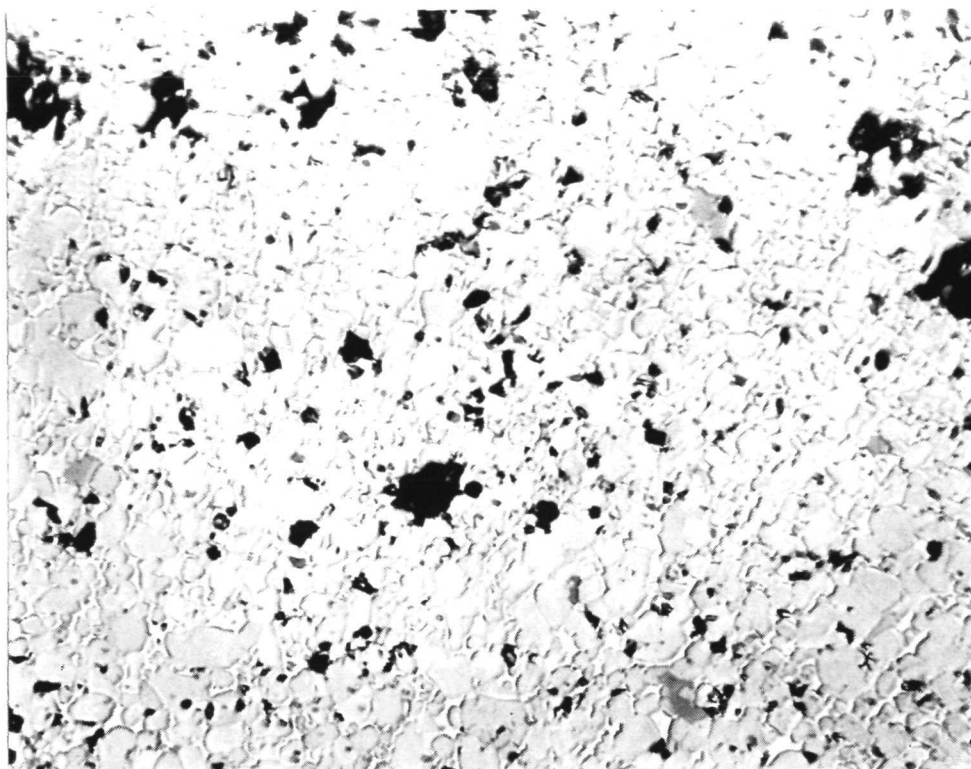


Plate No.

6583

As Polished

500X

Characterization Data:

Density:	6.28 g/cc
X-Ray Diffraction:	ZrB <sub>2</sub> principal phase
Electron Probe Analysis:	Zr and Ni identified

Figure 26. Microstructural Features and Characterization  
Data for Hot Pressed Material, ZrB<sub>2</sub>20Ni, HP 173 A.

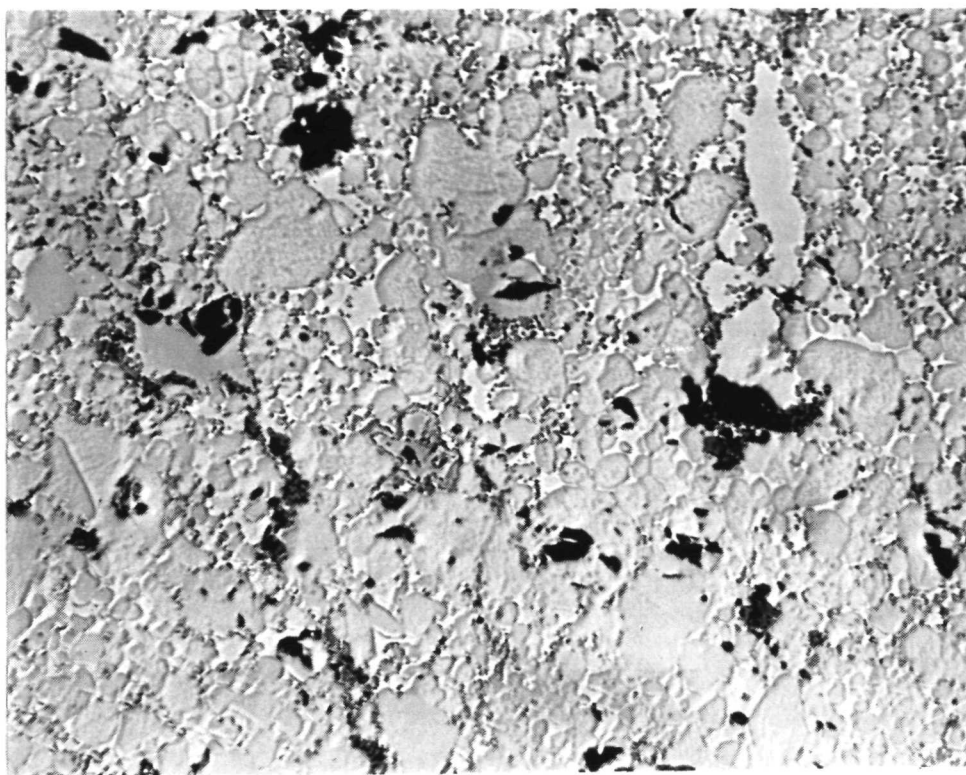


Plate No.  
6416

As Polished

500X

Characterization Data

Density:

X-Ray Diffraction:  $\text{ZrB}_2$  principal phase,  $\text{Ni}_3\text{B}_4$  identified.

Metallography: Nichrome reacted leaving voids in otherwise dense microstructure with grain boundary phase observed.

Figure 27. Microstructural Features and Characterization Data for Hot Pressed Material,  $\text{ZrB}_2\text{-20Ni}$ ; Nichrome Wire, HP 127.

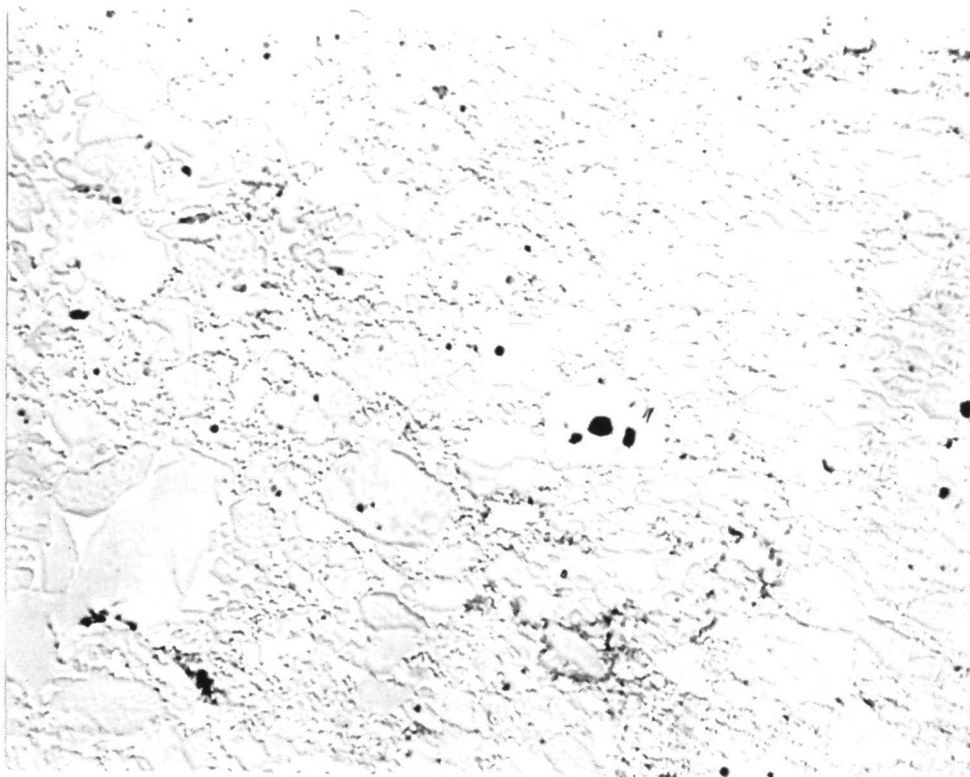


Plate No.  
6435

As Polished

500X

#### Characterization Data

Density:

X-Ray Diffraction:  $\text{ZrB}_2$  principal phase,  $\text{Ni}_3\text{B}_4$  identified.

Metallography: Nichrome reacted leaving voids in otherwise dense microstructure with grain boundary phase observed.

Figure 28. Microstructural Features and Characterization Data for Hot Pressed Material,  $\text{ZrB}_2\text{20Ni}$ : Nichrome Wire, HP 131.



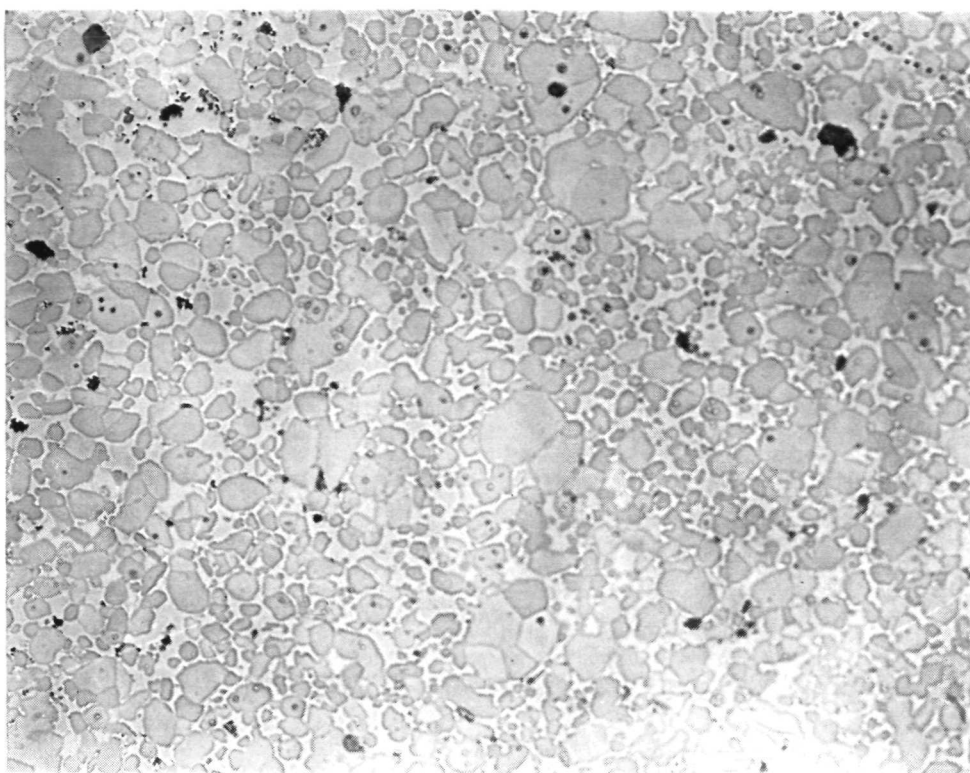


Plate No.  
6468

As Polished

500X

Characterization Data

Density:

X-Ray Diffraction:  $\text{ZrB}_2$  principal phase,  $\text{Ni}_3\text{B}_4$  identified.

Metallography: Nichrome reacted leaving voids in otherwise dense microstructure with grain boundary phase observed.

Figure 29. Microstructural Features and Characterization Data for Hot Pressed Material,  $\text{ZrB}_2\text{-20Ni}$ : Nichrome Wire, HP 134.



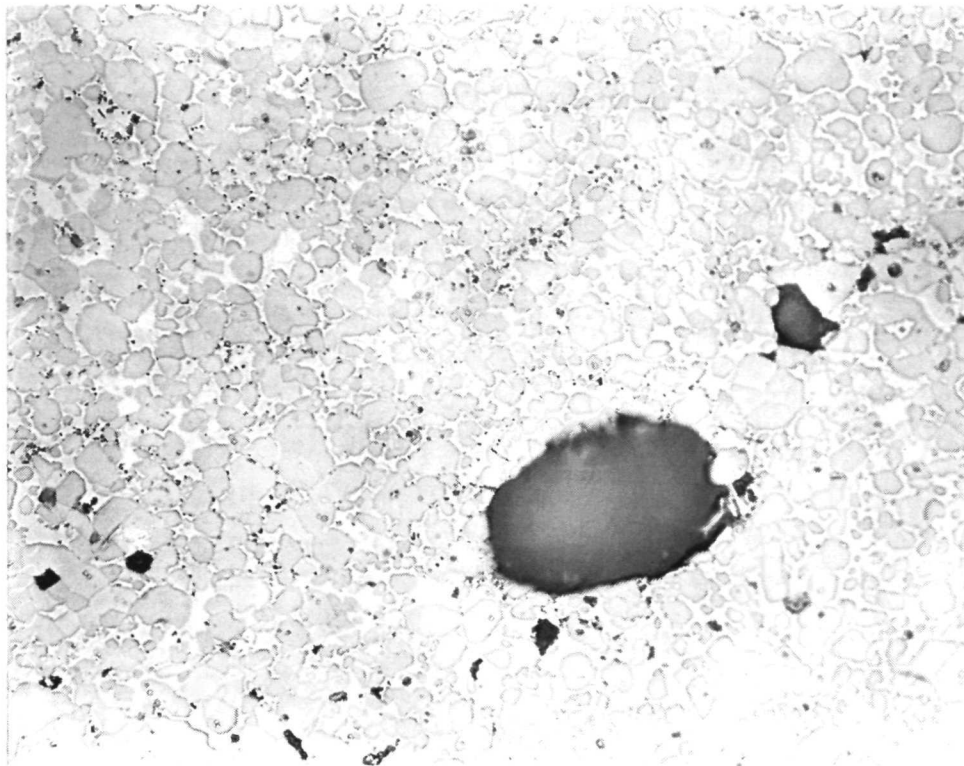


Plate No.  
6467

As Polished

500X

Characterization Data

Density:

X-Ray Diffraction:  $\text{ZrB}_2$  principal phase.

Metallography: Stainless steel reacted leaving voids in otherwise dense microstructure with grain boundary phase observed.

Figure 30. Microstructural Features and Characterization Data for Hot Pressed Material,  $\text{ZrB}_2\text{20Ni}$ : stainless steel wire, HP 138.

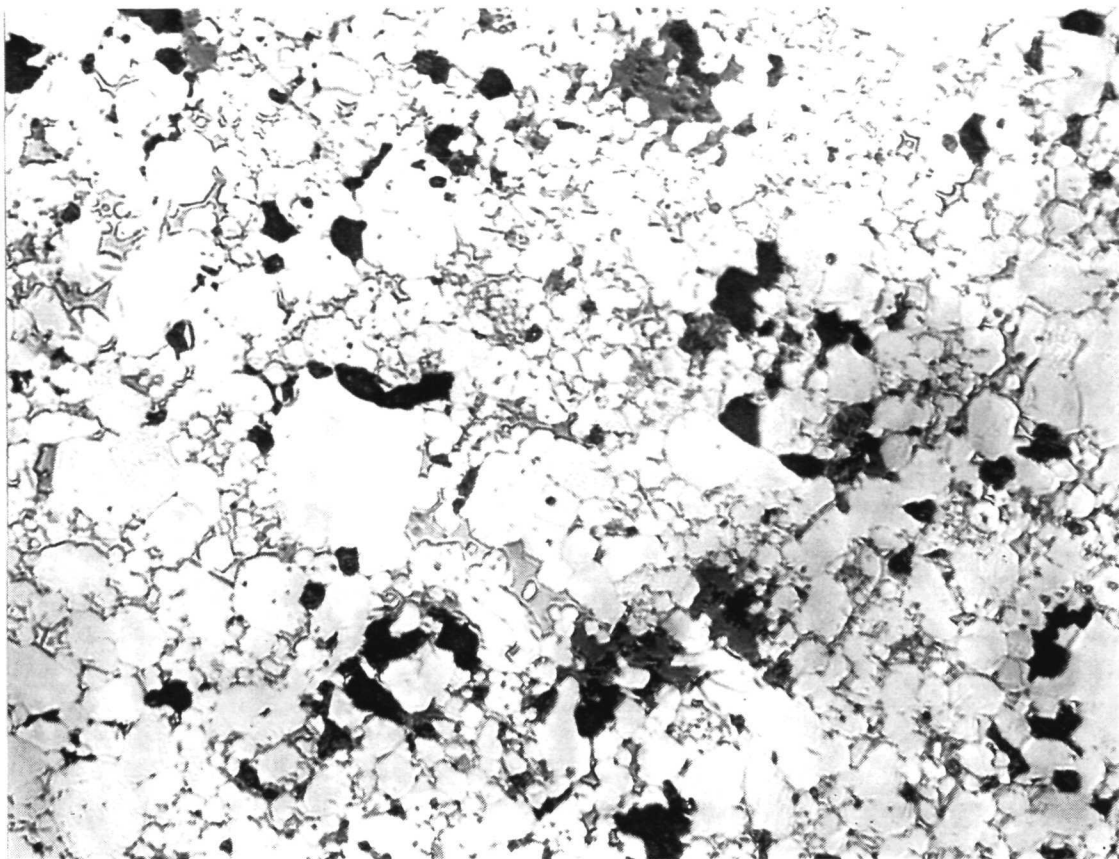


Plate No.  
6352

Etched

500X

Characterization Data:

Density: 5.84 g/cc (97% powder density)  
 X-Ray Diffraction:  $\text{ZrB}_2$  principal phase,  $\alpha$  Fe and possible Zr C indicated  
 Electron Microprobe Analysis: Fe distribution at grain boundaries

Figure 31. Microstructural Features and Characterization Data for Hot Pressed Material,  $\text{ZrB}_2$  10 Fe, HP 98

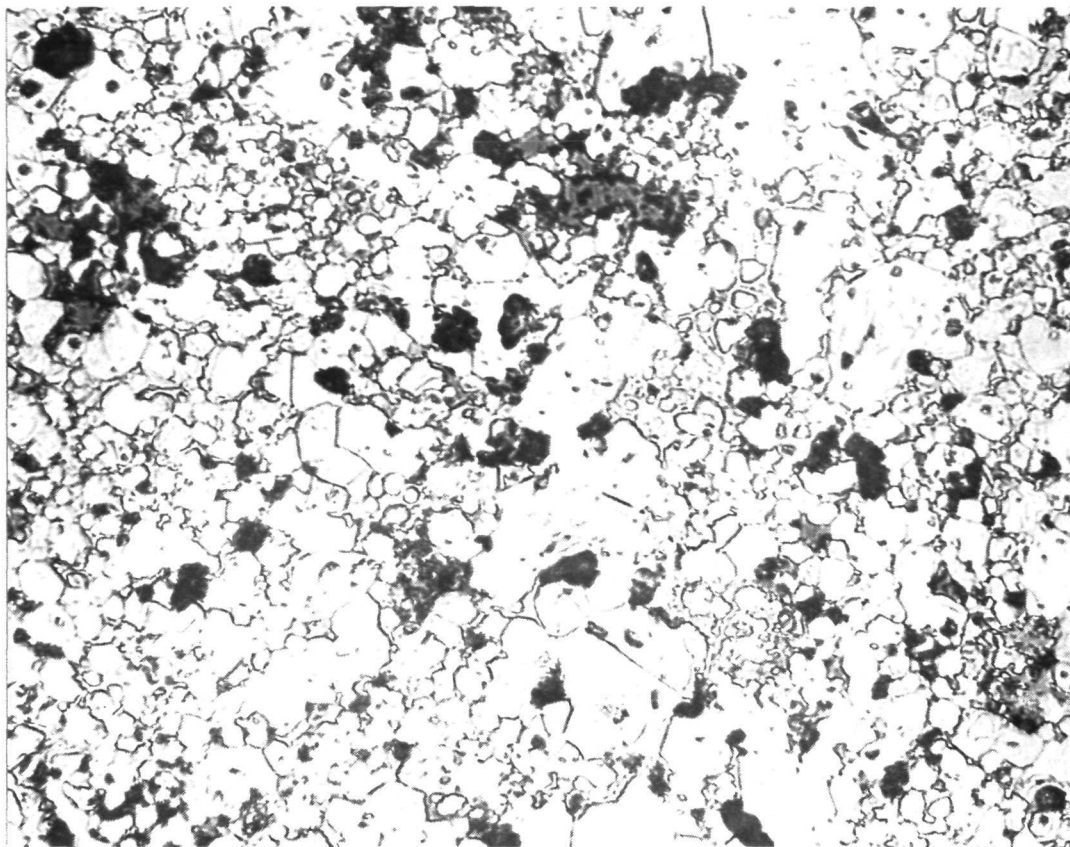


Plate No.  
6278

Etched

500X

Characterization Data:

Density: 6.03 g/cc (100 + % powder density)

X-Ray Diffraction:  $\text{ZrB}_2$  principal phase,  $\alpha$  Fe not identified

Figure 32. Microstructural Features and Characterization Data for Hot Pressed Material,  $\text{ZrB}_2$  10Fe, HP101

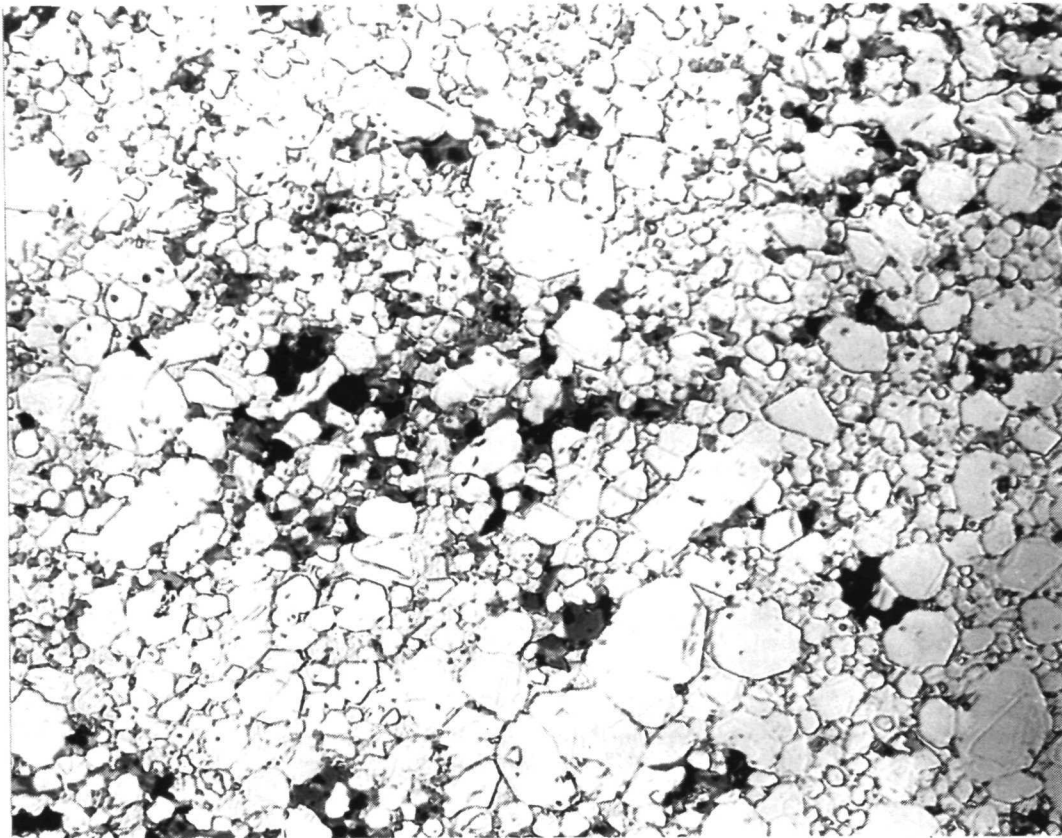


Plate No.  
6333

Etched

500X

Characterization Data:

Density:

6.31 g/cc (99<sup>+</sup> % powder density)

X-Ray Diffraction:

ZrB<sub>2</sub> principal phase,  $\alpha$  Fe not identified

Figure 33. Microstructural Features and Characterization Data for Hot Pressed Material, ZrB<sub>2</sub> 20 Fe, HP 106

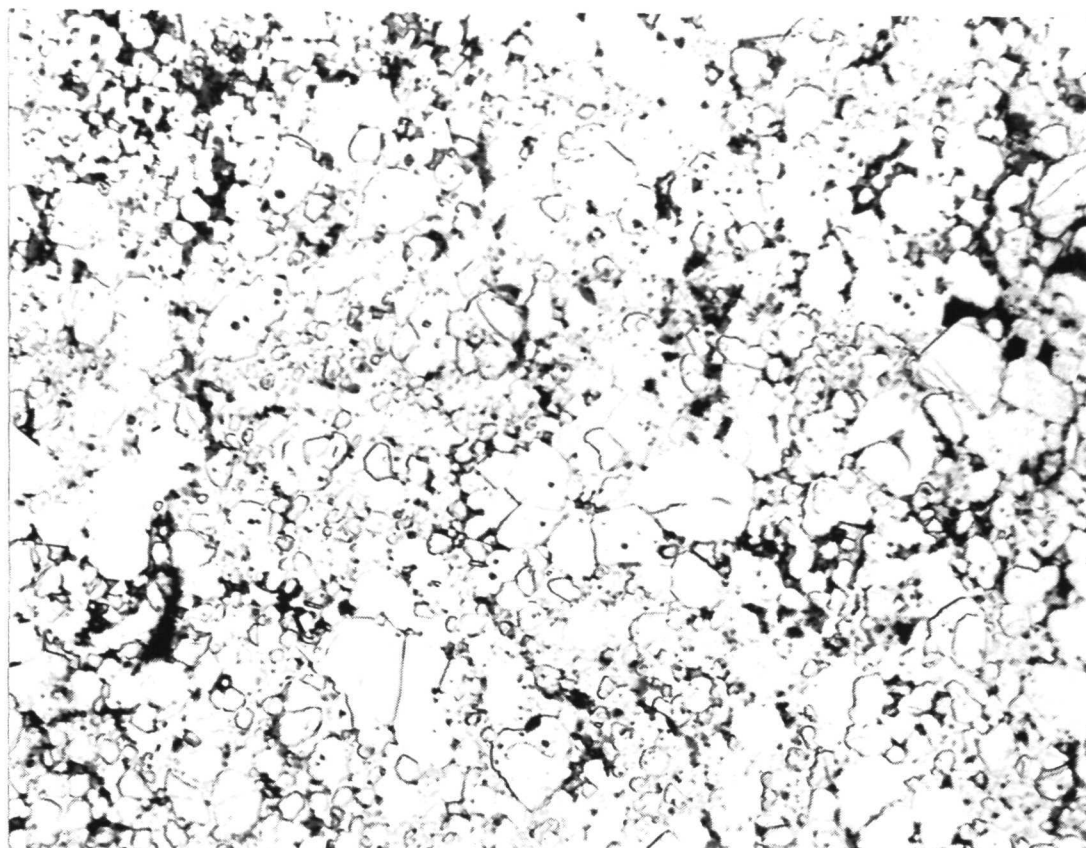


Plate No.  
6304

Etched

500X

Characterization Data:

Density:

6.34 g/cc (98 % powder density)

X-Ray Diffraction

ZrB<sub>2</sub> principal phase,  $\alpha$  Fe indentified, ZrC indicated

Figure 34. Microstructural Features and Characterization Data for  
Hot Pressed Material, ZrB<sub>2</sub> 30 Fe, HP 107

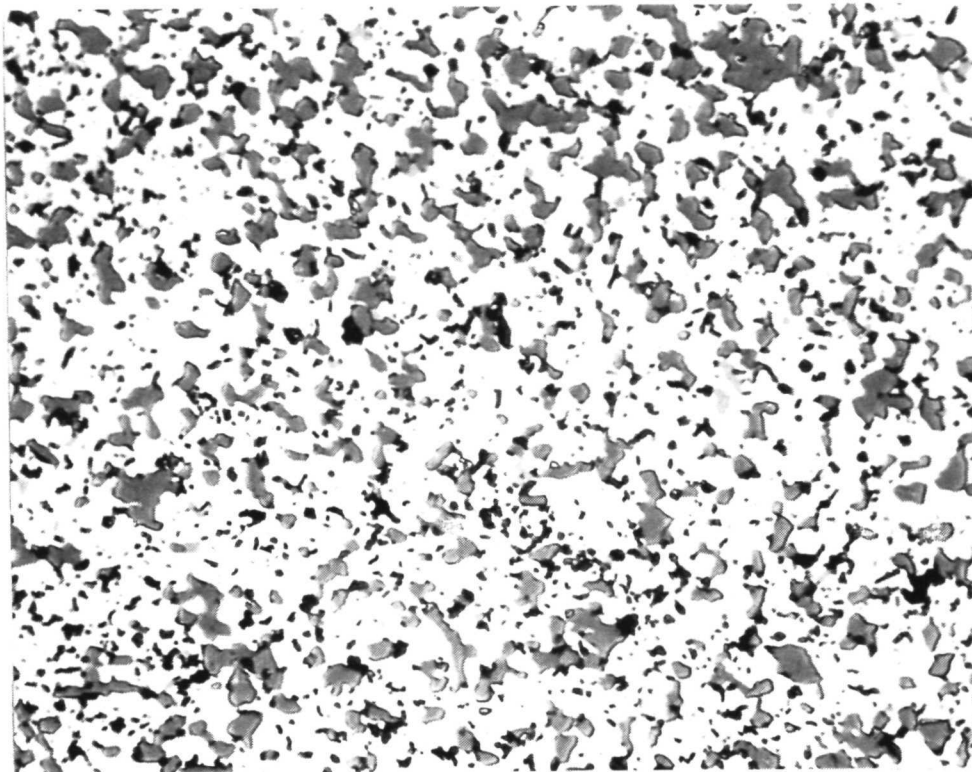


Plate No.  
5466

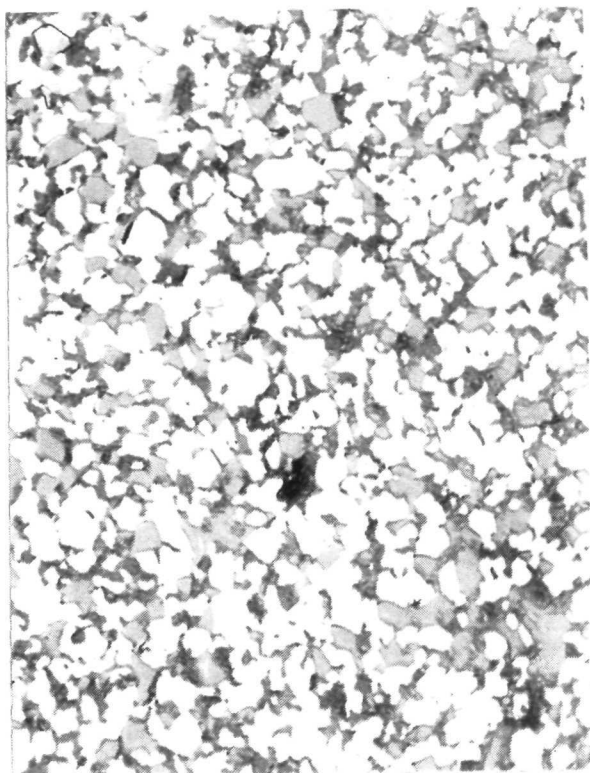
As Polished

500X

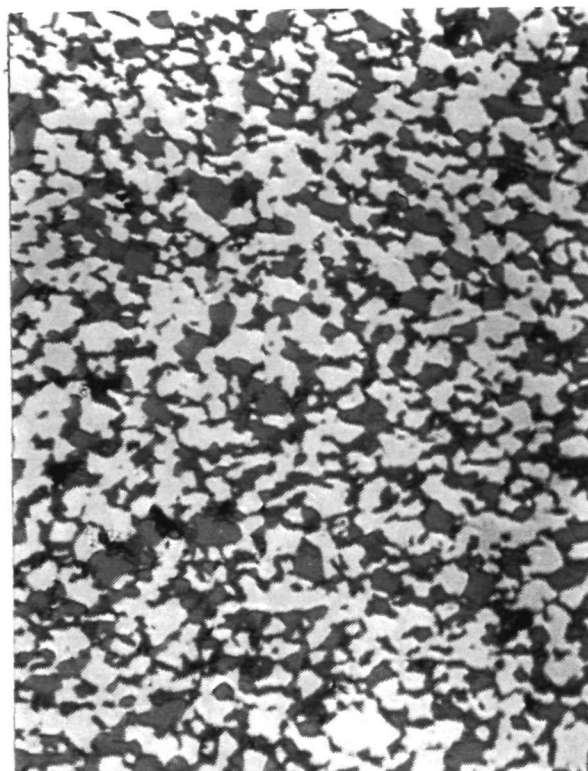
Composition:	72ZrB <sub>2</sub> :18SiC:10C (volume proportions)
Billet Identification:	VIII(18,10) 07F R40L, 5.21 g/cc
Billet Size:	6 inches square x 1.5 inches high
Fabrication Conditions:	3710°F, 3000 psi, 145 minutes (at 3710°F)
Billet Density:	330 lbs/ft <sup>3</sup>

Figure 35. Composition, Fabrication Conditions and Microstructural Features of Diboride Material VIII(18,10).





As Polished 500X  
Parallel\* Orientation  
Plate No. 6211



As Polished 500X  
Perpendicular\* Orientation  
Plate No. 6210

Composition:  $56\text{ZrB}_2:14\text{SiC}:30\text{C}$  (volume proportions)

Billet Identification: NP6M2

Billet Size: 9 inches x 7 inches x 3 1/2 inches (Norton Company)

Density: 4.46 g/cc

Sonic Modulus: Parallel  $43.4 \times 10^6$  psi

Perpendicular  $29.4 \times 10^6$  psi

\*Orientations are relative to the plane of the hot pressed billet which is perpendicular to the direction of the applied processing pressure.

Figure 36. Composition, Modulus Data, and Microstructural Features of VIII(14,30)M2, NP6M2.

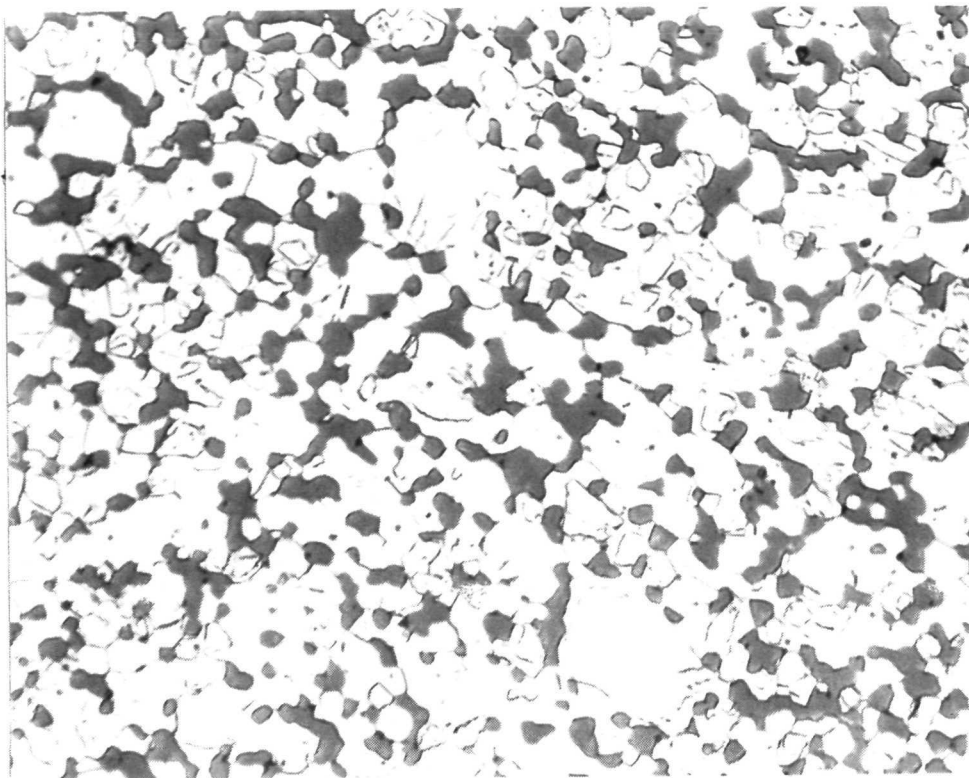


Plate No.  
5775

Etched with 10 Glycerine 5HNO<sub>3</sub>:HF

500X

Figure 37. Microstructural Characteristics of Boride  
V (80<sup>V</sup>/oZrB<sub>2</sub>-20<sup>V</sup>/oSiC).



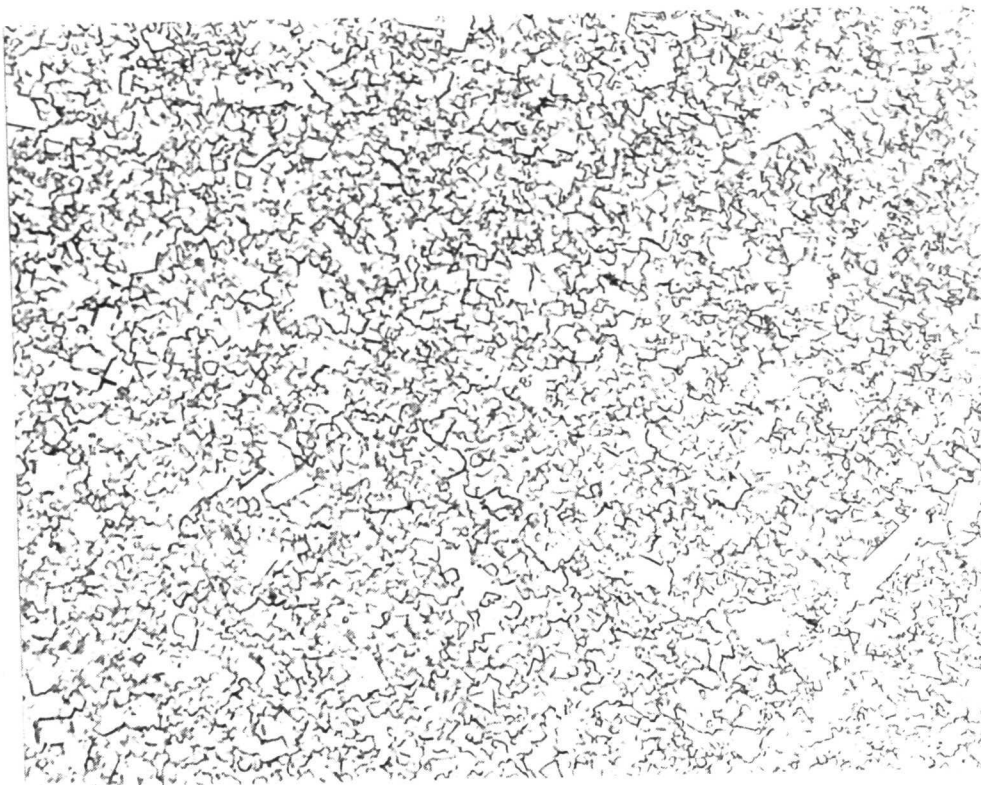
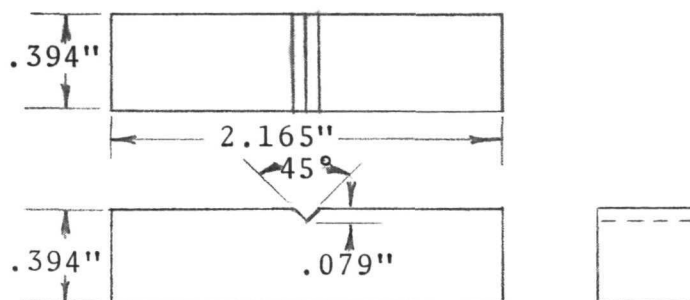


Plate No.  
6176

Etched.

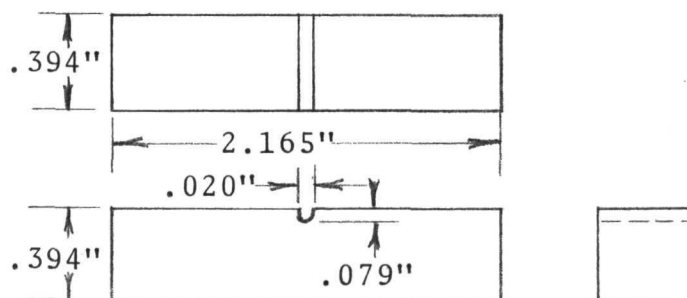
1500X

Figure 38. Microstructural Features of Tungsten Carbide Cermet,  
WC6Co.



"V" Notch Specimen

Root Radius =  $2.54 \times 10^{-4}$  M (0.010 inch)



Saw Kerf Specimen

Root Radius =  $2.54 \times 10^{-4}$  M (0.010 inch)

Figure 39. Notch and Kerf Configurations for Impact and Slow Bend Test Specimens.

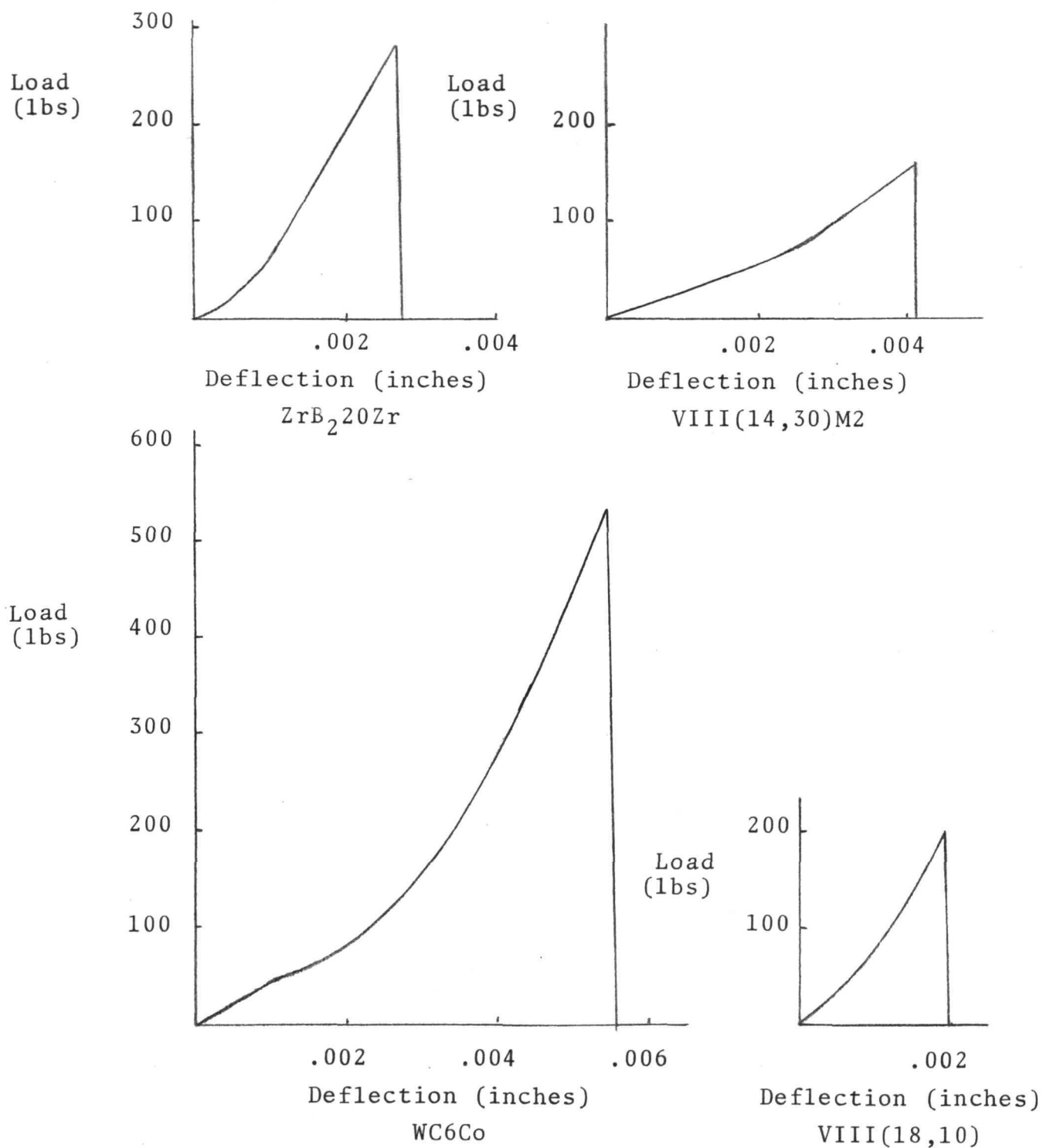
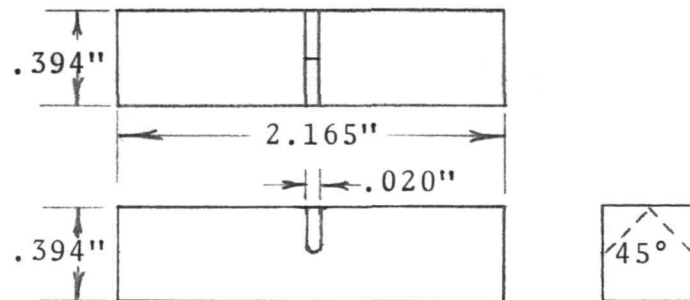
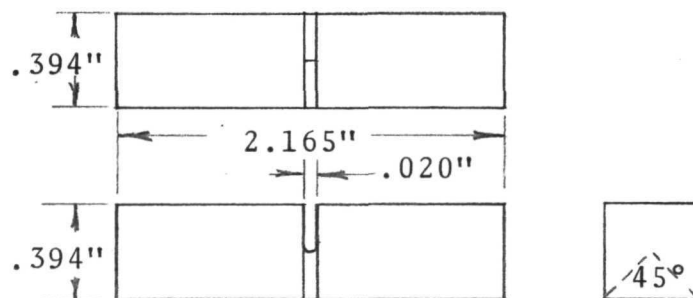


Figure 40. Typical Slow Bend Load vs. Deflection Data for Catastrophic Failure of V-Notch Specimens on Hard Test Machine.



Shallow Chevron Notch  
Configuration A



Deep Chevron Notch  
Configuration B

Figure 41. Chevron Configurations for Slow Bend Test Specimens.

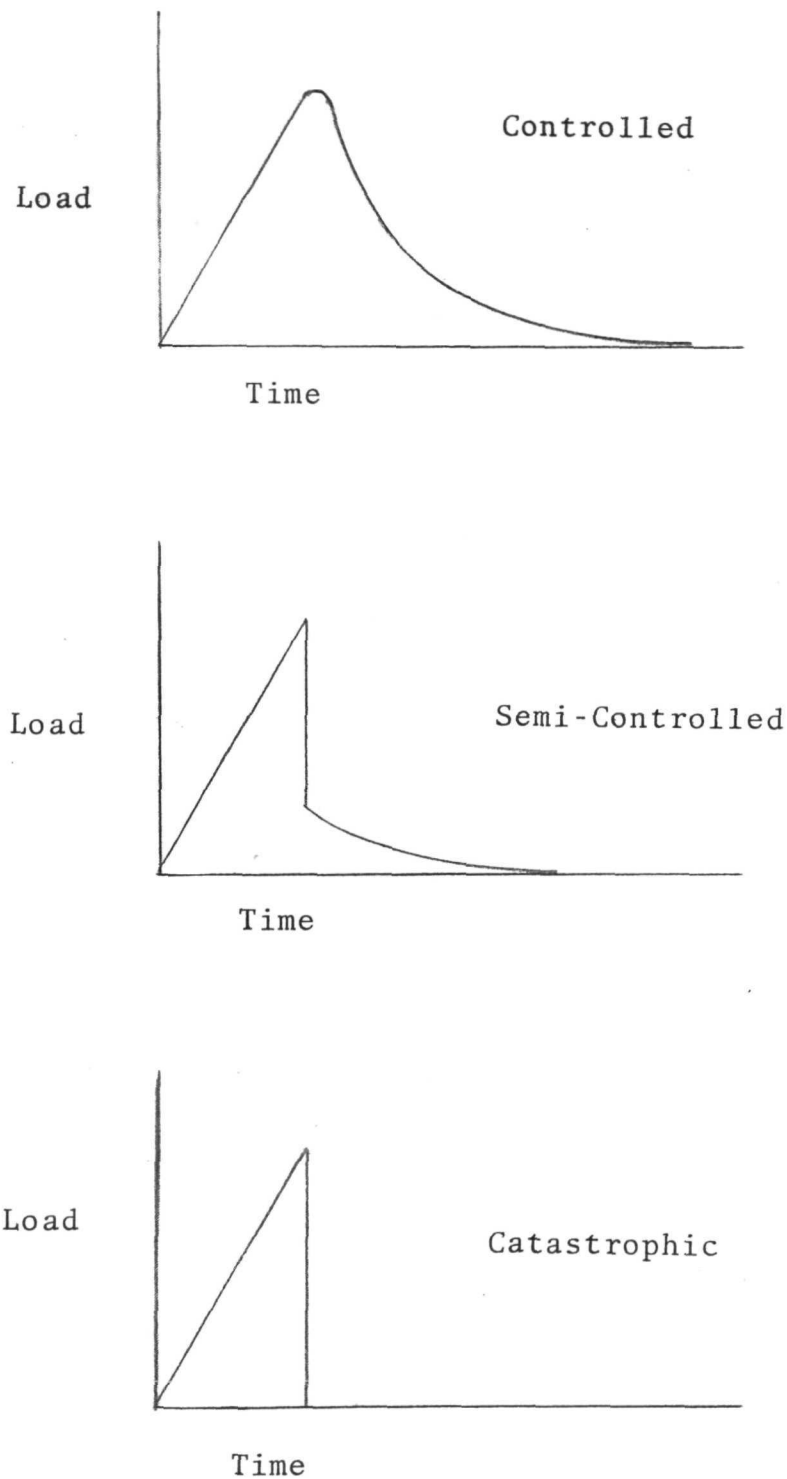


Figure 42. Typical Slow Bend Load vs. Deflection Data for Controlled, Semi-Controlled and Catastrophic Failure of Deep Chevron Specimens.